Branching Fractions in B0 Meson Decays to A1+-(1260) Pi-+ and A1+-(1260)K-+ with the BaBar Experiment at SLAC

By: Vincenzo Lombardo (Milan U.)

Ph.D. Thesis (Advisors: Fernando F. Palombo and James G. Smith).

Università degli Studi di Milano

Facoltà di Scienze Matematiche, Fisiche e Naturali

Dipartimento di Fisica

Corso di Dottorato di Ricerca in Fisica, Astrofisica e Fisica Applicata

Fisica del Nucleo e delle Particelle

CICLO XIX

TIME DEPENDENT CP VIOLATING ASYMMETRIES AND BRANCHING FRACTIONS IN B^0 MESON DECAYS TO $a_1^\pm(1260)\pi^\mp$ AND $a_1^\pm(1260)K^\mp$ WITH THE *BABAR* EXPERIMENT AT SLAC

TESI PRESENTATA DAL

DOTT. VINCENZO LOMBARDO

PER IL CONSEGUIMENTO DEL TITOLO DI

DOTTORE DI RICERCA

Tutor: Chiar.mo Prof. F. Palombo
           Università degli Studi di Milano
Co-Tutor: Chiar.mo Prof. J. G. Smith
           University of Colorado, Boulder

Coordinatore del Dottorato di Ricerca: Chiar.mo Prof. G. Bellini

Anno Accademico 2005–2006

Alla mia famiglia

To my family

Contents

Introduction

The goal of this thesis is realized at *BABAR* experiment in the asymmetric b-factory PEP-II at SLAC (Stanford Linear Accelerator Center, Stanford, USA). The history of CP violation is one of experimental discovery overturning untested assumptions. Observation of the $\theta - \tau$ puzzle in the early 1950s marks the inception of the discovery of the symmetry-violating properties of the weak interaction. Two spin-zero particles of the same mass and lifetime (now known to be charged kaons) were found to decay into different final states of opposite parity, one to two pions and the other to three, seemingly violating parity conservation. In 1956, Lee and Yang showed that parity conservation, while well-tested in strong and electromagnetic interactions, was not experimentally constrained for weak interactions, and proposed a list of experimental tests [1]. Shortly thereafter, C.S. Wu and collaborators performed one of these experiments, and showed that parity was not conserved in nuclear β decay, conclusively demonstrating the uniqueness of the weak interaction among the forces [2].[1] However, the combined CP transformation was still widely assumed to be a symmetry of nature due to the difficulty of explaining the weak interaction without it. The discovery eight years later of CP violation in neutral K mesons by Christenson, Cronin, Fitch and Turlay provided the basis for both far-reaching insight (the Kobayashi-Maskawa prediction of a third family of quarks and leptons, a year before even the charm quark was discovered, and 4 years before the b) [3, 4].

Before 1964, no one realistically expected CP symmetry to be violated. Accomodating CP violating involves a significant increase in the complexity of weak interaction theory that was just not motivated at the time, as only the first 3 quarks had been discovered at that moment. Fitch later remarked that "not many of our colleagues would have given credit for studying CP violation, but we did so anyway" [5]. The beam that was used contained pure K_2^0 ($= K_L^0$) mesons. A two-arm spectrometer was

---

[1]Note however that parity conservation is still poorly experimentally constrained in gravity.

used in order to detect the decay products. After two months of data taking, a significant peak was indeed observed for a $\pi^+\pi^-$ decay of the K_2^0. If mass eigenstates and CP eigenstates were equivalent, K_2^0 would be the purely CP-odd (and slightly heavier) counterpart to the CP-even K_1^0 ($= K_s^0$). But the $\pi^+\pi^-$ final state is CP-even, thus the (presumably) CP-odd K_2^0 should not be able to decay into it *unless CP were violated*. Fitch and Cronin observed a significant peak for a $\pi^+\pi^-$-hypothesis decay at the K_2^0 mass, consisting of 45 ± 9 two-pion events out of a total of 22,700 K_2^0 decays. Although the experiment did result in a slowly increasing acceptance in the physics community that CP was violated, immediately following the measurement strong disbelief did exist. Alternative explanations were proposed, including regeneration of K_1^0, a non-bosonic version of the pion as the actual decay product, and violation of exponential decay laws. These alternatives were at least as unpleasant for theory as the violation of CP itself, and successive experiments refuted their possibility, eventually eliminating all but the Kobayashi-Maskawa quark mixing picture as the description of Cronin and Fitch's results. Thirty-seven years of experimental study of the kaon sector after CP violation was discovered has yielded only recently the observation of direct CP violation, and has merely helped to confirm the counterintuitive picture of a small complex coefficient in a 3 x 3 unitary matrix as the source of the CP asymmetry. The smallness of CP violating effects in the kaon system is an impediment to progress in that sector, although the potential remains for measurements of the decays $K^+ \to \pi^+\nu\overline{\nu}$ and $K_L^0 \to \pi^0\nu\overline{\nu}$, which directly probe the imaginary part of the coefficient. The present and near future lie in B decays, which, as shown by *BABAR* and Belle[2], exhibit significant CP asymmetries, as is predicted by the Standard Model. However, the predictions of the Standard Model regarding CP have yet to be fully examined experimentally, and, as seen above, one cannot take untested ideas for granted. Many well-motivated theoretical extensions of the Standard Model produce strikingly different predictions for CP violation; and the manifest baryon asymmetry of the universe poses great difficulty for reconciliation with the small amount of CP violation predicted by the Standard Model. Such tests are the primary purpose of the *BABAR* experiment — the goal was to either confirm or refute the Standard Model picture of CP violation.

B meson decay channels useful for CP violation studies have a very little branching fractions, in the order of 10^{-4} or less, with a $\Upsilon(4S)$[3] cross section of 1.2 nb. To

---

[2]similar experiment to *BABAR* in the KEK-B accelerator (Tsukuba, Japan).

[3]$\Upsilon(4S)$ is a resonance composed by a quark couple $b\overline{b}$ with mass 10.58 GeV and decades in a couple

observe CP violation a high luminosity collider is necessary (a so called b-factory[4]). Time dependent measurements of asymmetries depend on the ability of evaluating decay vertices of the two B mesons coming from $\Upsilon(4S)$ meson decay. In *BABAR* experiment the measurement of this vertices is due to asymmetric collider (e^- with 9 GeV and e^+ with 3.1 GeV) where Υ mesons are produced with impulse in the laboratory frame. The B mesons boosts make distances run by particles measurable. In this thesis it is presented a measurement of the branching fraction of the decay $B^0 \to a_1^\pm(1260)\,\pi^\mp$ with $a_1^\pm(1260) \to \pi^\mp\pi^\pm\pi^\pm$. The data sample corresponds to 218×10^6 $B\overline{B}$ pairs produced in e^+e^- annihilation through the $\Upsilon(4S)$ resonance. The rare decay $B^0 \to a_1^\pm(1260)\,\pi^\mp$ is expected to be dominated by $b \to u\overline{u}d$ contributions. For the branching fraction of this decay mode an upper limit of 49×10^{-5} at the 90% C.L. has been set by CLEO [6]. Bauer *et al.* have predicted a branching fraction 38×10^{-6} for the decay $\overline{B}^0$ to $a_1^-(1260)\,\pi^+$ within the framework of the factorization model and assuming $|V_{ub}/V_{cb}| = 0.08$ [7]. The study of this decay mode is complicated by the large discrepancies between the parameters of the $a_1(1260)$ meson obtained from analyzes involving hadronic interactions [8] and τ decays [9]. This analysis has been published in *Phys. Rev. Lett.* **97**, 051802 (2006). A time-dependent analysis of the the decay $B^0 \to a_1^\pm(1260)\,\pi^\mp$, in addition to the decays $B^0 \to \pi^+\pi^-$, $B^0 \to \rho^\pm\pi^\mp$, and $B^0 \to \rho^+\rho^-$, can be used to give a new measurement of the Cabibbo-Kobayashi-Maskawa angle α of the Unitarity Triangle [10]. I have performed a quasi two-body time-dependent analysis in decays $B^0 \to a_1^\pm(1260)\,\pi^\mp$ identified by four charged pions in order to determine a phase α_{eff} which is equal to the weak phase α in the limit of vanishing penguin amplitudes. Applying flavour SU(3) to these decays and to $B^0 \to a_1^\pm(1260)\,K^\mp$ and $B^0 \to K_A^\pm\pi^\mp$ with K_{1A} an admixture of $K_1(1270)$ and $K_1(1400)$, expression providing bounds on α - α_{eff} can be derived [11]. For this reason a CP-averaged rate for $B^0 \to a_1^\pm(1260)\,K^\mp$ is necessary to estract α; how this measurement can be performed will be presented.

---

of mesons $B\overline{B}$ (50% neutral $B\overline{B}$ and 50% charged $B\overline{B}$). Quantum numbers of this resonance are $J^{CP}{=}1^{--}$.

[4]b-factory is usual expression to describe an accelerator that is able to produce a large number of B mesons (greater than 10^7 B for year).

Chapter 1

CP Violation in the B Meson System

1.1 Overview of CP Violation

1.1.1 Discrete Symmetries

The set of operators on the Hilbert space of state functions on the quantum field contains both discrete and continuous transformations that preserve the Minkowski interval $t^2 - \vec{x}^2$. The set of continuous transformations that preserve this interval are the familiar Lorentz transformations, comprised of the product space of rotations, translations, and Lorentz boosts. The three independent discrete transformations that also preserve $t^2 - \vec{x}^2$ are the charge conjugation operator (C), the parity operator (P), and the time-reversal operator (T). These form a complete set of discrete Minkowski interval-preserving transformations of the Hilbert space. Although other discrete interval-preserving transformations exist in the Standard Model (SM) [12, 13, 14], all can be formed from C, P, T, and the group of continuous Lorentz and gauge rotations.[1] The action of the three discrete transformations on, as an example, the special case of a spin 1/2 (Dirac) field, is discussed below.

Parity

The parity operator $\mathcal{P}$ reverses the signs of the 3 spatial elements of a four-vector: $(t, \vec{x}) \rightarrow (t, -\vec{x})$ and $(E, \vec{p}) \rightarrow (E, -\vec{p})$. One can easily visualize parity as a mirror-

---

[1]For example, consider the set of discrete transformations $M_{\hat{n}}$, which takes the mirror image of space with respect to a plane defined by a unit vector $\hat{n}$. This is simply parity combined with a rotation of π about $\hat{n}$. Minimal supersymmetry adds a single independent Lorentz-invariant transformation (R-parity), of which the symmetry is broken at observable energy levels, producing mass differences.

image plus an 180-degree rotation normal to the plane of the mirror (which works for any mirror angle) — this reverses the momentum of a particle but leaves its spin unchanged:
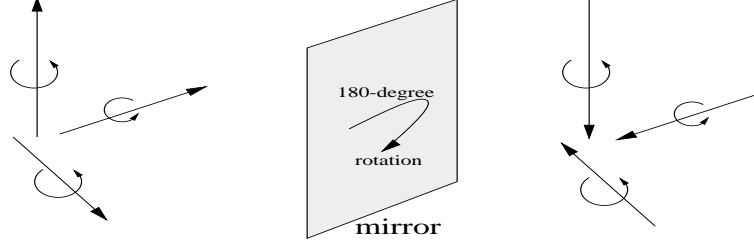

Figure 1.1: Effects of P symmetry

Consider the action of parity on the particle and antiparticle annihilation operators of the Dirac field $a_{\vec{p}}^s$ and $b_{\vec{p}}^s$. Parity should transform the states $a_{\vec{p}}^s|0\rangle$ and $b_{\vec{p}}^s|0\rangle$ to $a_{-\vec{p}}^s|0\rangle$ and $b_{-\vec{p}}^s|0\rangle$ as shown in the figure above. This implies

$$\mathcal{P}a_{\vec{p}}^s\mathcal{P}^{-1} = \eta_a a_{-\vec{p}}^s \qquad \text{and} \qquad \mathcal{P}b_{\vec{p}}^s\mathcal{P}^{-1} = \eta_b b_{-\vec{p}}^s \tag{1.1}$$

where η_a and η_b are phases. Since $\mathcal{P}^2 = \mathbf{1} \Rightarrow \eta_a, \eta_b$ must equal ± 1 (the parity group, as with the other two discrete operators, is idempotent, *ie.* $\mathcal{P}^{-1} = \mathcal{P}$, so the equation above could just as easily have been written $\mathcal{P}a_{\vec{p}}^s\mathcal{P}$, etc.). To find the matrix representation of $\mathcal{P}$ and the phases η_a and η_b, consider the action of $\mathcal{P}$ on $\phi(x)$. Decomposing ϕ into eigenstates of spin and momentum gives:

$$\mathcal{P}\phi(x)\mathcal{P}^{-1} = \frac{1}{\sqrt{2E_{\vec{p}}}} \int \frac{d^3p}{(2\pi)^3} \sum_s \left(\eta_a a_{-\vec{p}}^s u^s(p)e^{-ipx} + \eta_b^* b_{-\vec{p}}^{s\dagger} v^s(p)e^{ipx} \right) \tag{1.2}$$

The key is to change variables to (not surprisingly) $p' = (p^0, -\vec{p}) \Rightarrow p \cdot x = p' \cdot (t, -\vec{x})$ and $p' \cdot \sigma$ (where σ is the four-vector of 2×2 Pauli matrices) $= p \cdot \sigma^\dagger \gamma^0$ (where γ^0 is the 0-th Dirac matrix) $= p \cdot \overline{\sigma}$, where

$$\overline{\sigma} \equiv \sigma^\dagger \gamma^0 \tag{1.3}$$

Thus the four-spinors $u(p)$ and $v(p)$ can be written as:

$$u(p) = \begin{pmatrix} \sqrt{p \cdot \sigma}\varsigma \\ \sqrt{p \cdot \overline{\sigma}}\varsigma \end{pmatrix} = \begin{pmatrix} \sqrt{p' \cdot \overline{\sigma}}\varsigma \\ \sqrt{p' \cdot \sigma}\varsigma \end{pmatrix} = \gamma^0 u(p')$$

$$v(p) = \begin{pmatrix} \sqrt{p \cdot \sigma}\varsigma \\ -\sqrt{p \cdot \overline{\sigma}}\varsigma \end{pmatrix} = \begin{pmatrix} \sqrt{p' \cdot \overline{\sigma}}\varsigma \\ -\sqrt{p' \cdot \sigma}\varsigma \end{pmatrix} = -\gamma^0 v(p') \tag{1.4}$$

where ς is a generic two-component spinor. Thus (1.2) can be written as:

$$\mathcal{P}\phi(x)\mathcal{P}^{-1} = \frac{1}{\sqrt{2E_{\vec{p}}}} \int \frac{d^3 p'}{(2\pi)^3} \sum_s \left(\eta_a a_{\vec{p}'}^s \gamma^0 u^s(p') e^{-ip' \cdot (t, -\vec{x})} \right.$$
$$\left. - \eta_b^* b_{\vec{p}'}^{s\dagger} \gamma^0 v^s(p') e^{ip' \cdot (t, -\vec{x})} \right) \tag{1.5}$$

But,

$$\phi(t, -\vec{x}) = \frac{1}{\sqrt{2E_{\vec{p}}}} \int \frac{d^3 p'}{(2\pi)^3} \sum_s \left(a_{\vec{p}'}^s u^s(p') e^{-ip' \cdot (t, -\vec{x})} \right.$$
$$\left. + b_{\vec{p}'}^{s\dagger} v^s(p') e^{ip' \cdot (t, -\vec{x})} \right) \tag{1.6}$$

$\Rightarrow \eta_a = 1$, $\eta_b = -1$, and

$$\mathcal{P}\phi(t, \vec{x})\mathcal{P}^{-1} = \gamma^0 \phi(t, -\vec{x}) \tag{1.7}$$

Time Reversal

The time reversal operator reverses momentum and spin and also flips the sign of the time component of a state. Therefore we want the transformation of the Dirac particle and antiparticle annihilation operators to be:

$$\mathcal{T} a_{\vec{p}}^s \mathcal{T}^{-1} = \eta_a' a_{-\vec{p}}^{-s} \qquad \text{and} \qquad \mathcal{T} b_{\vec{p}}^s \mathcal{T}^{-1} = \eta_b' b_{-\vec{p}}^{-s} \tag{1.8}$$

We can start to compute the transformation of the fermion field ϕ:

$$\mathcal{T}\phi(t, \vec{x})\mathcal{T}^{-1} = \frac{1}{\sqrt{2E_{\vec{p}}}} \int \frac{d^3 p}{(2\pi)^3} \sum_s \mathcal{T} \left(a_{\vec{p}}^s u^s(p) e^{-ipx} + b_{\vec{p}}^{s\dagger} v^s(p) e^{ipx} \right) \mathcal{T}^{-1} \tag{1.9}$$

However, if $\mathcal{T}$ were to only act on the operators a and b, the situation would be the same as with parity and the spatial coordinates would flip sign instead of time (also the operators would reverse spin but not the spinors, which would be an unphysical nonlinearity). $\mathcal{T}$ therefore must act on more than just the operators.

The solution is to let $\mathcal{T}$ act on complex numbers in addition to operators. Let

$$\mathcal{T}z = z^*\mathcal{T} \quad \forall z \text{ in } \mathcal{C} \tag{1.10}$$

Thus (1.9) becomes

$$\frac{1}{\sqrt{2E_{\vec{p}}}} \int \frac{d^3p}{(2\pi)^3} \sum_s \left(\eta_a'^* a_{-\vec{p}}^{-s} (u^s(p))^* e^{ipx} + \eta_b'^* b_{-\vec{p}}^{-s\dagger} (v^s(p))^* e^{-ipx} \right) \tag{1.11}$$

We need to find a constant matrix $\mathcal{M}$ such that $\mathcal{M}u^{-s}(p') = (u^s(p))^*$ (and similarly for $v^s(p)$) — then we can change variables to p' and $(-t, \vec{x})$ so that we can obtain an answer for the action of the transformation in terms of $\phi(-t, \vec{x})$.

We can see that:

$$(u^s(p))^* = \begin{pmatrix} \sqrt{p \cdot \sigma^*} \varsigma^{s*} \\ \sqrt{p \cdot \overline{\sigma}^*} \varsigma^{s*} \end{pmatrix} = \begin{pmatrix} \sigma^2 & 0 \\ 0 & \sigma^2 \end{pmatrix} \begin{pmatrix} \sigma^2 & 0 \\ 0 & \sigma^2 \end{pmatrix} \begin{pmatrix} \sqrt{p \cdot \sigma^*} \varsigma^{s*} \\ \sqrt{p \cdot \overline{\sigma}^*} \varsigma^{s*} \end{pmatrix} =$$
$$-\gamma^1 \gamma^3 \begin{pmatrix} -i\sigma^2 \sqrt{p \cdot \sigma^*} \varsigma^{s*} \\ -i\sigma^2 \sqrt{p \cdot \overline{\sigma}^*} \varsigma^{s*} \end{pmatrix} \tag{1.12}$$
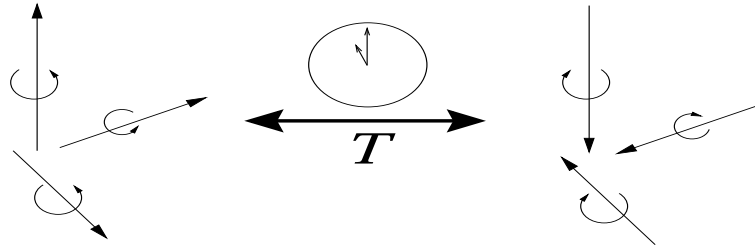
and can then use the identity

Figure 1.2: Effects of T symmetry

$$\sigma^2 \sqrt{p \cdot \sigma^*} = \sqrt{p' \cdot \sigma}\, \sigma^2 \tag{1.13}$$

and the fact that

$$-i\sigma^2 \varsigma^{s*} = \begin{pmatrix} 0 & 1 \\ -1 & 0 \end{pmatrix} \begin{pmatrix} \varsigma^{1*} \\ \varsigma^{2*} \end{pmatrix} = \begin{pmatrix} \varsigma^{2*} \\ -\varsigma^{1*} \end{pmatrix} = \varsigma^{-s} \tag{1.14}$$

to obtain for (1.13):

$$-\gamma^1 \gamma^3 \begin{pmatrix} \sqrt{p' \cdot \sigma}(-i\sigma^2 \varsigma^{s*}) \\ \sqrt{p' \cdot \overline{\sigma}}(-i\sigma^2 \varsigma^{s*}) \end{pmatrix} = -\gamma^1 \gamma^3 \begin{pmatrix} \sqrt{p' \cdot \sigma}\varsigma^{-s} \\ \sqrt{p' \cdot \overline{\sigma}}\varsigma^{-s} \end{pmatrix} = -\gamma^1 \gamma^3 u^{-s}(p') \tag{1.15}$$

and similarly for $(v^s(p))^*$. Thus (1.15) becomes

$$-\gamma^1 \gamma^3 \frac{1}{\sqrt{2E_{\vec{p}'}}} \int \frac{d^3 p'}{(2\pi)^3} \sum_s \left(\eta_a'^* a_{\vec{p}'}^{-s} u^s(p') e^{-ip'\cdot(-t,\vec{x})} \right.$$

$$\left. + \eta_b'^* b_{\vec{p}'}^{-s\dagger} v^s(p') e^{ip'\cdot(-t,\vec{x})} \right) \Rightarrow$$

$$\mathcal{T}\phi(t,\vec{x})\mathcal{T}^{-1} = -\gamma^1 \gamma^3 \phi(-t,\vec{x}) \tag{1.16}$$

Charge Conjugation

The charge conjugation operator is defined to be the transformation of a particle into its antiparticle without changing momentum or spin. Thus,

$$\mathcal{C}a_{\vec{p}}^s \mathcal{C}^{-1} = \eta_a'' b_{\vec{p}}^s \qquad \text{and} \qquad \mathcal{C}b_{\vec{p}}^s \mathcal{C}^{-1} = \eta_b'' a_{\vec{p}}^s \tag{1.17}$$

so the transformation of the Dirac field is

$$\mathcal{C}\phi(x)\mathcal{C}^{-1} = \frac{1}{\sqrt{2E_{\vec{p}}}} \int \frac{d^3 p}{(2\pi)^3} \sum_s \left(b_{\vec{p}}^s u^s(p) e^{-ipx} + a_{\vec{p}}^{s\dagger} v^s(p) e^{ipx} \right) \tag{1.18}$$

We want to find what this is in terms of $\overline{\phi} = \phi^\dagger \gamma^0$, so we need a relation between $u^s(p)$ and $v^{s*}(p)$, and between $v^s(p)$ and $u^{s*}(p)$:

$$u^{s*}(p) = \begin{pmatrix} \sqrt{p \cdot \sigma^*}\varsigma^{s*} \\ \sqrt{p \cdot \overline{\sigma}^*}\varsigma^{s*} \end{pmatrix} = \begin{pmatrix} \sqrt{p \cdot \sigma^*}\varsigma^{s*} \\ \sqrt{p \cdot \overline{\sigma}^*}\varsigma^{s*} \end{pmatrix} = \begin{pmatrix} i\sqrt{p \cdot \sigma^*}\sigma^2\varsigma^{-s} \\ i\sqrt{p \cdot \overline{\sigma}^*}\sigma^2\varsigma^{-s} \end{pmatrix} \qquad (1.19)$$

However, from the identity (1.13) we can see that:

$$\sqrt{p \cdot \sigma^*}\sigma^2 = \sigma^2\sqrt{p \cdot \overline{\sigma}} \qquad \text{and}$$
$$\sqrt{p \cdot \overline{\sigma}^*}\sigma^2 = \sigma^2\sqrt{p \cdot \sigma} \qquad\qquad (1.20)$$

Thus,

$$u^{s*}(p) = \begin{pmatrix} i\sigma^2\sqrt{p \cdot \overline{\sigma}}\varsigma^{-s} \\ i\sigma^2\sqrt{p \cdot \sigma}\varsigma^{-s} \end{pmatrix} = \begin{pmatrix} 0 & -i\sigma^2 \\ i\sigma^2 & 0 \end{pmatrix} \begin{pmatrix} \sqrt{p \cdot \sigma}\varsigma^{-s} \\ -\sqrt{p \cdot \overline{\sigma}}\varsigma^{-s} \end{pmatrix} = -i\gamma^2 v^s(p). \qquad (1.21)$$

Similarly, $v^{s*}(p) = -i\gamma^2 u^s(p)$, so (1.18) becomes:

$$\begin{aligned} \mathcal{C}\phi(x)\mathcal{C}^{-1} &= \frac{1}{\sqrt{2E_{\vec{p}}}} \int \frac{d^3p}{(2\pi)^3} \sum_s \left(i\gamma^2 b_{\vec{p}}^s v^{s*}(p)e^{-ipx} + i\gamma^2 a_{\vec{p}}^{s\dagger} u^{s*}(p)e^{ipx} \right) \\ &= i\gamma^2 \phi^*(x) = i(\overline{\phi}\gamma^0\gamma^2)^T \end{aligned} \qquad (1.22)$$

CPT

The combination $\mathcal{CPT}$ operator has a rather special property: it is guaranteed to be a fundamental symmetry of nature, with only the basic assumptions of Lorentz invariance, locality, and the spin-statistics relation.[2] A proof for the restricted case of the Dirac field follows.

It's summarized and shown in the Table 1.1 how scalars, pseudoscalars, vectors, pseudovectors, and tensors are affected by the discrete symmetries:

The Lagrangian $\mathcal{L}$ is a Lorentz scalar, and as we can see above, any contraction of indices to form a Lorentz scalar must result in an eigenstate with a +1 $\mathcal{CPT}$ eigenvalue.

---

[2]Note that the spin-statistics relation itself is implied from Lorentz invariance, positive energies, positive norms, and causality.

	$\mathcal{C}$	$\mathcal{P}$	$\mathcal{T}$	$\mathcal{CP}$	$\mathcal{CPT}$
Scalar	$+1$	$+1$	$+1$	$+1$	$+1$
Pseudoscalar	$+1$	-1	-1	-1	$+1$
Vector	$\vec{-1}$	$\begin{pmatrix} +1 \\ -1 \\ -1 \\ -1 \end{pmatrix}$	$\begin{pmatrix} +1 \\ -1 \\ -1 \\ -1 \end{pmatrix}$	$\begin{pmatrix} -1 \\ +1 \\ +1 \\ +1 \end{pmatrix}$	$\vec{-1}$
Pseudovector	$\vec{+1}$	$\begin{pmatrix} -1 \\ +1 \\ +1 \\ +1 \end{pmatrix}$	$\begin{pmatrix} +1 \\ -1 \\ -1 \\ -1 \end{pmatrix}$	$\begin{pmatrix} -1 \\ +1 \\ +1 \\ +1 \end{pmatrix}$	$\vec{-1}$
Tensor	-1	$\begin{pmatrix} +1 & -1 & -1 & -1 \\ -1 & +1 & +1 & +1 \\ -1 & +1 & +1 & +1 \\ -1 & +1 & +1 & +1 \end{pmatrix}$	$\begin{pmatrix} -1 & +1 & +1 & +1 \\ +1 & -1 & -1 & -1 \\ +1 & -1 & -1 & -1 \\ +1 & -1 & -1 & -1 \end{pmatrix}$	$\begin{pmatrix} -1 & +1 & +1 & +1 \\ +1 & -1 & -1 & -1 \\ +1 & -1 & -1 & -1 \\ +1 & -1 & -1 & -1 \end{pmatrix}$	$+1$
Derivative Operator	$\vec{+1}$	$\begin{pmatrix} +1 \\ -1 \\ -1 \\ -1 \end{pmatrix}$	$\begin{pmatrix} -1 \\ +1 \\ +1 \\ +1 \end{pmatrix}$	$\begin{pmatrix} +1 \\ -1 \\ -1 \\ -1 \end{pmatrix}$	$\vec{-1}$

Table 1.1: Summary of discrete symmetries for scalars, pseudoscalars, vectors, pseudovectors and tensors.

1.1.2 CP

The CP transformation properties of the fermion field bilinears are listed in the column next to CPT. As we can see, if we restrict our attention to scalars, pseudoscalars, vectors, and the derivative operator, a Lagrangian formed from only such quantities must remain CP-invariant. Thus a massless spin 1/2 field with real coupling constants cannot violate CP. This is in fact true for quantum fields of any spin. Charge conjugation ensures that the fields themselves transform to their Hermitian conjugates (we have seen this above for the special case of spin 1/2). However, particle masses and coupling constants do not transform under CP (as complex numbers such as these are only transformed by, of the discrete operators, $\mathcal{T}$, as previously seen). If any of these quantities is not purely real, it will suffer a phase shift relative to the quantities that are transformed by CP, thus potentially violating CP symmetry.

Such phase differences must be robust against gauge modifications in order to manifest themselves as CP violation. If simple redefinitions of the phases of any of

the fields can remove overall phases in each field coupling, the theory remains *CP*-conserving. As will be shown in Section 1.4, if only two fermion generations are present, such a redefinition always exists, hence the Kobayashi-Maskawa prediction of a third generation. The effect of irreducible *CP*-violating phases will be elucidated in the following sections.

1.2 Mixing and Time Evolution of Neutral Mesons

The four pairs of conjugate neutral mesons that decay weakly, K^0, D^0, B^0, and B_s, can each mix with their respective antiparticle via a pair of box diagrams:
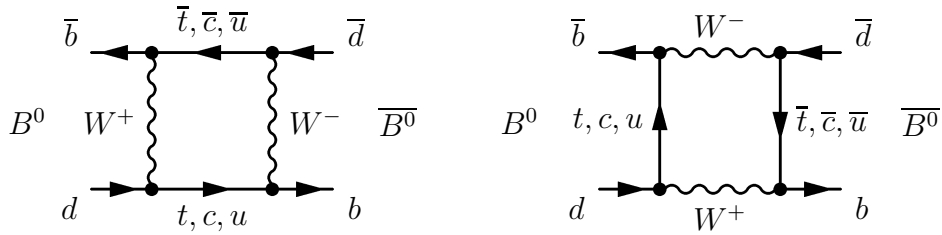
Figure 1.3: Feynman diagrams mixing $B^0 - \overline{B}^0$.

The ability to mix implies that the flavor eigenstates may not be equivalent to the mass eigenstates; the observed presence of mixing (into conjugate flavor-specific decays) implies that the mass and flavor eigenstates are in fact different.

Lack of *CP* symmetry implies a third set of eigenstates, *CP* eigenstates, which can differ from the mass and flavor eigenstates, as will be seen below.

1.2.1 Mixing of a "Generic" Neutral Meson

Consider a weakly-decaying neutral meson X^0 (which could be any of K^0, D^0, B^0 or B_s). An arbitrary linear combination of the flavor eigenstates

$$\alpha|X^0\rangle + \beta|\overline{X}^0\rangle \tag{1.23}$$

mixes according to the time-dependent Schrödinger equation

$$
i\frac{\partial}{\partial t}\begin{pmatrix}\alpha \\ \beta\end{pmatrix} = \mathcal{H}\begin{pmatrix}\alpha \\ \beta\end{pmatrix} \equiv \begin{pmatrix} m_{11} - \frac{1}{2}i\gamma_{11} & m_{12} - \frac{1}{2}i\gamma_{12} \\ m_{21} - \frac{1}{2}i\gamma_{21} & m_{22} - \frac{1}{2}i\gamma_{22} \end{pmatrix}\begin{pmatrix}\alpha \\ \beta\end{pmatrix} \tag{1.24}
$$

The m and γ parts represent the mixing and decay parts, respectively, of the time dependence. Each of the off-diagonal elements can be complex: the angle in the complex plane of m_{12} represents the phase of the mixing, and γ_{12} represents the (complex) coupling to common decay modes of X^0 and $\overline{X}^0$ (for example, $B^0/\overline{B}^0 \to J/\psi K_S^0$ or $\pi^+\pi^-$). We can see that CPT invariance guarantees that $m_{11} = m_{22}$ and $\gamma_{11} = \gamma_{22}$, and that $m_{21} = m_{12}^*$ and $\gamma_{21} = \gamma_{12}^*$ — the CPT-conjugate pairs of equations are:

$$
\begin{aligned}
i\frac{\partial\alpha}{\partial t} &= (m_{11} - \frac{1}{2}i\gamma_{11})\alpha + (m_{12} - \frac{1}{2}i\gamma_{12})\beta \\
i\frac{\partial\beta}{\partial t} &= (m_{21} - \frac{1}{2}i\gamma_{21})\alpha + (m_{22} - \frac{1}{2}i\gamma_{22})\beta
\end{aligned} \tag{1.25}
$$

and

$$
\begin{aligned}
i\frac{\partial\beta}{\partial t} &= (m_{11} - \frac{1}{2}i\gamma_{11})\beta + (m_{12}^* - \frac{1}{2}i\gamma_{12}^*)\alpha \\
i\frac{\partial\alpha}{\partial t} &= (m_{21}^* - \frac{1}{2}i\gamma_{21}^*)\beta + (m_{22} - \frac{1}{2}i\gamma_{22})\alpha
\end{aligned} \tag{1.26}
$$

which must be equivalent. Thus, setting m_{11} and m_{22} to m and γ_{11} and γ_{22} to γ, we have:

$$
i\frac{\partial}{\partial t}\begin{pmatrix}\alpha \\ \beta\end{pmatrix} = \begin{pmatrix} m - \frac{1}{2}i\gamma & m_{12} - \frac{1}{2}i\gamma_{12} \\ m_{12}^* - \frac{1}{2}i\gamma_{12}^* & m - \frac{1}{2}i\gamma \end{pmatrix}\begin{pmatrix}\alpha \\ \beta\end{pmatrix} \tag{1.27}
$$

The mass eigenstates are the eigenvectors of the Hamiltonian:

$$
\begin{aligned}
|X_L\rangle &= p|X^0\rangle + q|\overline{X}^0\rangle \\
|X_H\rangle &= p|X^0\rangle - q|\overline{X}^0\rangle
\end{aligned} \tag{1.28}
$$

where $|X_L\rangle$ and $|X_H\rangle$ are the lighter and heavier mass eigenstates,

$$q = \sqrt{\frac{m_{12}^* - \frac{1}{2}i\gamma_{12}^*}{m_{12} - \frac{1}{2}i\gamma_{12}}} p \qquad (1.29)$$

and $\qquad |p|^2 + |q|^2 = 1. \qquad (1.30)$

The difference in the magnitude of q/p from 1 is reponsible for CP-violation that is purely due to mixing — this will be discussed in section 1.3.2. The mass difference $\Delta m = m_H - m_L$ and decay width difference $\Delta\Gamma = \Gamma_H - \Gamma_L$ can also be obtained by diagonalizing the "mixing matrix" shown in Equation 1.27. Let

$$\alpha = |m_{12}|^2 - \frac{1}{4}|\gamma_{12}|^2, \qquad \beta = \mathcal{R}e(m_{12}\gamma_{12}^*) \qquad (1.31)$$

then,

$$\Delta m = \sqrt{2\alpha - 2\sqrt{\alpha^2 - \beta^2}} \qquad (1.32)$$

and

$$\Delta\Gamma = 4\beta/\Delta m \qquad (1.33)$$

An initially pure $|X^0\rangle$ state will, therefore, time evolve as a superposition of the mass eigenstates $|X_L\rangle$ and $|X_H\rangle$. Equation 1.29 may thus also be expressed as

$$q = \left(\frac{\Delta m - \frac{i}{2}\Delta\Gamma}{2(m_{12} - \frac{1}{2}i\gamma_{12})}\right) p \qquad (1.34)$$

1.2.2 The Neutral K System

Mixing between the two neutral K weak eigenstates K^0 and $\overline{K}^0$ was first predicted in 1955 by Gell-Mann and Pais [15]. The two physical states, $|K_1\rangle = \frac{1}{\sqrt{2}}(K^0 + \overline{K}^0)$ and $|K_2\rangle = \frac{1}{\sqrt{2}}(K^0 - \overline{K}^0)$, would thus be CP eigenstates with eigenvalues $+1$ and -1. The dominant decay of neutral K mesons is $\pi^+\pi^-$, due to helicity constraints and the fact the 3-body phase space is strongly suppressed at these mass scales (due to the well-known $(\Delta m)^5$ scaling rule). However, $\pi^+\pi^-$ is itself a CP eigenstate with eigenvalue $+1$. Thus, if CP were exactly conserved, *only the $|K_1\rangle$ physical state could decay into it*.

The limited phase space to decays other than $\pi^+\pi^-$ forces the lifetime of the eigen-

state with opposite CP K_2, to be far larger (3 orders of magnitude) than the lifetime of the K_1, thus the nomenclature K_S^0 and K_L^0 (for short and long lifetimes) is used. The lifetime difference is very convenient since it allows for simple experimental separation of the two physical states.

In 1964, Fitch and Cronin made their discovery that K_L^0 can in fact decay into $\pi^+\pi^-$ with a branching fraction of 2×10^{-3} (see the Introduction). Since CP is thus not strictly conserved, the general formalism detailed in the previous subsection must be used. Thus we have

$$\begin{aligned} |K_S\rangle &= p|K^0\rangle + q|\overline{K}^0\rangle \\ |K_L\rangle &= p|K^0\rangle - q|\overline{K}^0\rangle \end{aligned} \tag{1.35}$$

where p and q are commonly parametrized as:

$$p = \frac{1 + \epsilon}{\sqrt{2(1 + |\epsilon|^2)}}; \qquad q = \frac{1 - \epsilon}{\sqrt{2(1 + |\epsilon|^2)}} \tag{1.36}$$

The real part of ϵ is a measure of CP violation purely in mixing whereas the imaginary part is a measure of CP violation in the interference between mixing and decay (see the following section). The former is simplest to measure experimentally and was the effect seen in the orginal 1964 discovery. Since, in the K system, $\Delta\Gamma$ is of the same order as Δm, these effects are of similar magnitude, quite unlike the neutral B system, where the latter is far more prevalent.

1.2.3 The Neutral B System

In the case of neutral B mesons, in contrast with the neutral K system, the lifetime difference $\Delta\Gamma$ between the two mass eigenstates is *small* compared with the mixing frequency due to the difference in masses Δm. This difference in behavior of the K and B is due to the larger mass of the B meson and thus far greater phase space for flavor-specific decays in the B system, which dominate the partial width (in contrast to the K system) and give equivalent contributions (by CPT symmetry) to the width of both neutral B eigenstates. The resulting lack of decay suppression of either eigenstate implies nearly equivalent lifetimes.

Due to this simplification in formalism, the time evolution of neutral B mesons

which are initially created (at time $t = 0$) as pure flavor eigenstates can be written as:

$$|B^0_{phys}(t)\rangle = f_+(t)|B^0\rangle + (q/p)f_-(t)|\overline{B}\,^0\rangle \tag{1.37}$$

$$|\overline{B}\,^0_{phys}(t)\rangle = f_+(t)|B^0\rangle + (q/p)f_-(t)|\overline{B}\,^0\rangle \tag{1.38}$$

where

$$f_+(t) = e^{-imt}e^{-\Gamma t/2}\cos(\Delta mt/2) \tag{1.39}$$

$$f_-(t) = e^{-imt}e^{-\Gamma t/2}i\sin(\Delta mt/2) \tag{1.40}$$

This approximation holds up to the condition that

$$\Delta\Gamma \ll \Delta m \tag{1.41}$$

Since $\Delta\Gamma = \mathcal{O}(10^{-3})\Delta m$ in the B system, corrections to it are not considered in CP asymmetry measurements with the current statistics (furthermore, *BABAR* will have the capability of measuring $\Delta\Gamma$ as statistics of reconstructed B decays increase).

1.3   Three Types of CP Violation

Three types of CP violation can potentially be observed at B physics experiments:[3]
1) CP violation in decay (often referred to as direct CP violation): this occurs when multiple amplitudes with different weak phases as well as different strong phases contribute to a given final state, the result is visible as differing magnitude of the amplitude to a decay versus its CP conjugate.
2) CP violation purely in mixing: this occurs when the mass eigenstates of a neutral meson are different from the CP eigenstates.
3) CP violation in the interference between decays of mixed and unmixed mesons: this occurs for decays which are common to a neutral meson and its antiparticle.

1.3.1 CP **Violation in Decay (Direct CP Violation)**

Direct CP violation manifests itself as a difference in the magnitude of the amplitude to a given decay as compared with its CP conjugate, thus resulting in differing rates to

---

[3]There can be other manifestations of CP violation, *e.g.* CP violation in interaction, however observable CP violation at B-factories can all be classified into the 3 categories.

the two elements of the CP conjugate pair. It can occur for both neutral and charged decays.[4] Amplitudes from B^0 and $\overline{B}^0$ to a final state and its CP conjugate may be written as

$$A_f = \sum_i A_i e^{i(\phi_i + \delta_i)} \qquad \text{and} \qquad \overline{A}_{\overline{f}} = \eta_f \sum_i A_i e^{i(-\phi_i + \delta_i)} \tag{1.42}$$

where η_f is the CP eigenvalue (multiplied by a convention-dependent phase) if f is a CP eigenstate, ϕ are the weak phases, and δ are the strong phases. CP violation can only occur when the different weak phase contributions also have different strong phases (or else a simple rotation can remove the strong phase and thus the ratio would clearly have unit magnitude). It can also only occur when weak phases are nontrivial, *i.e.* when exists a relative phase between them (that is therefore irreducible by a rotation of the Lagrangian). Only when both different weak phases *and* different strong phases are present can one have the condition:

$$|\overline{A}_{\overline{f}}/A_f| \neq 1 \tag{1.43}$$

This is CP violation in decay. CP violation in decay has been observed in the kaon system and recently in the B system too. Since the strong phases that enter into measurements of CP violation in decay involve hadronic uncertainties, the relation of such measurements to CKM factors (see next section) cannot be calculated from first principles, but the strong phases may themselves be measured if the CKM factors are known from other measurements. These strong phase measurements can then be used as inputs to other measurements which have equivalent strong phases (thus allowing the extraction of other parameters), and thus measurements of CP violation in decay can (indirectly) provide a useful handle on fundamental quantities.

1.3.2 CP Violation Purely in Mixing

From section 1.2.1, recall that the mass eigenstates of the neutral meson system are the eigenvectors of the Hamiltonian

$$|X_L\rangle = p|X^0\rangle + q|\overline{X}^0\rangle$$

---

[4]For charged decays, it is the *only* potential manifestation of CP violation.

$$|X_H\rangle = p|X^0\rangle - q|\overline{X}^0\rangle \tag{1.44}$$

where

$$q = \sqrt{\frac{m_{12}^* - \frac{1}{2}i\gamma_{12}^*}{m_{12} - \frac{1}{2}i\gamma_{12}}}\, p \tag{1.45}$$

If q and p have different magnitudes, the CP conjugates of the mass eigenstates clearly will differ from the mass eigenstates themselves by more than a trivial phase. Thus the mass eigenstates will not be CP eigenstates and CP violation will be manifest. CP violation from

$$|q/p| \neq 1 \tag{1.46}$$

is purely an effect of mixing and is independent of decay mode. Thus it may be referred to as CP violation purely in mixing.

In neutral B decays, as discussed in section 1.2.2, this effect is expected to be very small. Since

$$\Delta m = \mathcal{O}(10^3)\Delta\Gamma \tag{1.47}$$

this implies that

$$|m_{12}| \gg |\gamma_{12}| \tag{1.48}$$

and thus the factor in equation 1.34 simplifies to a near-phase. CP violation purely in mixing should thus only enter the neutral B system at the 10^{-3} level. An asymmetry in the measurements of the overall rate to flavor tagged B^0 vs. $\overline{B}^0$ would be a signature of CP violation purely in mixing. With greater statistics, evidence for this may be seen; at present, experimental limits exist. It has been clearly observed, however, in the neutral kaon system (where it is the prevalent effect); the discovery of CP violation in 1964 was a detection of CP violation purely in mixing (see Section 1.2.2).

1.3.3 CP **Violation in Interference Between Decays of Mixed and Unmixed Mesons**

Final states which may be reached from either B^0 or $\overline{B}^0$ decays can exhibit a third type of CP violation, which results from the interference between the decays of mixed and of unmixed neutral B mesons which both decay to the final state. Consider the

CP-violating asymmetry in rates between B^0 and $\overline{B}^{\,0}$ as a function of time:

$$a_{CP}(t) = \frac{\Gamma(B^0_{phys}(t) \to f) - \Gamma(\overline{B}^0_{phys}(t) \to f)}{\Gamma(B^0_{phys}(t) \to f) + \Gamma(\overline{B}^0_{phys}(t) \to f)} \tag{1.49}$$

To calculate each of the time-dependent rates $\Gamma(t)$, one can form the inner product of equations 1.37 and 1.38 with the final state f and then take the magnitude squared of the resulting amplitudes:

$$
\begin{aligned}
\Gamma(B^0(t) &\to f) \propto \\
|\langle f|\mathcal{H}|B^0(t)\rangle|^2 = \quad & e^{-\Gamma t} \left\{ \cos^2\left(\frac{\Delta mt}{2}\right) |\langle f|\mathcal{H}|B^0\rangle|^2 \right. \\
& + \sin^2\left(\frac{\Delta mt}{2}\right) \left|\frac{q}{p}\right|^2 |\langle f|\mathcal{H}|\overline{B}^{\,0}\rangle|^2 \\
& - \frac{i}{2}\left|\frac{q}{p}\right| e^{-2i\phi_M} \sin(\Delta mt)\langle f|\mathcal{H}|B^0\rangle\langle f|\mathcal{H}|\overline{B}^{\,0}\rangle^* \\
& \left. + \frac{i}{2}\left|\frac{q}{p}\right| e^{2i\phi_M} \sin(\Delta mt)\langle f|\mathcal{H}|B^0\rangle^*\langle f|\mathcal{H}|\overline{B}^{\,0}\rangle \right\}
\end{aligned}
\tag{1.50a}
$$

$$
\begin{aligned}
\Gamma(\overline{B}^{\,0}(t) &\to f) \propto \\
|\langle f|\mathcal{H}|\overline{B}^{\,0}(t)\rangle|^2 = \quad & e^{-\Gamma t} \left\{ \cos^2\left(\frac{\Delta mt}{2}\right) |\langle f|\mathcal{H}|\overline{B}^{\,0}\rangle|^2 \right. \\
& + \sin^2\left(\frac{\Delta mt}{2}\right) \left|\frac{p}{q}\right|^2 |\langle f|\mathcal{H}|B^0\rangle|^2 \\
& + \frac{i}{2}\left|\frac{p}{q}\right| e^{-2i\phi_M} \sin(\Delta mt)\langle f|\mathcal{H}|B^0\rangle\langle f|\mathcal{H}|\overline{B}^{\,0}\rangle^* \\
& \left. - \frac{i}{2}\left|\frac{p}{q}\right| e^{2i\phi_M} \sin(\Delta mt)\langle f|\mathcal{H}|B^0\rangle^*\langle f|\mathcal{H}|\overline{B}^{\,0}\rangle \right\}
\end{aligned}
\tag{1.50b}
$$

where $2\phi_M$ is the phase of q/p. Since, as shown above, for the B system $|q/p| \approx 1$, we can thus write

$$\langle f|\mathcal{H}|\overline{B}^{\,0}(t)\rangle = \eta e^{-2i\phi_D}|\lambda|\langle f|\mathcal{H}|B^0(t)\rangle \tag{1.51}$$

where ϕ_D is the phase of the decay, η is the CP eigenvalue of f, and

$$\lambda = \frac{q}{p} \frac{\langle f|\mathcal{H}|\overline{B}^0\rangle}{\langle f|\mathcal{H}|B^0\rangle} = |\lambda|e^{-2i(\phi_M+\phi_D)}, \tag{1.52}$$

the expressions simplify greatly:

$$
\begin{aligned}
|\langle f|\mathcal{H}|B^0(t)\rangle|^2 &= A^2 e^{-\Gamma t}\{1 - \mathrm{C}\cos(\Delta mt) - \mathrm{S}\sin(\Delta mt)\} \quad \text{and} \tag{1.53}\\
|\langle f|\mathcal{H}|\overline{B}^0(t)\rangle|^2 &= A^2 e^{-\Gamma t}\{1 + \mathrm{C}\cos(\Delta mt) + \mathrm{S}\sin(\Delta mt)\} \tag{1.54}
\end{aligned}
$$

where $A^2 = |\langle f|\mathcal{H}|B^0\rangle|^2$ and

$$\mathrm{C} = \frac{1-|\lambda|^2}{1+|\lambda|^2} \qquad \text{and} \qquad \mathrm{S} = \eta\frac{-2\sin(2(\phi_M+\phi_D))}{1+|\lambda|^2} \tag{1.55}$$

Thus the time-dependent asymmetry

$$a_{CP}(t) = \frac{\Gamma(B^0_{phys}(t)\to f) - \Gamma(\overline{B}^0_{phys}(t)\to f)}{\Gamma(B^0_{phys}(t)\to f) + \Gamma(\overline{B}^0_{phys}(t)\to f)} = \mathrm{C}\cos(\Delta mt) + \mathrm{S}\sin(\Delta mt) \tag{1.56}$$

In the absence of *CP* violation, S and C must both go to zero, since they occur only when weak phases do not cancel. C is only nonzero when the ratio of the amplitude norms differs from unity, which is the signature of direct *CP* violation (detailed in section 1.3.1). S, however, represents a distinct type of *CP* violation that can occur even in the absence of *CP* violation purely in decay or in mixing. It results from the interference of the decays of mixed mesons with those of unmixed mesons; if the mixing contains a phase that is not cancelled by the decay itself, this observable time-dependent asymmetry above will result. Unlike *CP* violation in decay, no nontrivial strong phases are required.

As will be seen in the next section, *CP* violation in interference between decays of mixed and unmixed mesons is a large effect in the Standard Model picture of the neutral B system. Since this is a measurement of an asymmetry rather than an absolute rate, many experimental and model-dependent uncertainties (such as reconstruction efficiency) that would otherwise contribute to experimental error, instead cancel out in the ratio. Thus it provides an excellent mechanism for precision measurements of *CP* violation and the study of the Standard Model picture of CPV.

1.4 *CP* Violation in the Standard Model

CP violation within the context of the Standard Model $SU(2) \times U(1)$ electroweak symmetry was introduced by Kobayashi and Maskawa in 1973 via the postulation of a third family of quarks. This occurred a year prior to the discovery of charm; only 3 quarks existed at the time, so the prediction was quite prescient. The b-quark was then first observed in 1977. The prediction of additional quarks did not occur entirely without precedent, however. Theoretical interpretation of quark mixing via the weak interaction has closely followed experimental result, and the development of the 3 x 3 CKM matrix and its *CP* violating phase was a steady and piecewise process.

1.4.1 Weak Interactions and the CKM Matrix

The observed suppression of flavor-changing neutral current decays indicates that the quark sector is separated into families, similar to the lepton sector. However, lepton flavor is conserved,[5] whereas quark generation is manifestly violated (*e.g.* in weak decays of kaons). However, strangeness-changing decays have an additional suppression compared with strangeness-conserving weak decays. This "Cabibbo factor" may be accounted for by considering that, similar to neutral mesons, the quark mass eigenstates differ from the weak eigenstates. Thus a mixing matrix describing transitions between quark generations is necessary.

Such a matrix must be unitary since quark number is manifestly conserved.[6] With 2 generations, a unitary matrix can be described by a single parameter Θ_c:

$$\begin{pmatrix} d_{mass} \\ s_{mass} \end{pmatrix} = \begin{pmatrix} \cos\Theta_c & \sin\Theta_c \\ -\sin\Theta_c & \cos\Theta_c \end{pmatrix} \begin{pmatrix} d \\ s \end{pmatrix} \tag{1.57}$$

where d_{mass} and s_{mass} are the mass eigenstates nearest to the flavor eigenstates d and s respectively.

The same matrix (experimentally) holds for the (u, c) quark pair (although the c quark was of course discovered afterwards in 1974, four years after its prediction via the GIM mechanism that required charm to explain the absence of weak flavor-changing neutral currents[16]). The Cabbibo angle Θ_c is thus a full description of 2-generation mixing.

---

[5]Discounting, for the purposes of this document, recently discovered neutrino oscillations and thus lepton mixing.

[6]in contrast with the number of neutral mesons

More generally, we can write the charged-current coupling j_{cc} with 2 generations as

$$j_{cc}^{\mu} = \left(\begin{array}{cc} \overline{u} & \overline{c} \end{array}\right) \gamma^{\mu}(1-\gamma^5) \left(\begin{array}{c} d_{mass} \\ s_{mass} \end{array}\right) = \left(\begin{array}{cc} \overline{u} & \overline{c} \end{array}\right) \gamma^{\mu}(1-\gamma^5) V_{ij} \left(\begin{array}{c} d \\ s \end{array}\right) \quad (1.58)$$

where $V_{i}j$ is the 2 x 2 Cabbibo matrix parametrized by Θ_c above. With an arbitrary number of generations, the charged current ($W^{\pm}$) Lagrangian becomes:

$$\mathcal{L}_W = \frac{g}{\sqrt{2}} \left\{ \overline{u}_i^L \gamma^{\mu} W_{\mu}^+ V_{ij} d_j^L + \overline{d}_i^L \gamma^{\mu} W_{\mu}^- V_{ij}^* u_j^L \right\} \quad (1.59)$$

with u_i^L representing the vector of up-type quarks and d_i^L representing the down-type quarks. Applying the CP operation to the Lagrangian, one obtains:

$$\mathcal{L}_W = \frac{g}{\sqrt{2}} \left\{ \overline{d}_i^L \gamma^{\mu} W_{\mu}^- V_{ij} u_j^L + \overline{u}_i^L \gamma^{\mu} W_{\mu}^+ V_{ij}^* d_j^L \right\} \quad (1.60)$$

which is exactly the same except for the complex conjugation of V. Thus, if we can find a basis for which V (as well as the quark masses) are real, then CP is a symmetry.

Unitary matrices of dimension N form a group, the Lie group $SO(N)$. Elements of $SO(N)$ may be specified by $N^2 - 2N + 1$ real parameters. With 2 quark generations, V is defined by a single real parameter, the Cabibbo angle Θ_c. However, with 3 quark generations, 4 parameters are required. The real rotations may be taken to be the 3 Euler angles, but this leaves an extra parameter. The extra parameter is an *irreducible* complex phase. If this phase is nonzero, one can no longer find a basis for which V is real. Thus CP would cease to be a symmetry, and indeed that is the case in nature.

1.4.2   Unitarity Conditions and the Unitarity Triangle

Unitarity of the CKM matrix V requires that

$$V^{\dagger} V = V V^{\dagger} = \mathit{1} \quad \Rightarrow \quad \sum_j V_{ji}^* V_{jk} = \sum_j V_{ij} V_{kj}^* = \delta_{ik} \quad (1.61)$$

With a 3-generation CKM matrix

$$V = \begin{pmatrix} V_{ud} & V_{us} & V_{ub} \\ V_{cd} & V_{cs} & V_{cb} \\ V_{td} & V_{ts} & V_{tb} \end{pmatrix} \tag{1.62}$$

this results in 9 independent equations, 3 of which (for the diagonal of the product unit matrix) equal one and 6 of which equal zero. The equations for the off-diagonal elements, each containing a sum of 3 complex numbers which equals 0, will each describe a triangle in the complex plane:

$$V_{cd}V_{ud}^* + V_{cs}V_{us}^* + V_{cb}V_{ub}^* = 0 \tag{1.63a}$$

$$V_{cd}V_{td}^* + V_{cs}V_{ts}^* + V_{cb}V_{tb}^* = 0 \tag{1.63b}$$

$$V_{ud}V_{td}^* + V_{us}V_{ts}^* + V_{ub}V_{tb}^* = 0 \tag{1.63c}$$

$$V_{us}^*V_{ud} + V_{cs}^*V_{cd} + V_{ts}^*V_{td} = 0 \tag{1.63d}$$

$$V_{ub}^*V_{us} + V_{cb}^*V_{cs} + V_{tb}^*V_{ts} = 0 \tag{1.63e}$$

$$V_{ub}^*V_{ud} + V_{cb}^*V_{cd} + V_{tb}^*V_{td} = 0 \tag{1.63f}$$

The differences between these 6 triangles are purely empirical. There is no theoretical motivation at present for the fact that 4 of them are nearly degenerate and only 2 describe triangles that have each of their sides being the same order of magnitude in length — the 4 parameters that describe the CKM matrix are not predicted by the Standard Model and can only be determined experimentally. It is emprically the case that only equations 1.63c and 1.63f above describe triangles which are not nearly degenerate. Of these, the last equation, 1.63f, is the one that is typically used to pictorially represent the irreducible *CP* violating phase and is referred to as the Unitarity Triangle.

They exist many CKM parametrizations. The standard one uses θ_{12}, θ_{23}, θ_{13} and a phase δ_{13}, called PDG [40] parameterization, given by

$$\mathsf{V} = \begin{pmatrix} c_{12}c_{13} & s_{12}c_{13} & s_{13}e^{-i\delta_{13}} \\ -s_{12}c_{23} - c_{12}s_{23}s_{13}e^{i\delta_{13}} & c_{12}c_{23} - s_{12}s_{23}s_{13}e^{i\delta_{13}} & s_{23}c_{13} \\ s_{12}s_{23} - c_{12}c_{23}s_{13}e^{i\delta_{13}} & -c_{12}s_{23} - s_{12}c_{23}s_{13}e^{i\delta_{13}} & c_{23}c_{13} \end{pmatrix} \tag{1.64}$$

with c_{ij}=cosθ_{ij} and s_{ij}=sinθ_{ij} for quark families labelled with i,j=1,2,3. The empirical
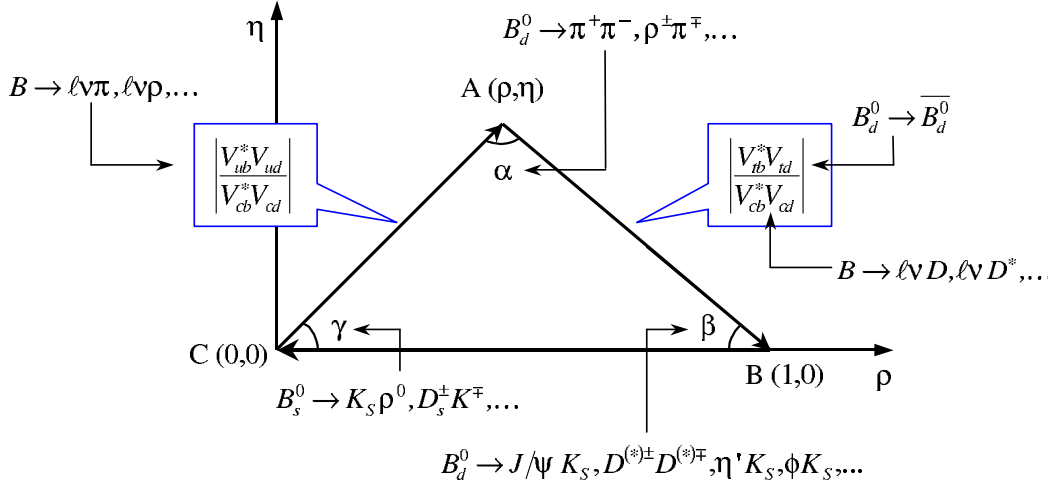
Figure 1.4: Unitary triangle and main decays to measure the sides and the angles.

fact that 4 of the triangles are nearly degenerate allows for a convenient parametrization of the CKM matrix via an expansion around the order parameter $\lambda \equiv s_{12}(= 0.2205 \pm 0.0018)$[7], sinus of Cabibbo's angle and function of real parameters A, λ and complex parameter $\rho + i\eta$:

$$
V = \begin{pmatrix} 1 - \frac{\lambda^2}{2} & \lambda & A\lambda^3(\rho - i\eta) \\ -\lambda & 1 - \frac{\lambda^2}{2} & A\lambda^2 \\ A\lambda^3(1 - \rho - i\eta) & -A\lambda^2 & 1 \end{pmatrix} + \mathcal{O}(\lambda^4) \qquad (1.65)
$$

with (λ, A, ρ, η) as the 4 real parameters describing the CKM matrix, the latter 3 being of order 1. This approximate parameterization, first proposed by Wolfenstein.

Unitary triangle obtained by (1.63f) can be rotated and scaled choosing a conventional phase in a way that $V_{cb}^* V_{cd}$ is real, and so aligning related side to real axis, and dividing lenght of all sides for $|V_{cd}V_{cb}^*|$ so lenght is normalized to 1. Obtained triangle (show in figure 1.4) will have two fixed vertexes at (0,0) and at (1,0) and coordinates of remaining vertex will depends by (ρ,η) corresponding to Wolfenstein's parameters; leghts of complex sides become:

$$
R_u \equiv \left| \frac{V_{ub}V_{ud}}{V_{cb}V_{cd}} \right| = \sqrt{\rho^2 + \eta^2}, \qquad R_t \equiv \left| \frac{V_{tb}V_{td}}{V_{cb}V_{cd}} \right| = \sqrt{(1 - \rho)^2 + \eta^2}. \qquad (1.66)
$$

---

[7]Note that this Cabibbo parameter $\lambda \equiv \sin \Theta_c$ differs from the time-dependent asymmetry parameter λ detailed in Section 1.3.3.

The three angles of out unitary triangle, denoted with α, β and γ, are:

$$\alpha \equiv \arg\left[-\frac{V_{td}V_{tb}^*}{V_{ud}V_{ub}^*}\right], \quad \beta \equiv \arg\left[-\frac{V_{cd}V_{cb}^*}{V_{td}V_{tb}^*}\right], \quad \gamma \equiv \arg\left[-\frac{V_{ud}V_{ub}^*}{V_{cd}V_{cb}^*}\right]. \quad (1.67)$$

These quantities are physical and can be measured from CP asymmetries in B decays. Consistency among different experimental values help in Standard Model verification. Particularly, β angle yields, with a good approximation, Standard Model phase between mixing amplitude of neutral B and their decay amplitude.

1.4.3 Measurement of CKM parameters

We show in the following lines the measurement of CKM parameters and fixing, briefly, processes to evaluate them. More informations can be found in [17].

$|\boldsymbol{V_{ud}}|$: analysis has been done using nuclear β decays:

$$|V_{ud}| = 0.9738 \pm 0.0002. \quad (1.68)$$

$|\boldsymbol{V_{us}}|$: they used semileptonic decays of kaons and hyperons:

$$|V_{us}| = 0.227 \pm 0.001. \quad (1.69)$$

$|\boldsymbol{V_{cd}}|$: due to charm neutrino-antineutrino pairs production:

$$|V_{cd}| = 0.227 \pm 0.001. \quad (1.70)$$

$|\boldsymbol{V_{cs}}|$: from ratio between hadronic decays of W and leptonic decays, measured by LEP:

$$|V_{cs}| = 0.9730 \pm 0.0003. \quad (1.71)$$

$|\boldsymbol{V_{cb}}|$: with exclusive semileptonic decays and inclusive charm B meson becays:

$$|V_{cb}| = 0.0426 \pm 0.006. \quad (1.72)$$

$|\boldsymbol{V_{ub}}|$: value has been obtained combining measurement with exclusive method (from

$B^0 \to \rho^- \ell^+ \nu_\ell$ channel) with an inclusive method (from $b \to u\ell^- \overline{\nu}_\ell$):

$$|V_{ub}| = 0.00368 \pm 0.00009. \tag{1.73}$$

$|\boldsymbol{V_{tb}}|$: with hypotesis on unity of triangle:

$$|V_{tb}| = 0.99913 \pm 00003 \tag{1.74}$$

All the values of CKM matrix parameters founded so far, of angles and sides of unitary triangle, let us determinate an area in which we had to find the position of the third vertex. In the figure 1.5 we can see a possible triangle, where we have the area (dots on white field) in which it is possible to find vertex with a confidence level of 95%.

1.4.4 Penguin and tree processes

Direct CP violation depends both weak phases difference and strong phases difference. So, we need to distinguish which diagrams give a contribution to total amplitude with different phases. In Standard Model meson decays, composed by a heavy quark happen through charged interactions described by Lagrangian [18]. Generally, amplitudes are divided in two classes, so called *tree* and *penguin*. If all complications due to long distance strong interactions or final state interactions or hadron-hadron interactions are negligible, this split is easily explained through weak diagrams. So called penguin diagrams are ones with W boson is emitted and reabsorbed in the same line of emitter quark (figure 1.6), while tree diagram, that havo no loop in weak diagram (figura 1.7). Tree diagrams are further split in *spectator* (light quark is disconnected by starting meson in the weak diagram), *exchange* (W boson is swapped between starting meson quark) and *annihilation* (starting meson quarks are annihilated to make W).

This separation between different kinds of tree diagram is not important in CP violation cause two kinds of diagrams, that contribute to decay amplitude, have same CKM matrix element and so the same weak phase. Different from tree diagram, in $b \to q$ with $q = d, s$ process, penguin terms contribute with different combinations of CKM elements depending by the quark within loop $i = u, c, t$:

$$v_{iq} = V_{ib}^* V_{iq}. \tag{1.75}$$

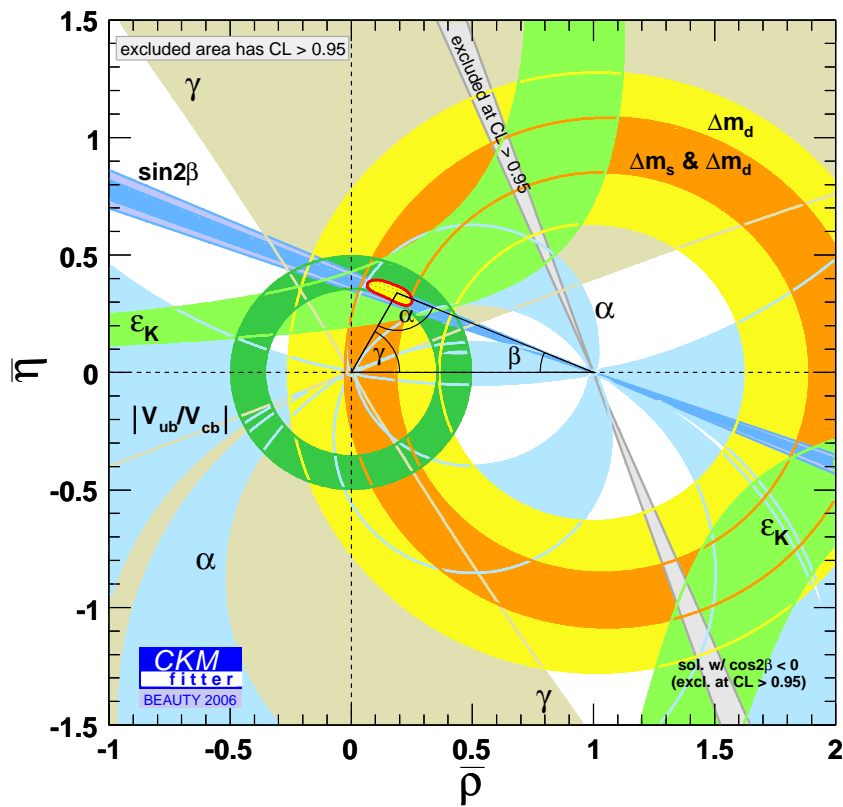Figure 1.5: Constraint from the text on the position of the apex, A, of the unitarity triangle following from $|V_{ub}|$, B mixing, ϵ and $\sin 2\beta$. A possible unitarity triangle is shown with A in the preferred region.
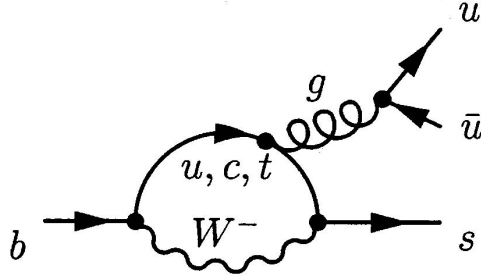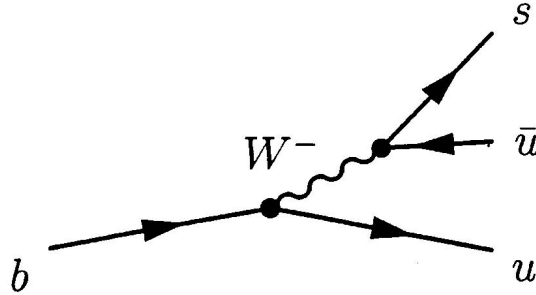
Figure 1.6: Penguin diagram for $b \to sg^*$ process.

Figure 1.7: Tree diagram for $b \to uW^-$ process.

So weak phase differences in the asymmetry are the ones due to penguin and tree contributions; it becomes important to know intensity and weak phases related to both diagrams. In penguin diagram are considered strong interactions too. The quark in the loop emits a gluon to compensate for mass difference between initial and final quark. Gluon can produce a quark-antiquark pair o be reabsorbed and re-issued from other gluons that can be found in this kind of process. When we evaluate direct *CP* asymmetry, strong phase differences are caused by penguin diagrams.

1.4.5   Measurement of angles of unitary triangle

The simplest way to see relationship between measurement of asymmetry $a_{f_{CP}}$ and angles of unitary triangle α, β e γ is due to decays dominated by only one amplitude with particular final states, *CP* eigenstates. In this case, relationship that links asymmetry

with angles is simply. In B mesons system we have, in first approximation (neglecting $\Delta\Gamma_B$):

$$\left(\frac{q}{p}\right)_B \simeq -\frac{M_{12}^*}{|M_{12}|} = \frac{(V_{tb}^*V_{td})^2}{|V_{tb}^*V_{td}|^2} = \frac{V_{tb}^*V_{td}}{V_{tb}V_{td}^*} = e^{2i\beta}. \tag{1.76}$$

Combinations of CKM parameters can be seen directly from box diagram in figure 1.3: in Standard Model they are responsible of not-diagonal elements of mass matrix defined on flavour eigenstates. Box diagrams, where mixing happens through u and c quarks, are negligible for many cases.

To avoid hadronic uncertainties, we need to choose decay modes dominated by only one diagram. Most of channels, instead, has contributions both penguin and tree diagrams. There are three cases in which CP violation is caused by phase: tree diagrams dominate penguin ones because they are forbidden; tree diagrams are forbidden and so penguin diagrams dominate; both diagrams have same weak phase.

Dominant tree diagrams

Tree diagrams are dominant when CKM parameters of penguin diagrams are not greater than tree ones, or when this condition is verified:

$$\left|\frac{V_{tb}V_{td}^*}{V_{q'b}V_{q'q}^*}\right| \leq 1 \tag{1.77}$$

An example of dominating tree diagram is $B \to \pi\pi$ decay that corresponds to $b \to u\bar{u}d$ where CKM parameters of this penguin and tree process are in the order of λ^3. So, tree diagram results dominant in a good approximation. In this case, we measure α angle and from (1.76) we obtain

$$\lambda_{\pi\pi} = \frac{q}{p}\frac{\overline{A}}{A} \simeq \frac{V_{tb}^*V_{td}}{V_{tb}V_{td}^*}\frac{V_{ub}V_{ud}^*}{V_{ub}^*V_{ud}} = e^{2i\alpha} \tag{1.78}$$

that corresponds to first equation of (1.67). Hadronic uncertainties rise from penguin diagrams contribution, estimated about 10% and it can be reduced.

Forbidden tree diagrams

In the Standard Model they expect flavour changing decays but not decaying quark charge: in this case tree diagrams are forbidden. An example of these decays is $B \to \phi K_S$ or $b \to s\bar{s}s$ at quark level. Because we have a K meson we had to consider kaons

mixing too that involves an addition of a factor

$$\left(\frac{q}{p}\right)_K \simeq \frac{V_{cs}V_{cd}^*}{V_{cs}^*V_{cd}} \tag{1.79}$$

to λ expression that becomes:

$$\lambda_{\phi K_S} = \left(\frac{q}{p}\right)_B \left(\frac{q}{p}\right)_K \frac{\overline{A}}{A} \simeq \frac{V_{tb}^*V_{td}}{V_{tb}V_{td}^*}\frac{V_{cs}V_{cd}^*}{V_{cs}^*V_{cd}}\frac{V_{tb}V_{ts}^*}{V_{tb}^*V_{ts}} = e^{-2i\beta} \tag{1.80}$$

Diagram with only one weak phase

$B \to \psi K_S$ decay, $b \to c\overline{c}s$, is representative in the case which a single weak phase dominates. Neglecting corrections in the order of λ^4 we have $V_{tb}^*V_{ts} = -V_{cb}V_{cs}^*$, where first CKM elements combination is related to penguin diagram while second one is related to tree diagram. In this way, with a good approximation, we can assume same phase for both diagrams.

$$\lambda_{\psi K_S} = \left(\frac{q}{p}\right)_B \left(\frac{q}{p}\right)_K \frac{\overline{A}}{A} \simeq \frac{V_{tb}^*V_{td}}{V_{tb}V_{td}^*}\frac{V_{cs}V_{cd}^*}{V_{cs}^*V_{cd}}\frac{V_{cb}V_{cs}^*}{V_{cb}^*V_{cs}} = -e^{-2i\beta} \tag{1.81}$$

Hadronic uncertainties are estimated about 10^{-3}.

1.5 Rare B meson decays

All B meson decays that not happen through $b \to c$ reaction are known as rare B decays. Due to little value of $|V_{ub}|$, $b \to u$ are suppressed, so, we expect observable contributions from other diagrams for some hadronic decay channel.

There are many processes that contribute to rare B decays. B mesons can decay with or without strangeness change. ($|\Delta S| = 1$ or 0). Rare decays with $|\Delta S| = 1$ produce, in their final state, strange mesons (K or K^*), and they happen through a process with a Cabibbo-suppressed spectator quark $b \to u\overline{u}s$ and a gluonic loop (penguin) $b \to sg^*$. In these decays penguin diagrams are dominant. In these diagrams the favourite side from CKM matrix, that corresponds to $b \to s$ transition, should be rare decays amplitude in final states with one or three s quarks.

Viceversa, for decays with $|\Delta S| = 0$, we expect a dominant Cabibbo-favoured spectator quark process $b \to u\overline{u}d$, because $b \to dg^*$ is suppressed by V_{td}, but it

shouldn't be negligible for decays in final states without s or c quarks. A significant contribution of $b \to dg^*$ would mean presence of so called *penguin pollution*. We can note loop diagram is more significative for B meson decays rather than D decays because $b \to s$ loop is sensitive for strong coupling of t quark through V_{tb} and V_{ts}, while corresponding $c \to u$ loop contributions are suppressed cause of weak V_{cb} and V_{ub} coupling and due to small s and d masses [19].

1.6 Formalism for $B\overline{B}$ coherent states

B^0 and $\overline{B}^0$ mesons produced by $\Upsilon(4\text{S})$ decay can be found in a coherent quantum state with $L = 1$ (*p wave*). In this state two particle form one system that can be considered as one B meson evolving in time with two mesons propagating in the space with the same phase between them. This means that for every time the state is composed exactly by B^0 and $\overline{B}^0$. When one of two particles decays, we will be able to have events with B^0 and $\overline{B}^0$ whose decay probabilities are controlled by time difference of two decays.

Two mesons produced in $\Upsilon(4\text{S})$ decay are identified with θ angle that form with electron beam in Υ frame. Coherent state is described by antisymmetric function:

$$
\begin{aligned}
S(\tau_1, \tau_2) \quad &= \tfrac{1}{\sqrt{2}}\{B^0_{phys}(\tau_1, \theta, \phi)\overline{B}^0_{phys}(\tau_2, \pi - \theta, \phi + \pi) \\
&\quad - \overline{B}^0_{phys}(\tau_1, \theta, \phi)B^0_{phys}(\tau_2, \pi - \theta, \phi + \theta)\}\sin(\theta)
\end{aligned}
\tag{1.82}
$$

and replacing 1.37 and 1.38, we can write as

$$
\begin{aligned}
S(\tau_1, \tau_2) \quad &= \tfrac{1}{\sqrt{2}}e^{-(\Gamma/2 + im)(\tau_1 + \tau_2)}\{\cos[\Delta m_B(\tau_1 - \tau_2)/2](B^0_1\overline{B}^0_2 - \overline{B}^0_1 B^0_2) \\
&\quad - i\sin[\Delta m_B(\tau_1 - \tau_2)/2](\tfrac{p}{q}B^0_1 B^0_2 - \tfrac{q}{p}\overline{B}^0_1\overline{B}^0_2)\}\sin(\theta_1).
\end{aligned}
\tag{1.83}
$$

where τ_1 is B_1 own time, which we identify with B meson decaying forward ($\theta_1 < \pi/2$), and τ_2 is B_2 own time moving in the opposite direction. Cause in Υ frame two B mesons have same but opposite momenta, we can consider, until one of two meson will decay, $\tau_1 = \tau_2$ and in this case the equation (1.83) contains B^0 and $\overline{B}^0$. When one of the two particles decays, its own timer stops, so proportional terms $\sin[\Delta m_B(\tau_1 - \tau_2)/2]$ assume importance.

From equation (1.83) it's possible the following result: decays amplitude in which

one of two mesons decays in a final state f_1 at t_1 time while the other one decays in a state f_2 at t_2 time is obtained in this way

$$
\begin{aligned}
A(t_1, t_2) \;=\;& \tfrac{1}{\sqrt{2}} e^{-(\Gamma/2+im)(t_1+t_2)}\zeta(t_1,t_2)\{cos[\Delta m_B(t_1-t_2)/2](A_1\overline{A}_2 - \overline{A}_1 A_2) \\
& -i\sin[\Delta m_B(t_1-t_2)/2](\tfrac{p}{q}A_1 A_2 - \tfrac{q}{p}\overline{A}_1\overline{A}_2)\}\sin(\theta_1), \qquad (1.84)
\end{aligned}
$$

where A_i means B^0 decay amplitude in a f_i state, $\overline{A}_i$ is $\overline{B}^0$ decay amplitude in the same state f_i.

A particular B decay state that allows us to identify such flavour meson (*tagging decays*) has one of two amplitudes A_f or $\overline{A}_f$ equal to zero. In the equation (1.84) we introduce following brief notation to mantain same signs with (1.83)

$$
\zeta(t_1, t_2) = \begin{cases} +1 & t_1 = \tau_1,\ t_2 = \tau_2 \\ -1 & t_1 = \tau_2,\ t_2 = \tau_1 \end{cases}
$$

but this factor vanishes in decay rate calculation.

We can evaluate production rate of combined states f_1 and f_2, that results time dependent:

$$
\begin{aligned}
R(t_1, t_2) =\;& N e^{-\Gamma(t_1+t_2)}\{(|A_1|^2 + |\overline{A}_1|^2)(|A_2|^2 + |\overline{A}_2|^2) - 4\mathrm{Re}(\tfrac{q}{p}A_1^*\overline{A}_1)\mathrm{Re}(\tfrac{q}{p}A_2^*\overline{A}_2) \\
& -\cos(\Delta m_B(t_1-t_2))[(|A_1|^2 - |\overline{A}_1|^2)(|A_2|^2 - |\overline{A}_2|^2) + 4\mathrm{Im}(\tfrac{q}{p}A_1^*\overline{A}_1)\mathrm{Im}(\tfrac{q}{p}A_2^*\overline{A}_2)] \\
& +2\sin(\Delta m_B(t_1-t_2))[\mathrm{Im}(\tfrac{q}{p}A_1^*\overline{A}_1)(|A_2|^2 - |\overline{A}_2|^2) - (|A_1|^2 - |\overline{A}_1|^2)\mathrm{Im}(\tfrac{q}{p}A_2^*\overline{A}_2)]\}
\end{aligned}
$$
$$(1.85)$$

In this formula, it was estimated an integral on all possible directions of both B mesons so we could delete angular dependence and showing a normalization factor N. We used also this approximation $|q/p| = 1$.

To measure CP asymmetry we seek for events in which a B (B_{CP}) decays in a CP eigenstate f_{CP} at $t_{f_{CP}}$ time, while other meson (B_{tag}) decays in a way that allows us to identify its flavour, so called *tagging* mode, at t_{tag} time. For example, it's possible to consider a way to tag with $A_2 = 0$, $\overline{A}_2 = \overline{A}_{\mathrm{tag}}$. This identifies B meson decaying in a CP eigenstate as a B^0 at $t_1 = t_{\mathrm{tag}}$ time in with the tagging decays. Furthermore we had to underline how this it is true when tagging decay happens afterwards the decay in CP eigenstate. In this case, B_{CP}, for every time $t_1 < t_{\mathrm{tag}}$, is described by a state evolving in a way to be tagged as B^0 at $t_1 = t_{\mathrm{tag}}$ time. So, the expression with two

times it is reduced to

$$
\begin{aligned}
R(t_{\text{tag}}, t_{f_{CP}}) = N e^{-\Gamma(t_{\text{tag}} + t_{f_{CP}})} |\overline{A}_{\text{tag}}|^2 |A_{f_{CP}}|^2 \{ & 1 + |\lambda_{f_{CP}}|^2 \\
& + \cos[\Delta m_B(t_{f_{CP}} - t_{\text{tag}})](1 - |\lambda_{f_{CP}}|^2) \\
& - 2\sin[\Delta m_B(t_{f_{CP}} - t_{\text{tag}})]\text{Im}(\lambda_{f_{CP}}) \}
\end{aligned} \tag{1.86}
$$

with $\lambda_{f_{CP}}$ defined in 1.52.

If final tagging state has $\overline{A}_2 = 0$, $A_2 = A_{\text{tag}}$, that identifies B_{CP} as a $\overline{B}^0$ at t_{tag} time, usually it is used an expression similar to equation (1.86) where signs of cosinus and sinus terms are opposite. Hypotesis $|q/p| = 1$ guarantees us amplitudes for opposite tags are same. With these rates, we can evaluate time dependent CP asymmetry that results to be equal to expression 1.56, where $t = t_{f_{CP}} - t_{\text{tag}}$.

Expression (1.86) is function of two temporal variables t_{tag} and $t_{f_{CP}}$ representing respectively passed time from $B^0\overline{B}^0$ pair creation for B_{CP} and B_{tag}. This requires reconstruction of pair creation time but it's pratically impossible to realize it. So to solve this problem, we replace variables

$$
\{t_{\text{tag}}, t_{f_{CP}}\} \rightarrow \{s = t_{\text{tag}} + t_{f_{CP}}, \Delta t = t_{f_{CP}} - t_{\text{tag}}\}
$$

with these new ones, assuming values:

$$
\begin{aligned}
-\infty &< \Delta t < +\infty \\
|\Delta t| &< s < +\infty
\end{aligned} \tag{1.87}
$$

Integrating on s, we obtain relationship between decay rate and $B_{CP} \rightarrow f_{CP}$ to Δt:

$$
R(\Delta t) \propto e^{-\Gamma|\Delta t|}[1 \pm S \sin(\Delta m_B \Delta t) \mp C \cos(\Delta m_B \Delta t)] \tag{1.88}
$$

where C and S are defined, respectively, in 1.55 and signum $+ (-)$ refers to B_{tag} when we have B^0 ($\overline{B}^0$). Necessity of the Δt measurement is main cause of contruction of asymmetric collider (please see Chapter 2 for more details).

1.7   Weak phase α

We will describe below the experimental constraints on the Unitary Triangle angle α obtained from B-meson decays involving $b \to u$ transitions. The CKM angle is well known and consistent with SM predictions [24]. Any constraint on α consitutes a test of the SM description of quark mixing and CPV in B-meson decays. A significant deviation from SM expectation would be a clear indication of new physics. It is possible to obtain a SM prediction of α from indirect constraints by combining measurements of the CKM matrix elements $|V_{us}|$, $|V_{ud}|$, $|V_{ub}|$ and $|V_{cb}|$, CPV in mixing from neutral kaons, $B - \overline{B}$ mixing in B_d and B_s mesons and the measurement of $\sin2\beta$ from $b \to c\overline{c}s$ decays. The SM predictions for α are $(98.2 \pm 7.7)^{\circ}$ [25] and $(97^{+13}_{-19})^{\circ}$ [26]. The α angle of the Unitary Triangle has been measured from the time-dependent CP asymmetries in the decays $B^0 \to \pi^+\pi^-$, $B^0 \to \rho^{\pm}\pi^{\mp}$, and $B^0 \to \rho^+\rho^-$. Combined error is at a level of 9° [27]. The amplitudes of the target processes expected in the Standard Model represent the sum of tree and penguin amplitudes with different weak and strong phases. The corresponding Feynman diagrams for the decay $B^0 \to a_1^{\pm}\pi^{\mp}$ are depicted in Fig. 1.8.
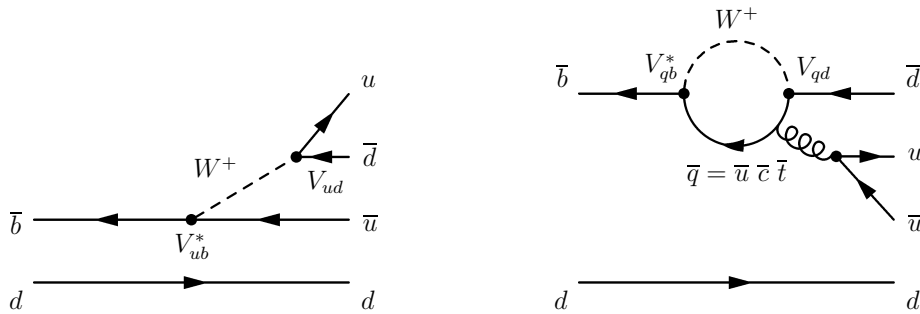

Figure 1.8: *Tree (left) and penguin (right) diagrams for the decay $B^0 \to a_1^{\pm}\pi^{\mp}$.*

The extracted α_{eff} differs from α because of the presence of penguin amplitudes. In order to determine an upper bound to this difference, SU(3) flavor symmetry can be used. This approach needs to measure BFs (or UL at 90% CL) for the SU(3) partners of the main mode (see section 1.7.2).

1.7.1   Time Dependent Decay Rates in $B^0 \to a_1^{\pm}(1260)\,\pi^{\mp}$

The time-dependent (TD) CP violating asymmetries can be measured also in B^0 decays to non CP eigenstate like $B^0 \to a_1^{\pm}(1260)\,\pi^{\mp}$. [10, 30]. Such possibility was

already investigated in the BaBar Book [31]. The formalism of TD CP analysis is the same of the decay $B^0 \to \rho^\pm \pi^\mp$ and can be seen in [32]. We report here the main formulas and observables for $B^0 \to a_1^\pm(1260)\, h^\mp$ with h=π or K. With $\Delta t \equiv t_{a_1h} - t_{\text{tag}}$ defined as the proper time interval between the decay of the reconstructed $B^0_{a_1h}$ and that of the other meson B^0_{tag}, the time-dependent decay rates are given by [33]:

$$
\begin{aligned}
f^{a_1^+ h^-}_{B^0 \text{tag}} &= (1 + \mathcal{A}^{a_1h}_{CP}) \frac{e^{-|\Delta t|/\tau}}{4\tau} \Big[1 + \frac{\Delta D_{c_{\text{tag}}}}{2} + \langle D \rangle_{c_{\text{tag}}} \Big(S^+_{a_1h} \sin(\Delta m_d \Delta t) - \\
& \qquad\qquad\qquad\qquad\qquad\qquad\qquad\qquad C^+_{a_1h} \cos(\Delta m_d \Delta t) \Big) \Big] \\[2mm]
f^{a_1^+ h^-}_{\overline{B}^0 \text{tag}} &= (1 + \mathcal{A}^{a_1h}_{CP}) \frac{e^{-|\Delta t|/\tau}}{4\tau} \Big[1 - \frac{\Delta D_{c_{\text{tag}}}}{2} - \langle D \rangle_{c_{\text{tag}}} \Big(S^+_{a_1h} \sin(\Delta m_d \Delta t) - \\
& \qquad\qquad\qquad\qquad\qquad\qquad\qquad\qquad C^+_{a_1h} \cos(\Delta m_d \Delta t) \Big) \Big] \\[2mm]
f^{a_1^- h^+}_{B^0 \text{tag}} &= (1 - \mathcal{A}^{a_1h}_{CP}) \frac{e^{-|\Delta t|/\tau}}{4\tau} \Big[1 + \frac{\Delta D_{c_{\text{tag}}}}{2} + \langle D \rangle_{c_{\text{tag}}} \Big(S^-_{a_1h} \sin(\Delta m_d \Delta t) - \\
& \qquad\qquad\qquad\qquad\qquad\qquad\qquad\qquad C^-_{a_1h} \cos(\Delta m_d \Delta t) \Big) \Big] \\[2mm]
f^{a_1^- h^+}_{\overline{B}^0 \text{tag}} &= (1 - \mathcal{A}^{a_1h}_{CP}) \frac{e^{-|\Delta t|/\tau}}{4\tau} \Big[1 - \frac{\Delta D_{c_{\text{tag}}}}{2} - \langle D \rangle_{c_{\text{tag}}} \Big(S^-_{a_1h} \sin(\Delta m_d \Delta t) - \\
& \qquad\qquad\qquad\qquad\qquad\qquad\qquad\qquad C^-_{a_1h} \cos(\Delta m_d \Delta t) \Big) \Big]
\end{aligned}
\tag{1.89}
$$

where $\langle D \rangle_{c_{\text{tag}}}$ and $\Delta D_{c_{\text{tag}}}$ are the average dilution factor and the tag-asymmetry dilution term of the tagging category c_{tag}, respectively, $\mathcal{A}^{a_1h}_{CP}$ is the time-integrated charge asymmetry, τ is the mean B^0 lifetime, and Δm_d is the $B^0 \overline{B}^0$ oscillation frequency. The time-dependent parameters $C^+_{a_1\pi}$, $C^-_{a_1\pi}$, $S^+_{a_1\pi}$, and $S^-_{a_1\pi}$ must be measured. In the case of the self-tagging mode $a_1 K$, the values of these parameters are:

$$
C^+_{a_1 K} = -1\,, \qquad C^-_{a_1 K} = 1\,, \qquad S^+_{a_1 K} = 0\,, \qquad S^-_{a_1 K} = 0\,. \tag{1.90}
$$

To semplify the notation and to provide an immediate interpretation in terms of CP violation, we write the decay rates in eq. 1.89 using the avarage parameters:

$$
C_{a_1h} = \frac{C^+_{a_1h} + C^-_{a_1h}}{2}\,, \quad \Delta C_{a_1h} = \frac{C^+_{a_1h} - C^-_{a_1h}}{2}\,, \tag{1.91}
$$

$$S_{a_1h} = \frac{S^+_{a_1h} + S^-_{a_1h}}{2} \ , \ \Delta S_{a_1h} = \frac{S^+_{a_1h} - S^-_{a_1h}}{2} \ . \tag{1.92}$$

The decay rates in terms of these avarage parameters are :

$$
\begin{aligned}
f^{a_1^+h^-}_{B^0\text{tag}} &= (1 + \mathcal{A}^{a_1h}_{CP})\frac{e^{-|\Delta t\,|/\tau}}{4\tau}\Big[1 + (S_{a_1h} + \Delta S_{a_1h})\sin(\Delta m_d\Delta t\,) - \\
&\qquad\qquad\qquad\qquad\qquad (C_{a_1h} + \Delta C_{a_1h})\cos(\Delta m_d\Delta t\,)\Big] \\[2mm]
f^{a_1^+h^-}_{\overline{B}^{\,0}\text{tag}} &= (1 + \mathcal{A}^{a_1h}_{CP})\frac{e^{-|\Delta t\,|/\tau}}{4\tau}\Big[1 - (S_{a_1h} + \Delta S_{a_1h})\sin(\Delta m_d\Delta t\,) + \\
&\qquad\qquad\qquad\qquad\qquad (C_{a_1h} + \Delta C_{a_1h})\cos(\Delta m_d\Delta t\,)\Big] \\[2mm]
f^{a_1^-h^+}_{B^0\text{tag}} &= (1 - \mathcal{A}^{a_1h}_{CP})\frac{e^{-|\Delta t\,|/\tau}}{4\tau}\Big[1 + (S_{a_1h} - \Delta S_{a_1h})\sin(\Delta m_d\Delta t\,) - \\
&\qquad\qquad\qquad\qquad\qquad (C_{a_1h} - \Delta C_{a_1h})\cos(\Delta m_d\Delta t\,)\Big] \\[2mm]
f^{a_1^-h^+}_{\overline{B}^{\,0}\text{tag}} &= (1 - \mathcal{A}^{a_1h}_{CP})\frac{e^{-|\Delta t\,|/\tau}}{4\tau}\Big[1 - (S_{a_1h} - \Delta S_{a_1h})\sin(\Delta m_d\Delta t\,) + \\
&\qquad\qquad\qquad\qquad\qquad (C_{a_1h} - \Delta C_{a_1h})\cos(\Delta m_d\Delta t\,)\Big]
\end{aligned}
\tag{1.93}
$$

The time- and flavor-integrated charge asymmetries $\mathcal{A}^{a_1\pi}_{CP}$ and $\mathcal{A}^{a_1K}_{CP}$ measure direct CP violation. The "dilution" parameters ΔC_{a_1h} and ΔS_{a_1h} are insensitive to CP violation. The parameter ΔC_{a_1h} measures the asymmetry between the sum of the probabilities $\mathrm{Pr}(B^0_{a_1h} \to a_1^+h^-) + \mathrm{Pr}(\overline{B}^{\,0}_{a_1h} \to a_1^-h^+)$ and $\mathrm{Pr}(B^0_{a_1h} \to a_1^-h^+) + \mathrm{Pr}(\overline{B}^{\,0}_{a_1h} \to a_1^+h^-)$: the larger $|\Delta C_{a_1h}|$, the weaker the sensitivity on S_{a_1h}. A value of $\Delta C_{a_1h} = 1(-1)$ would imply that $B^0(\overline{B}^{\,0}) \to a_1^+h^-$ is self-tagging. ΔS_{a_1h} is related to the strong phase difference between the amplitudes contributing to $B^0 \to a_1h$ decays. The quantities S_{a_1h} and C_{a_1h} parameterize mixing-induced CP violation related to the angle α, and flavor-dependent direct CP violation, respectively. For the self-tagging a_1K mode, the values of the four time-dependent parameters are $C_{a_1K} = 0$, $\Delta C_{a_1K} = -1$, $S_{a_1K} = 0$, and $\Delta S_{a_1K} = 0$. It is needed to measure the six parameters $\mathcal{A}^{a_1\pi}_{CP}$, $\mathcal{A}^{a_1K}_{CP}$, $S_{a_1\pi}$, $C_{a_1\pi}$, $\Delta S_{a_1\pi}$, and $\Delta C_{a_1\pi}$. Particularly interesting are the two direct CP asymmetries between $B^0\ (\overline{B}^{\,0}\ ) \to a_1^+\pi^-$ and $\overline{B}^{\,0}\ (B^0\ ) \to a_1^-\pi^-$ [32, 36] . These

asymmetries may be expressed in terms of the observables $C_{a_1\pi}$, $\Delta C_{a_1\pi}$, and $\mathcal{A}_{CP}^{a_1\pi}$:

$$\mathcal{A}_{CP}^{+-} = \frac{\mathcal{A}_{CP}^{a_1\pi}(1 + \Delta C_{a_1\pi}) + C_{a_1\pi}}{1 + \mathcal{A}_{CP}^{a_1\pi} C_{a_1\pi} + \Delta C_{a_1\pi}}, \qquad \mathcal{A}_{CP}^{-+} = \frac{\mathcal{A}_{CP}^{a_1\pi}(1 - \Delta C_{a_1\pi}) - C_{a_1\pi}}{1 - \mathcal{A}_{CP}^{a_1\pi} C_{a_1\pi} - \Delta C_{a_1\pi}} . \quad (1.94)$$

1.7.2   SU(3) Bounds on α - α_{eff}

Phases $\alpha_{\text{eff}}^{\pm}$ may be defined [37, 38, 39] as :

$$\alpha_{\text{eff}}^{\pm} \equiv \frac{1}{2} \arg[(q/p)(\overline{A}_{a_1\pi}^{\pm}/A_{a_1\pi}^{\mp})],$$

where $\arg[q/p]$ is the $B^0\overline{B}^0$ mixing phase, and $A_{a_1\pi}^{+}(\overline{A}_{a_1\pi}^{+})$ and $A_{a_1\pi}^{-}(\overline{A}_{a_1\pi}^{-})$ are the transition amplitudes of the processes $B^0(\overline{B}^0) \rightarrow a_1^+\pi^-$ and $B^0(\overline{B}^0) \rightarrow a_1^-\pi^+$, respectively. These phases cannot be measured separately while their algebraic average is measurable [33]:

$$\alpha_{\text{eff}} \equiv \frac{1}{2}\left(\alpha_{\text{eff}}^{+} + \alpha_{\text{eff}}^{-}\right) \qquad (1.95)$$

$$\alpha_{\text{eff}} = \frac{1}{4}\left[\arcsin\left(\frac{S_{a_1\pi} + \Delta S_{a_1\pi}}{\sqrt{1 - (C_{a_1\pi} + \Delta C_{a_1\pi})^2}}\right) + \arcsin\left(\frac{S_{a_1\pi} - \Delta S_{a_1\pi}}{\sqrt{1 - (C_{a_1\pi} - \Delta C_{a_1\pi})^2}}\right)\right]$$
$$(1.96)$$

The angles $\alpha_{\text{eff}}^{\pm}$ (and α_{eff}) are equal to α in the absence of contributions from penguin amplitudes. The difference α_{eff} - α may be bounded, using SU(3) relations. Let's consider first the upper bounds on $|\alpha - \alpha_{\text{eff}}^{-}|$, using the decay modes $B^0 \rightarrow a_1^- K^+$ and $B^+ \rightarrow a_1^+ K^0$. Defining the charge averaged decay rate $\overline{\Gamma}(B \rightarrow f) \equiv \frac{1}{2}\left[\Gamma(B \rightarrow f) + \Gamma(\overline{B} \rightarrow \overline{f})\right]$, we may define also the ratios:

$$\mathcal{R}_-^+ \equiv \frac{\overline{\lambda}^2 f_\pi^2 \overline{\Gamma}(a_1^+ K^0)}{f_K^2 \overline{\Gamma}(a_1^-\pi^+)}, \qquad \mathcal{R}_-^0 \equiv \frac{\overline{\lambda}^2 f_\pi^2 \overline{\Gamma}(a_1^- K^+)}{f_K^2 \overline{\Gamma}(a_1^-\pi^+)}, \qquad (1.97)$$

where $\overline{\lambda} = 0.23$ and f_π, f_K are decay constants [40]. Superscripts denote the charge of the B meson while the subscripts denote the charge of a_1 meson in the denominator. Defining the ratio of penguin (p_-) and tree (t_-) amplitudes in the processes $B^0 \rightarrow a_1^-\pi^+$ and $\overline{B}^0 \rightarrow a_1^+\pi^-$:

$$r_- = \frac{|p_-|}{|t_-|},$$

we have the following bounds [30]:

$$\frac{\mathcal{R}_-^+}{1+\sqrt{\mathcal{R}_-^+}} \leq r_- \leq \frac{\mathcal{R}_-^+}{1+\sqrt{\mathcal{R}_-^+}}, \tag{1.98}$$

$$\frac{\sqrt{\mathcal{R}_-^0}-\overline{\lambda}^2}{1+\sqrt{\mathcal{R}_-^0}} \leq r_- \leq \frac{\sqrt{\mathcal{R}_-^0}-\overline{\lambda}^2}{1-\sqrt{\mathcal{R}_-^0}}, \tag{1.99}$$

and the bounds :

$$|\sin(\alpha-\alpha_{\text{eff}}^-)| \leq \sqrt{\mathcal{R}_-^0}, \tag{1.100}$$

$$|\sin(\alpha-\alpha_{\text{eff}}^-)| \leq \sqrt{\mathcal{R}_-^+}\sin\gamma, \tag{1.101}$$

where γ is one of the angles of the Unitary Triangle. The current constraints on γ [42] are : $38^0 \leq \gamma \leq 80^0$ (at 95% C.L.). Let's consider now the upper bounds on $|\alpha-\alpha_{\text{eff}}^+|$, using the decay modes $B^+ \rightarrow K_{1A}^0\pi^+$ and $B^0 \rightarrow K_{1A}^+\pi^-$, where K_{1A} is the strange member, partner of a_1 in the axial-vector nonet 1^{++}. We may define in this case the ratios:

$$\mathcal{R}_{+A}^+ \equiv \frac{\overline{\lambda}^2 f_{a_1}^2 \overline{\Gamma}(K_{1A}^0\pi^+)}{f_{K_{1A}}^2 \overline{\Gamma}(a_1^+\pi^-)}, \qquad \mathcal{R}_{+A}^0 \equiv \frac{\overline{\lambda}^2 f_{a_1}^2 \overline{\Gamma}(K_{1A}^+\pi^-)}{f_{K_{1A}}^2 \overline{\Gamma}(a_1^+\pi^-)}, \tag{1.102}$$

K_{1A} is a superposition of the physical states $K_1(1270)$ and $K_1(1400)$:

$$K_{1A} = \cos\theta K_1(1400) + \sin\theta K_1(1270),$$

with $33^0 \leq \theta \leq 57^0$ [43]. This implies for the amplitudes:

$$A(B^+ \rightarrow K_{1A}^0\pi^+) = \cos\theta A(K_1^0(1400)\pi^+) + \sin\theta A(K_1^0(1270)\pi^+)$$

and

$$A(B^0 \rightarrow K_{1A}^+\pi^-) = \cos\theta A(K_1^+(1400)\pi^-) + \sin\theta A(K_1^+(1270)\pi^-)$$

and upper bounds for charge averages rates:

$$\overline{\Gamma}(K_{1A}^0\pi^+) \leq \left[\cos\theta\sqrt{\overline{\Gamma}(K_1^0(1400)\pi^+)} + \sin\theta\sqrt{\overline{\Gamma}(K_1^0(1270)\pi^+)}\right]^2 \tag{1.103}$$

$$\overline{\Gamma}(K_{1A}^{+}\pi^{-}) \leq \left[\cos\theta\sqrt{\overline{\Gamma}(K_1^{+}(1400)\pi^{-})} + \sin\theta\sqrt{\overline{\Gamma}(K_1^{+}(1270)\pi^{-})}\right]^2 \qquad (1.104)$$

These bounds can be used in eq. 1.102 and obtain the upper bounds :

$$|\sin(\alpha - \alpha_{\text{eff}}^{+}| \leq \sqrt{\mathcal{R}_{+A}^0}\,, \qquad (1.105)$$

$$|\sin(\alpha - \alpha_{\text{eff}}^{+}| \leq \sqrt{\mathcal{R}_{+A}^{+}}\sin\gamma\,, \qquad (1.106)$$

Note that the upper bounds in eq. 1.100, 1.101 and 1.105, 1.106 calculated using ratios of charge averaged rates can be calculated using (if possible) separate rates for B and $\overline{B}$ mesons. The separate upper bounds on $|\alpha - \alpha_{\text{eff}}^{-}|$ and $|\alpha - \alpha_{\text{eff}}^{+}|$ may be combined and obtain an upper bound on $|\alpha - \alpha_{\text{eff}}|$:

$$|\alpha - \alpha_{\text{eff}}| \leq \frac{1}{2}\left(|\alpha - \alpha_{\text{eff}}^{-}| + |\alpha - \alpha_{\text{eff}}^{+}|\right) \qquad (1.107)$$

Equations 1.98 and 1.99 can be used to check the validity of the approximation that penguin contribution is a small effect. It shouldbe necessary eventually to test flavor SU(3) and SU(3) breaking corrections.

1.8   Latest results on CP violation measurements

BABAR has already published the results on the measurement of time-dependent CP-violating asymmetries in the neutral B mesons decays. The results was obtained using analyzed data corresponding to 232 millions $B\overline{B}$ pairs acquired in the period 1999-2004. The selected events are the ones with a neutral B completely reconstructed in a charmonium final state, while the flavour of the other B is determined through decay products. Asymmetry amplitude, proportional to $\sin 2\beta$ in the considered decays, comes from lifetime distributions of these events. The result obtained is:

$$\sin 2\beta = 0.722 \pm 0.040_{stat} \pm 0.023_{syst}$$

It has been also determined $|\lambda|$ value:

$$|\lambda| = 0.950 \pm 0.031_{stat} \pm 0.013_{syst}$$

consistent with the absence of direct CP violation, according with the Standard Model results for these decay modes. Furthermore *BABAR* for the first time has measured the direct CP asymmetry in the decay $B^0 \rightarrow K^+\pi^-$ [70] with the following result:

$$A_{K\pi} = -0.133 \pm 0.030_{stat} \pm 0.009_{syst}$$

Also Belle collaboration at KEKB (Tsukuba, Japan) has published measurements on CP violation, obtained with a statystics of 152 millions $B\overline{B}$ pairs:

$$\sin 2\beta = 0.728 \pm 0.056_{stat} \pm 0.023_{syst}$$

$$|\lambda| = 1.007 \pm 0.041_{stat} \pm 0.033_{syst}$$

The results founded by *BABAR* and Belle are in a good agreement with the Standard Model prediction.

Chapter 2

The BaBar Detector

2.1   Overview — B-Factories

Exploring CP violation in the B system and its potential impact on the Standard Model, baryogenesis, and cosmology, requires copious production of B mesons, accurate measurement of the B flight time and flavor, and reasonably low background for reconstruction. There are several potential options for experiments which can fulfill these criteria:

1. Hadron colliders ($\overset{(-)}{pp}$): The cross section for $B\overline{B}$ production at TeV hadron colliders is very high compared with e^+e^- B factories, approximately $100\,\mu$b vs. 1.2 nb. This large advantage does compete with several disadvantages, however. Hadronic collisions have far more background, making reconstruction of final states which do not contain a J/ψ very challenging. Purely hadronic final states with non-negligible background in e^+e^- colliders at the $\Upsilon(4S)$, such as $D\overline{D}$ or $\pi^0\pi^0$, may be extremely difficult at a hadronic collider and it is not clear that it will be possible to reconstruct such decays. Nevertheless, these experiments do have a statistical advantage and also have the potential for observing CP violation in the B_s system, which is beyond the reach of $\Upsilon(4S)$ experiments. LHC-b at CERN is a new experiment currently under construction.

2. Fixed target proton beam experiments: Fixed-target experiments also offer the potential of a higher rate of B production, but have even greater levels of backgrounds, superimposed interactions, and boost which compresses all tracks in a small solid angle. A significant effort was undertaken at DESY to build such an

experiment, HERA-B.

3. e^+e^- colliders at the Z-pole: The Z-pole presents a relatively clean environment for B-physics with a relatively large cross section ($\sim$ 6 nb). However, the luminosities achieved at this energy are low, the only two colliders in the world which can reach it, LEP and SLD, are both dismantled, and the cost of building new experiments at this energy prevents this from being a viable option.

4. Symmetric and asymmetric e^+e^- B-factories: The $\Upsilon(4S)$ resonance provides a very clean environment for B reconstruction. Asymmetric e^+ and e^- beams provide a boost to the B meson pair that is produced, allowing for reconstruction of B flavor as a function of flight time through the separation of the B vertices in the lab frame, Δz . Statistical limitations, of which luminosity is the critical factor, are the dominant source of error for time-dependent CP asymmetries. Two asymmetric B-factories have been built and are currently producing physics: PEP-II/*BABAR* and KEK-B/Belle. Previously, the symmetric B-factory CLEO (at the CESR ring at Cornell) was able to produce precision B physics results, however the symmetric design precluded measurement of time-dependent CP-violating asymmetries.

Figures 2.2 and 2.3 show the *BABAR* and Belle detectors. The experiments are very similar, with the following important differences: the KEK B factory has a nonzero beam crossing angle (4.2 mr) at the interaction point (IP), whereas the PEP-II/*BABAR* B factory has a more traditional collinear IP. The KEK design potentially allows a greater number of beam bunches to be stored in the ring, due to absence of parasitic crossings at $\pm$ 1m, as are present in the PEP-II design. However KEK-B is a highly non-traditional design; concerns over higher-order mode resonances at the IP led the PEP-II B factory to use a collinear crossing. So far, both KEK-B and PEP-II have performed well. At the time of writing, PEP-II has integrated 254.6 fb^{-1}and KEK-B has integrated 443.2 fb^{-1}.
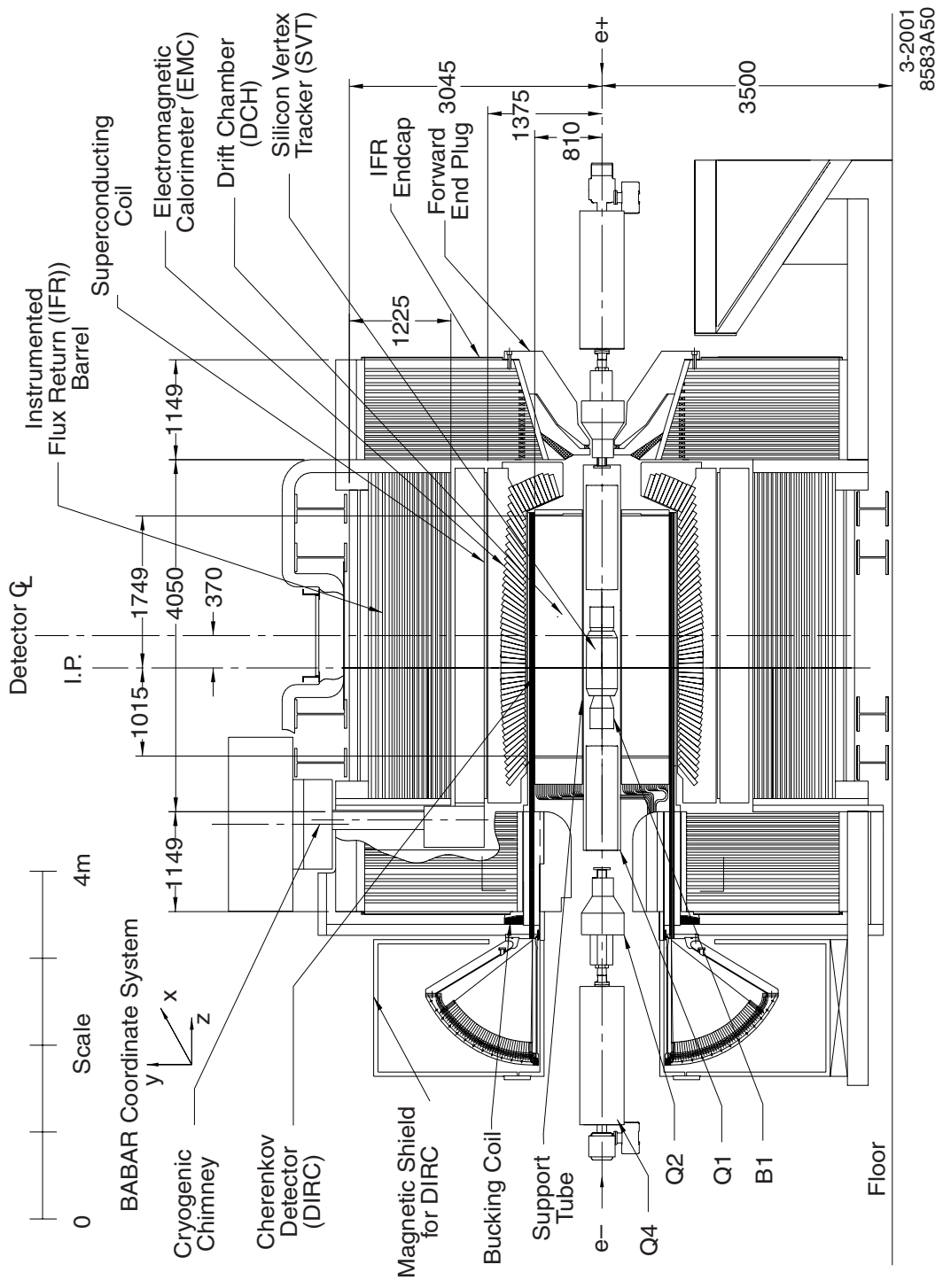
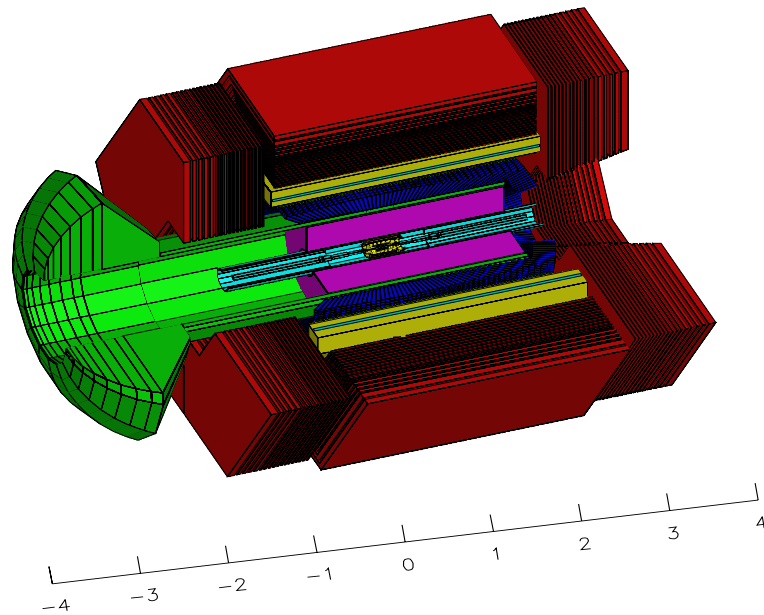Figure 2.1: *BABAR* detector longitudinal section.
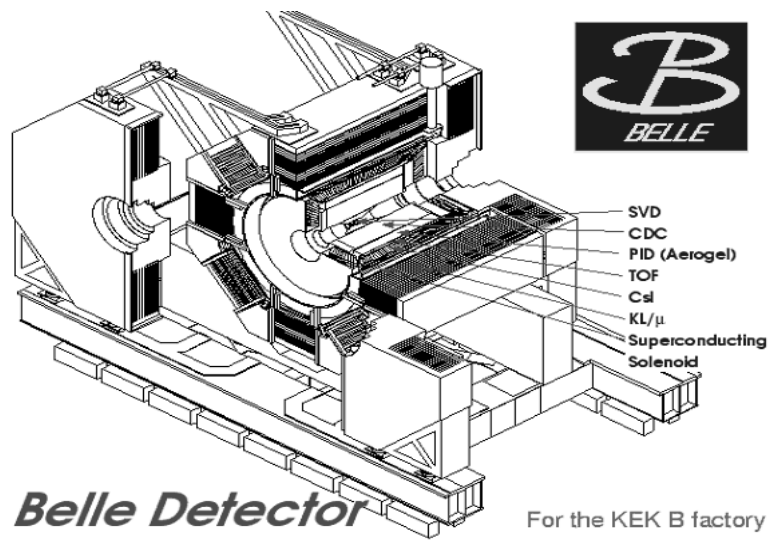
Figure 2.2: *BABAR* detector cutout diagram.

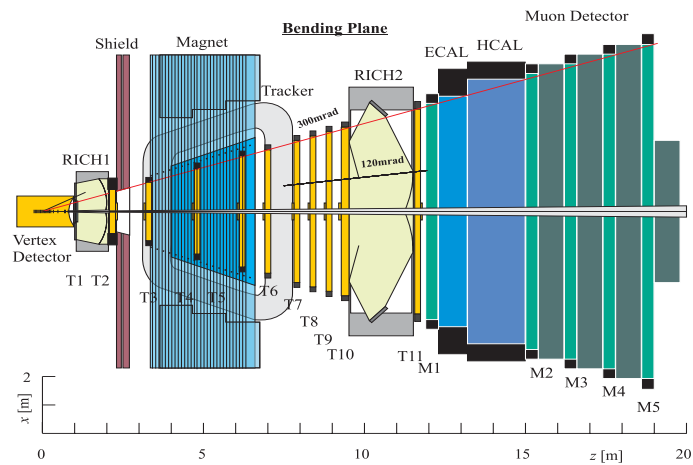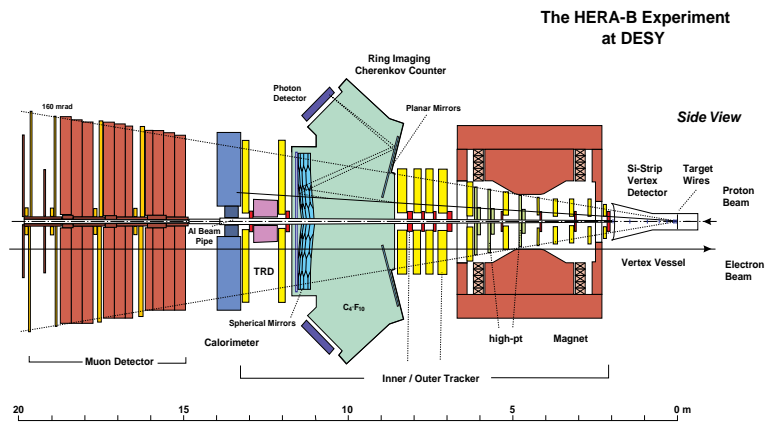Figure 2.3: Belle detector cutout diagram.

Figure 2.4: Diagrams of: (*top*) the HERA-B detector (at DESY, first beam in 2000) and (*bottom*) the LHC-b detector (CERN, to be completed in 2007).
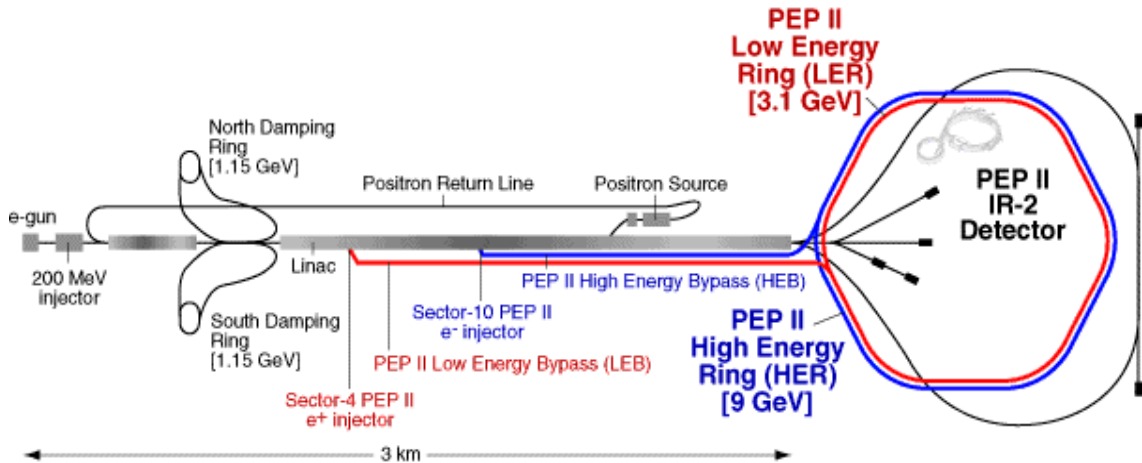
Figure 2.5: The PEP-II asymmetric storage ring and the SLAC linear accelerator. The SLAC linac is the injector for PEP-II. The single interaction point of PEP-II is at Interaction Region 2, where *BABAR* is situated.

The particle identification method also differs between *BABAR* and Belle: as will be described in Section 2.6, *BABAR* uses quartz bars to internally reflect Cerenkov light to a backward-mounted detector (the DIRC), whereas Belle uses an aerogel Cerenkov detector. In addition, *BABAR* has a 5-layer silicon vertex detector (SVT, see section 2.3) that can do standalone tracking (important for $D\overline{D}$), whereas Belle uses a 3-layer silicon vertex detector.

Figure 2.4 shows the design of the HERA-B and LHC-b experiments. Each of these experiments uses hadron beams, with, in the case of HERA-B, a fixed (tungsten wire) target in the beam halo, and, for LHC-b, colliding proton beams. Hadrons do present a challenging (but potentially very rewarding) environment for B physics.

2.2   The PEP-II Asymmetric Collider

The design of PEP-II is shown in figure 2.5. The 9 GeV electrons and 3.1 GeV positrons are injected from the SLAC linac via bypass lines in the linac gallery. The beam parameters are listed in Table 1. PEP-II has surpassed design goals both in instantaneous and in average integrated luminosity.
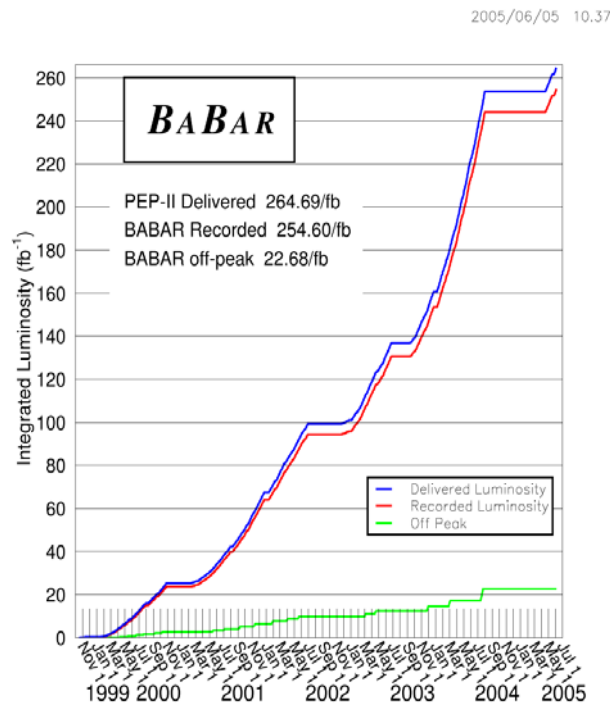
Figure 2.6: PEP-II -*BABAR* integrated luminosity since startup.

Parameters	Design	Typical
Energy HER/LER (GeV)	9.0/3.1	9.0/3.1
Current HER/LER (A)	0.75/2.15	1.21/2.04
# of bunches	1658	889
Bunch spacing (ns)	4.2	4.2-8.4
σ_{Lx} (μm)	110	110
σ_{Ly} (μm)	3.3	4.1
σ_{Lz} (mm)	9	9
Luminosity ($10^{33}\,\mathrm{cm}^{-2}\mathrm{s}^{-1}$)	3	8-9
Luminosity (pb^{-1}/d)	135	423

Table 2.1: PEP-II beam parameters. Values are given for the design and for colliding beam operation at time of writing. HER and LER refer to the high energy e^- and low energy e^+ ring, respectively. σ_{Lx}, σ_{Ly}, and σ_{Lz} refer to the R.M.S. horizontal, vertical, and longitudinal bunch size at the IP.

Most of the data is taken at the $\Upsilon(4S)$ resonance (10.58 GeV), however approximately 12% are taken at 40 MeV below the resonance to allow studies of non-resonant background in data. A plot of PEP-II integrated luminosity as a function of time is in figure 2.6.

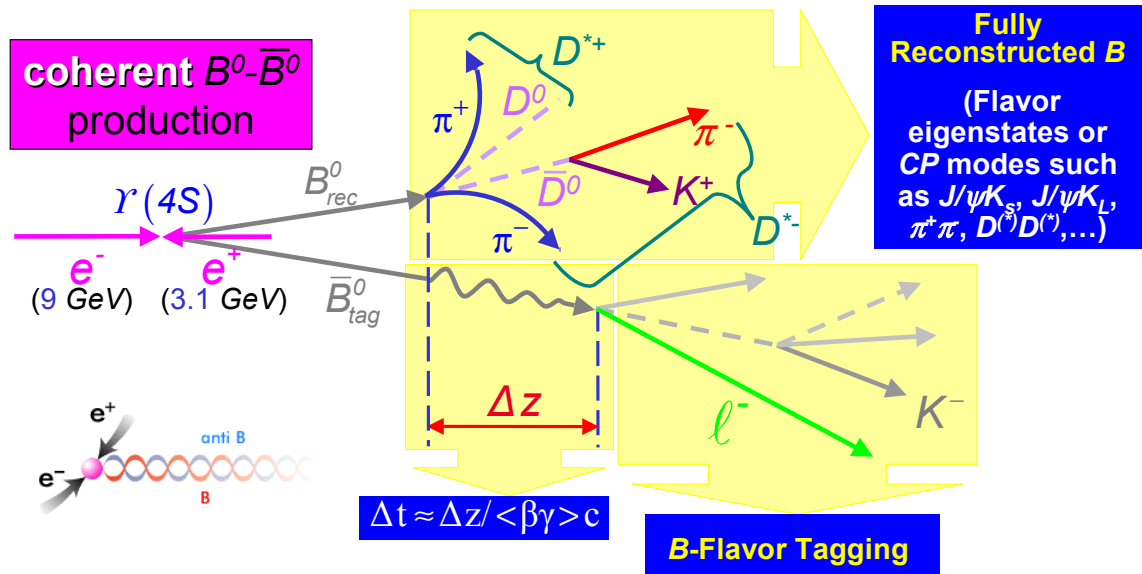## 2.3   Overview of Experimental Technique at the $\Upsilon(4S)$

Figure 2.7: Experimental reconstruction technique used for measuring time-dependent CP-violating asymmetries at an $\Upsilon(4S)$ asymmetric collider. A coherent $B\overline{B}$ pair is produced from the $\Upsilon(4S)$ decay, which allows determination of reconstructed neutral B flavor as a function of decay time.

In order to measure time-dependent CP-violating asymmetries at the $\Upsilon(4S)$, one must (of course) first reconstruct a neutral B decay mode that can exhibit CP violation, such as $B^0 \rightarrow D\overline{D}$ or $B^0 \rightarrow J/\psi K_s^0$. However, that is merely the first step. After signal event reconstruction, the additional tracks in the event (which correspond to the decay products of the other B [the "tag side B"]) must be used to determine whether the other B in the event was a B^0 or $\overline{B}^0$, due to the fact that the CP asymmetry is opposite for B^0 and $\overline{B}^0$ (see equations 1.53 and 1.54).

After both the event reconstruction and the flavor tagging are completed, the difference
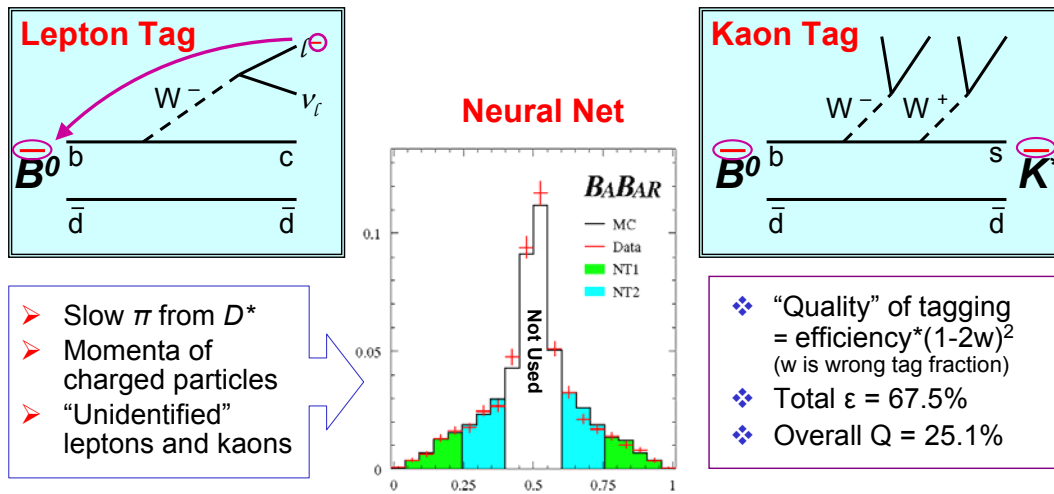
Figure 2.8: Technique used for tagging the flavor of the opposite-side B. Lepton and kaon charge is correlated with the flavor of the B. For events with no obvious lepton or kaon, a neural net is used to attempt to extract the flavor.

in vertex z-position[1] between the reconstructed B vertex and the tag side B vertex must be determined. This difference, Δz, is (very nearly) proportional to the decay time difference Δt between the two B decays. Δt is the time measurement over which the CP-violating asymmetry can occur, and is input (as t) in equations 1.53 and 1.54. Figure 2.7 gives an overview of this reconstruction method.

Figure 2.8 briefly describes the technique used for flavor tagging. The sign of charged leptons and kaons in the event (which are not part of the reconstructed B) is correlated with the flavor of the tag side B. A cut-based selector using *BABAR*'s electron, muon, and kaon identification capabilities is used to select signal events with a lepton or kaon on the tag side, and from this determine the flavor of the tag side B. For events which are not cleanly tagged by the cut-based selector, a neural net algorithm is used to extract the flavor of the tag side B. The neural net uses information including slow pion charge, jettiness of the tag side tracks, and recovery of leptons and kaons which are not cleanly identified in order to reconstruct the tag side flavor. The overall efficiency of tagging is 74.0% and the fraction of tagged events which are given an incorrect tag is 16.8%. The error on time-dependent asymmetries is proportional to $Q = \epsilon(1 - 2w)^2$ where ϵ is the efficiency and w is the wrong-tag fraction. This quality

---

[1]The z-axis in *BABAR* is along the direction of the beam line, with electrons (and the center-of-mass boost) pointing toward $+z$ in the lab frame.
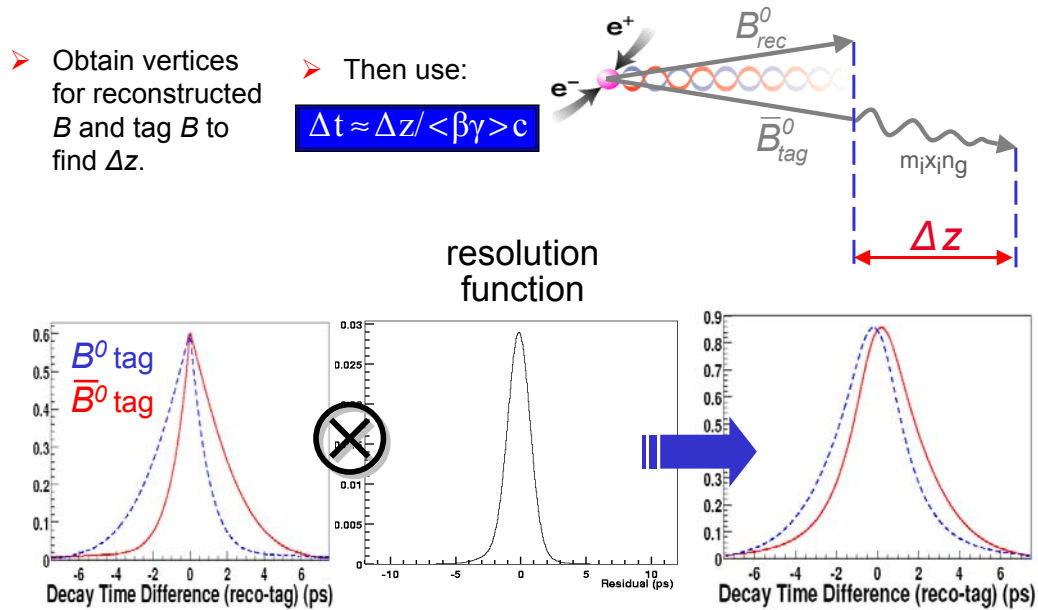
Figure 2.9: Δt measurement and resolution function. The difference in reconstructed z-position of the tag and reconstructed B decay vertices is used to determine the time difference Δt.

factor Q is 29.7% for *BABAR*'s tagging algorithm.

Figure 2.9 briefly describes the Δt measurement and resolution function. A clustering algorithm is used to determine the vertex position for the tag side B decay; the error on this position dominates the resolution. CP violation evinces itself as a difference in Δt distribution depending on whether the flavor tag is B^0 or $\overline{B}^0$, but this decay time distribution is convoluted by the error of Δt. Fully reconstructed B events which have definite flavor (such as $B^0 \to D^{*+}\pi^-$ or $D^{*+}\rho^-$) are used to determine both the mistag fractions and the parameters of the resolution function (which is modelled as a triple gaussian) in data (for more details please see Section 7.4.2).
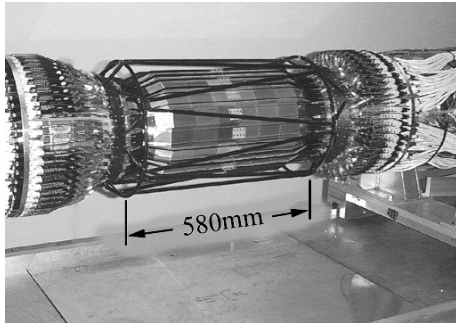
Figure 2.10: Fully assembled SVT. The silicon sensors of the outer layer are visible, as is the carbon-fiber space frame (black structure) that surrounds the silicon.
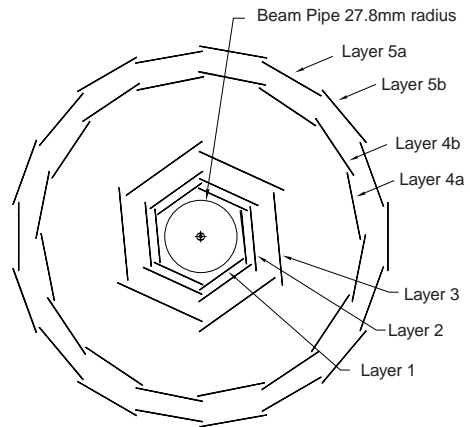

Figure 2.11: Transverse section of the SVT.

2.4 The Silicon Vertex Tracker (SVT)

The SVT contains 5 layers of silicon, double sided with conductive strip sensors. Strips on the opposite sides of each layer are orthogonal: ϕ strips run parallel to the beam axis and z strips run transverse to the beam direction.
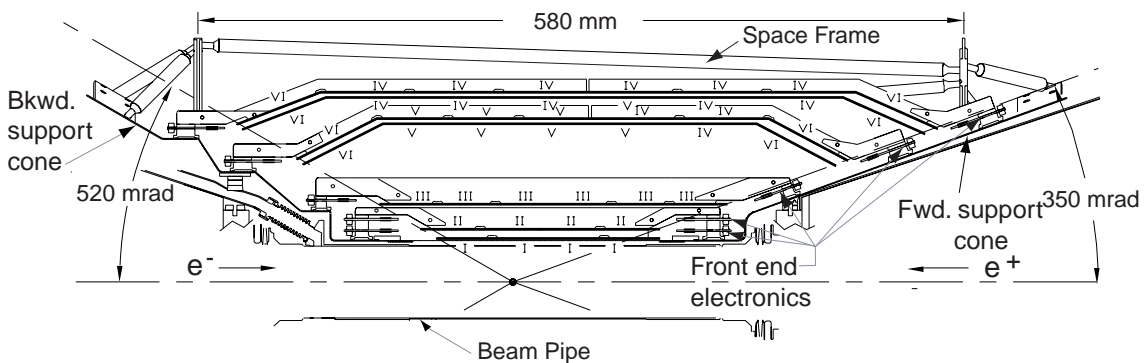

Figure 2.12: Longitudinal section of the SVT.

Together, the SVT and the central tracking drift chamber (DCH) form the charged particle tracking system (see also the following 2 sections). Precise and efficient measurement of track 4-momentum is necessary for full reconstruction of B meson decays, which tend to have multiple charged decay products. In addition, good vertex (and Δz) resolution and accurate extrapolation to the outer subdetectors is essential for reconstruction and background subtraction. Thus, accurate charged particle tracking and vertexing is required.

The 5 layers and relatively long radial separation between SVT detector layers provide both standalone track pattern recognition and refinement of drift chamber tracks via addition of SVT hits. The necessity of precise measurements close to the interaction point for Δz measurement and for background rejection using vertex quality, and for efficient reconstruction of low momentum tracks (such as slow pions from D^* decays), drive the requirements for the SVT.

The SVT silicon is composed of n-type substrate with p^+ and n^+ strips on opposite sides. The bias voltage ranges from 25-35 V. The layers of the SVT are divided radially into modules, shown as line segments in Figure 2.11. The modules in the inner 3 layers are straight along the z-axis, while those in layers 4 and 5 are arch-shaped, as shown in Figure 2.12. The arch design was selected to minimize the amount of silicon as well as increase the angle of incidence of tracks originating at the IP which cross the arch "lampshades" near the edges of acceptance. The total active silicon area is 0.96 m^2.

The strip pitch (width) varies from 50 to 210 μm depending on the layer (inner layers are more closely bonded). The strips are AC-coupled to the electronic readout. Only approximately half the strips are read out; most have an unconnected "floating strip" between each pair of active strips (to reduce cost of readout electronics without adversely impacting performance). Digitization is performed by an ATOM ("A Time-Over-Threshold Machine") chip at the end of each set of 128 strips, which amplifies, digitizes, and buffers the signal from each channel. The ATOM chip compares the charge accumulated on each strip with an (adjustable) threshold of 0.95 fC, and records the time in clock intervals (30 MHz for the SVT) for which each strip is over threshold. This information is then delivered to a computer farm for further processing upon an accept signal from the Level 1 Trigger (see section 2.9).

A variety of monitoring checks and calibrations must be performed on the SVT to maintain data quality. Perhaps the most important of these from an avoidance-of-equipment-damage perspective is radiation protection. Currently, twelve silicon PIN

diodes surround the support cones and monitor both instantaneous radiation and accumulated dose. The beam is automatically aborted if radiation levels are above 1 Rad/ms threshold. So far, the SVT is well below the operational limit of 4 MRad integrated dose. The silicon PIN diodes have a temperature-dependent leakage current that increases with absorbed radiation dose. Due to absorbed doses of over 2 MRad in some diodes, the leakage current in these diodes is much higher than the current induced by the radiation. The temperature is monitored very precisely but it is a challenge to correct for the temperature dependence of the leakage current, and the annealing and reverse-annealing effects due to radiation damage. During the 2005 summer shutdown it will be installed a system of diamond sensors inside the SVT. Diamond sensors grown by chemical vapor deposition (CVD) have no significant leakage current and are much more radiation hard than silicon PIN diodes. With a bias voltage of 500V applied across a 500-μm-thick polycrystalline CVD diamond sensor, the size of the signal due to a minimum-ionizing particle is more than 50% of that for a signal from a 300-μm-thick silicon sensor. The existing twelve silicon PIN diodes are mounted on the outside of support rings at the small end of each of the SVT support cones. We are assuming that the SVT will not be disassembled for replacement of SVT modules in the summer of 2005 and hence we will not have access to the existing PIN-diode sensors. However, we are assuming that the SVT will be removed from the beam-pipe so that we have access to the inside of the support cones for installation of diamond sensors. The diamond sensors will then augment (rather than replace) the existing silicon PIN-diode radiation sensors. For data quality calibration, channel gains and noise must be individually calibrated, and these are done online via an integrated pulse generator and calibration electronics. The offline reconstruction has the responsibility for calibration of the alignment of each SVT module. Alignment is critical for accuracy of vertexing and of tracking reconstruction, and is done in two steps. The local SVT alignment uses dimuon and cosmic ray events to calibrate the relative position of each of the 340 wafers. The global alignment then determines the overall position and rotation of the SVT with respect to the DCH.

The SVT has performed according to design essentially since its inception. A combined hardware and software hit-finding efficiency greater than 95% is observed, excluding the 4 (out of 208) readout sections which are defective. Single hit resolution for tracks originating from the IP averages 20 μm in both z and ϕ for hits on the inner 3 layers and 40 μm in z and 20 in ϕ for hits in the outer 2 layers. Before the summer

2002 shutdown there were 9 readout sections out of 208 that were not used in the DAQ. During the shutdown it was recabled the SVT and there was the possibilty to inspect closely all the modules with problems. This allowed us to fix 5 of the 9 problems and the last 4 sections do not have significantly impact on performances.

2.5   The Drift Chamber (DCH)

The DCH contains 40 layers of gold-coated tungsten-rhenium sense wires and gold-coated aluminium field wires in a mixture of 80% helium and 20% isobutane gas. There are a total of 7,104 sense wires and 21,664 field wires, with one wire per electronics channel. Wires are each tensioned (30 grams for sense wires, 155 grams for field wires) and pass through the aluminium endplates via feedthroughs made from Celenex insulating plastic around a copper wire jacket. The layers are grouped by four into 10 superlayers, with the wires in each superlayer oriented as either axial (directly parallel to the z-axis) or "stereo" (at a small angle in ϕ with respect to the z-axis, in order to obtain longitudinal position information). 6 of the 10 superlayers are stereo, and the other 4 are axial.[2] The DCH is asymmetric in z about the interaction point, as shown in Figure 2.15, to accommodate the forward boost of the center of mass of physics events.

---

[2]The arrangement is, from inner to outer, AUVAUVAUVA (A = axial, U = u stereo ($+\phi$), V = v stereo ($-\phi$)).
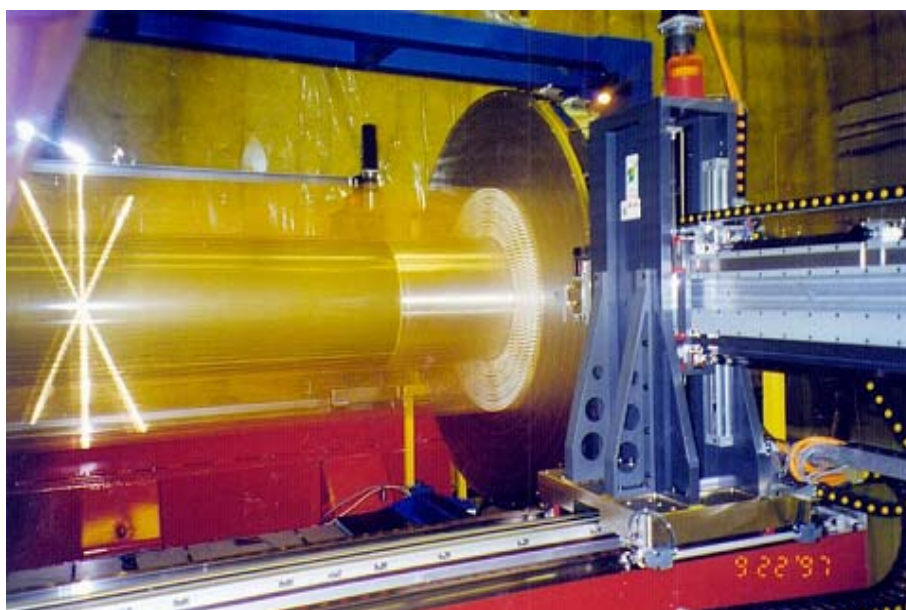
Figure 2.13: DCH wire stringing at TRIUMF (September 1997).

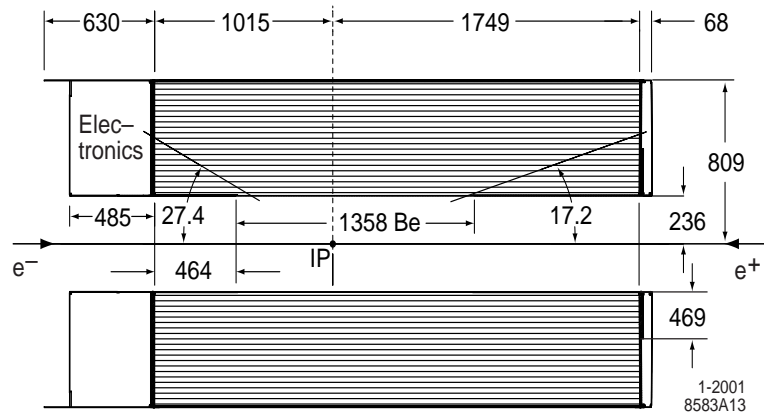Figure 2.14: DCH installation (August 1998).

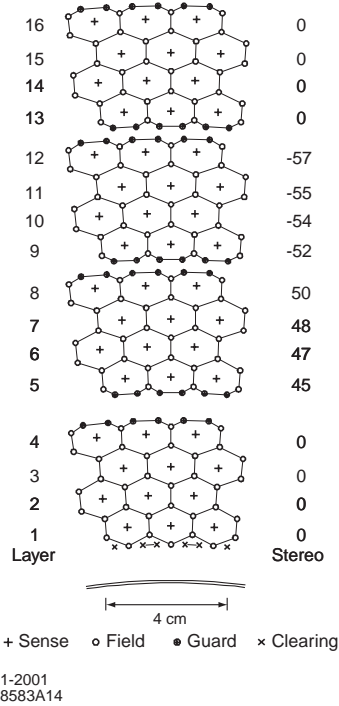Figure 2.15: Longitudinal section of the drift chamber.

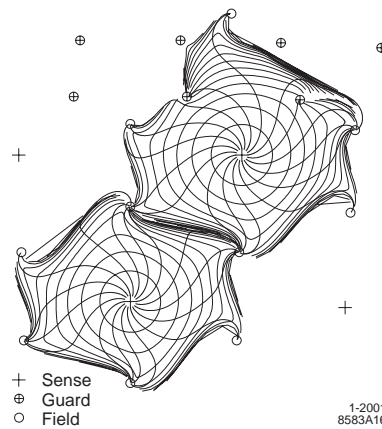Figure 2.16: DCH cell pattern (for a section of the inner 16 [of 40] layers).

Figure 2.17: DCH cell drift isochrones for cells in layers 3 and 4 (axial). Isochrones are at 100 ns intervals.
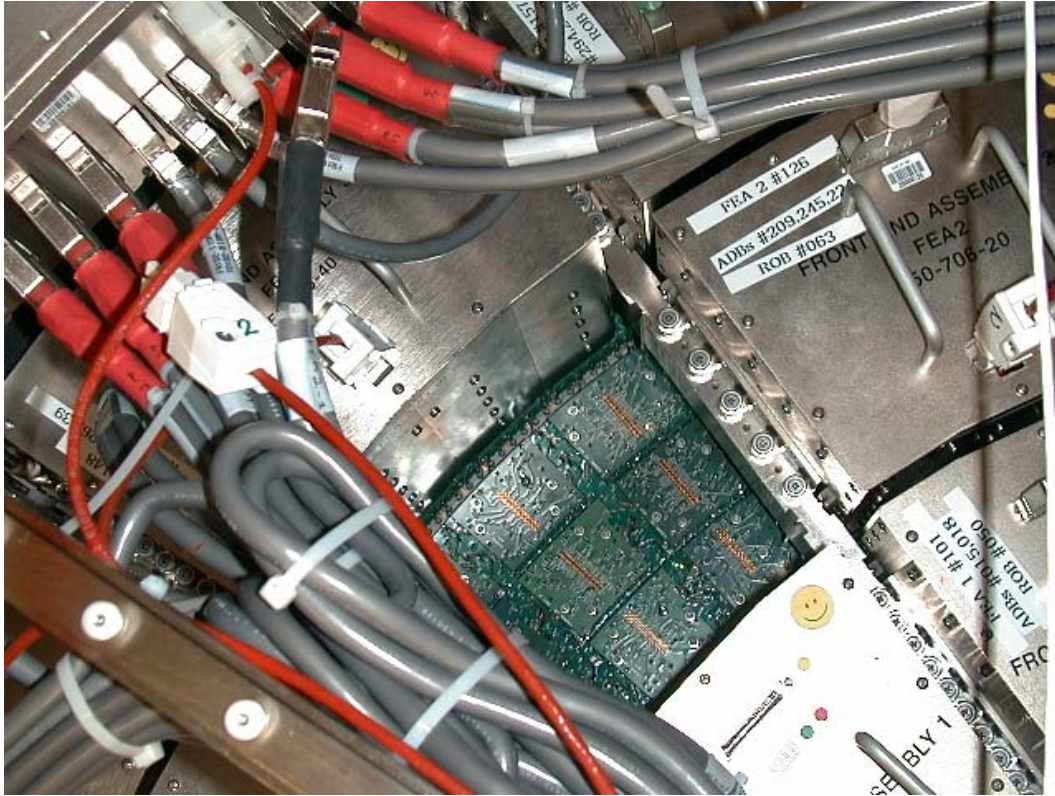
Figure 2.18: Partial view of drift chamber front-end electronics.

The endplates are 24mm thick aluminium, except for the outer 33.1 cm of the forward endplate, which is reduced to 12 cm to minimize the amount of material in front of the forward calorimeter endcap. The inner cylinder is fabricated from beryllium (to minimize the multiple scattering for the section of inner cylinder within the tracking fiducial volume) and aluminium (for the rest). The outer cylinder is 1.6 mm carbon fiber on 6 mm thick honeycomb Nomex core. The total thickness of the DCH is 1.08% X_0.

The cells are arranged in a hexagonal pattern, each with a sense wire at the center and field wires at the corners, as shown in figure 2.16. Cells on a superlayer boundary have a slightly different arrangement, with two guard wires taking the place of a single field wire. The nominal operating voltage is 1930 V. Isochrones and drift paths, calculated using the GARFIELD simulation, are shown in figure 2.17.

The DCH electronics are designed to provide accurate measurements of signal time and integrated charge (as well as providing information to the Level 1 Trigger,

see Section 2.9). Service boards plug directly onto the wire feedthroughs on the rear endplate. These boards distribute the high voltages as well as pass signal and ground to the front-end electronics assemblies. The front-end assemblies (FEAs) plug into the service boards and amplify, digitize, and buffer (for 12.9 μs) the signals. A view of the front-end electronics including (enclosed) front-end assemblies and service boards below can be seen in figure 2.18. The digital data is sent, upon receipt of a level 1 trigger accept signal, via 59.5 MHz serial link to a data I/O module which transmits the signal to the external electronics via fiber-optic cable. Extraction of hit time and integrated charge from the digital waveform takes place in the readout modules (ROMs) in external electronics.

Online calibrations of channel gain and threshold are performed daily via internal pulse generation. The data are monitored online to check for FEA or other electronics failure or for miscalibrated output. Monitoring and control of high voltage, radiation protection (using silicon PIN diodes similar to the SVT, as well as RadFETs for integrated dose measurement), the gas system, and temperature are performed, similar to other subsystems, via a slow control system based on EPICS.

Offline calibrations of the time-to-distance relation within cells, as well as of the deposited charge used for particle identification via dE/dx measurement, are performed. The time-to-distance relation is determined from two-prong events (Bhabha scattering events and dimuons) and is fit to a sixth-order Chebychev polynomial for each cell layer, with separate fits to right and left sides of wires (to account for $E \times B$ asymmetries). A correction for time-to-distance variations as a function of track entrance angle to the cell is detemined via simulation (not calibration) and added to the calibrated entrance-angle-averaged relation. The energy loss per unit length of tracks, dE/dx, contains particle type information due to the dependence of dE/dx on particle velocity (Bethe-Bloch relation), and is derived from measurements of integrated charge deposited in each cell along the track path. An overall multiplicative correction to the charge measurements due to gas pressure and temperature variations is performed once per run; additional calibrations due to variations with track entrance angle in ϕ and in θ are performed only when high-voltage settings are changed.

The design goal for the average drift distance resolution was 140 μm. An average resolution of 110 μm is achieved. The drift distance resolution as a function of drift distance can be seen from the offline monitoring plot shown in figure 2.19 (left side). Particle identification using the drift chamber provides significant information up to

high momenta, as can be seen in figure 2.19 (right side).
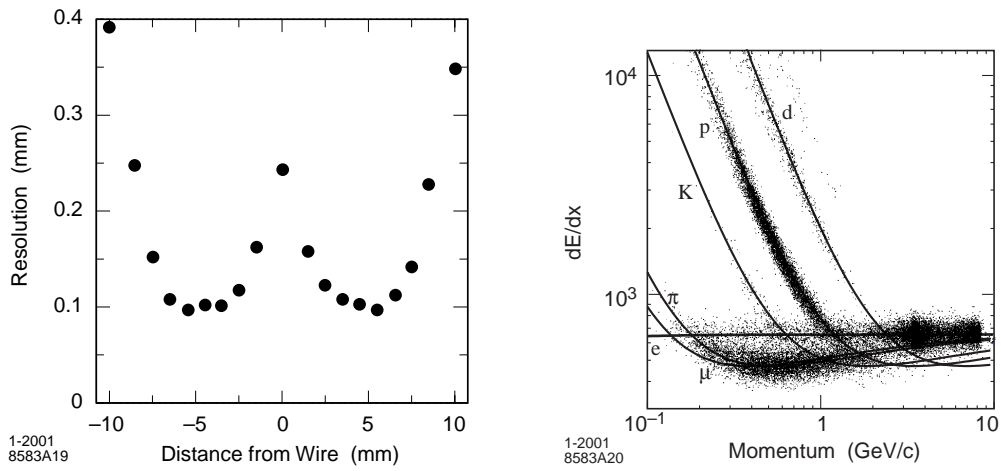

Figure 2.19: DCH drift distance resolution as a function of the drift distance in the cell (left); DCH particle identification as a function of momentum using dE/dx (right).
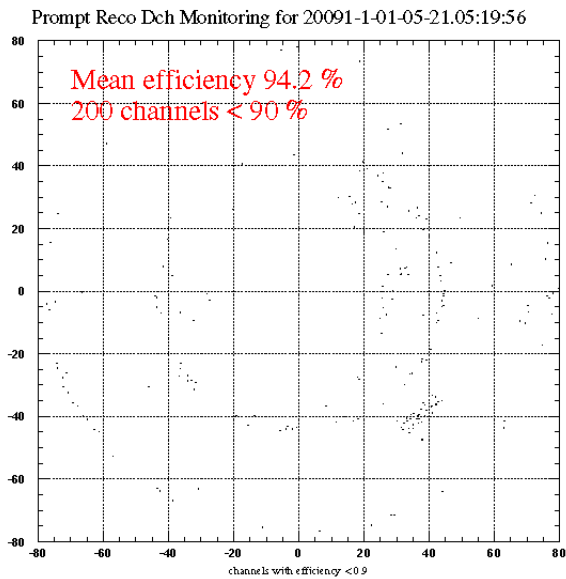

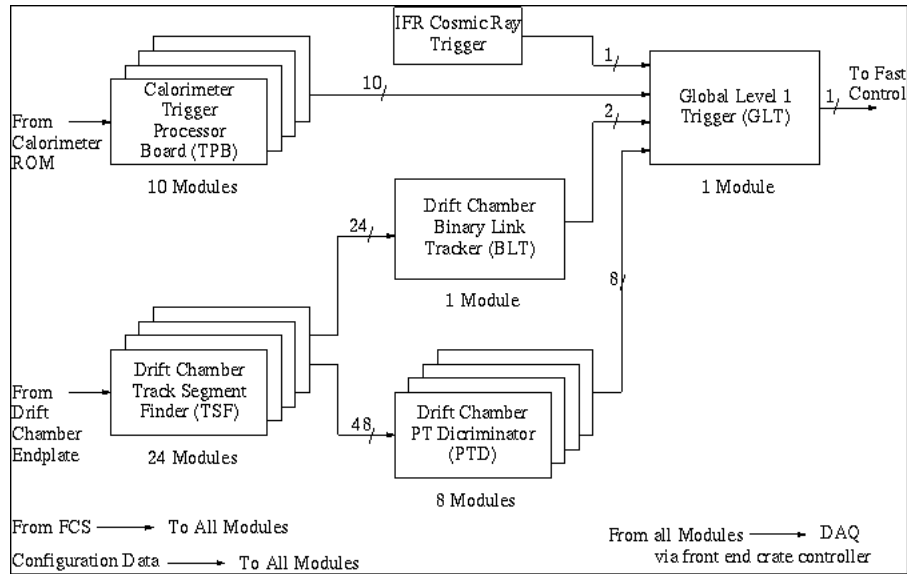
Figure 2.20: DCH channel efficiency.

Figure 2.21: Trigger L1 scheme.

Cell-by-cell channel efficiency is also monitored; typical efficiency is 90-95%, as may be seen in figure 2.20 (including a small region damaged from a high-voltage accident early in the commissioning phase, this can be seen towards the lower right of the figure as a higher concentration of points).

2.6   The Trigger and the Tracks Reconstruction

The *BABAR* trigger needs to provide high efficiency that is well-understood and stable for physics events. Since the events which pass the trigger must be fully reconstructed in the offline event reconstruction, the output rate must be no higher than 120 Hz to satisfy computing limitations of the offline processing farm. Since events with either a DCH track or a > 100 MeV EMC cluster occur at 20 kHz, the trigger is responsible for scaling this rate down by a factor of > 150 while accepting over 99% of B events, over 95% of hadronic continuum, and over 90% of $\tau^+\tau^-$ events. It also must be flexible enough to deal with changing background conditions, as this can happen at any given time at *BABAR*, without impact on physics or increase in online dead time (which must be $< 1\%$). The *BABAR* trigger is implemented in two levels, a Level 1 hardware trigger (called L1), and a Level 3 software trigger (called L3); a Level 2 trigger is used in some other high energy particle physics experiments, but was not needed for *BABAR*.

The Level 1 trigger consists of four subsystems: the Drift Chamber Trigger (DCT)

a trigger for charged particles, the Calorimeter Trigger (EMT) for neutral particles, an IFR Trigger used for calibration and works as cosmic trigger (IFT), and global electronics for producing the final L1 accept signal (GLT stands for Global Level Trigger). The DCT and EMT receive information from the Drift Chamber and Calorimeter detectors, respectively, process it, and send condensed data to the Global Trigger. The GLT attempts to match the angular locations of calorimeter towers and drift chamber tracks, and flexibly generates Level 1 triggers and sends them on to the Fast Control and Timing system (FCTS), based on the results of the processing. The GLT also uses the IFT information to independently trigger on cosmic ray and mu-pair events. The Level 1 trigger has been upgraded since 2004 with a new DCT system which performs 3D tracking using stereo wire information from the Drift-Chamber to obtain $\sim 4cm$ resolution in track Z (along beamline) coordinates of tracks to imporve background rejection. The Level 1 trigger rates are typically 2.5 Khz at a luminosity of of $L = 8 \times 10^{33} cm^{-2} s^{-1}$. The various stages of the L1 system operate at 4Mhz to 15MHz intervals with a total L1 trigger latency of ~ 11 microseconds.

The Level 3 then analyzes the event data from the Drift-Chamber and Calorimeter sub-systems in conjunction with the L1 trigger information to further reduce background events. Besides the physics filters. L3 trigger also performs Bhabha veto, selection of various calibration events and critical general online monitoring tasks. The L3 operates on an online farm which consists of 28 Dell 1650 (dual Pentium-III 1.4 GHz) computers with fast algorithms processing at $\sim 4ms$ per event. The L1 triggers are reduced by typically a factor of ~ 10 after the L3 filtering, before logging to the data storage system

The DCT is further subdivided azimuthally into Track Segment Finders (TSF), a binary link tracker for producing tracks from the segments (BLT), and a p_t discriminator (PTD). The set of TSF modules received 7104 "hit" signals originating in the 7104 cells of the drift chamber. The search for track segment is organized in terms of pivot cells. Physically, pivot cells are the cells in the third layer, called pivot layer, of each superlayer. Each pivot cell and seven neighboring cells constitute a pivot group. Some of the cells are shared with other pivot groups, but each pivot group has one unique pivot cell (see Fig. 2.22): Each segment finder engine reeives continuous digital-discriminator signals from the eight cells of the pivot group assigned to that engine. The cells in a pivot group are numbered 0 through 7, as shown in Fig. 2.22 (cell 4 is the pivot cell). Note that if the pivot group template (the black circles in the figure)
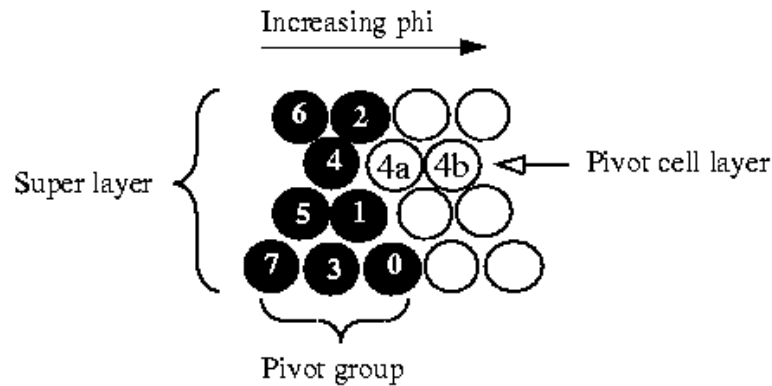
Figure 2.22: Showing the definitions of pivot cell and pivot group. Numbers indicate the cell number within a pivot group; the pivot cell is number 4. 4a and 4b indicate adjacent pivot cells.

were to move one cell to the right, a new pivot cell (cell 4a) and a new pivot group would be defined. Note also that the signals from some cells are needed for more that one engine. In particular, cells labeled "7", "3" and "0" are associated with two other pivot groups.

The complete Segment Finder consists of 1776 track segment finder engines, one of each of the 1776 pivot cells (pivot groups). Each engine processes data from the eight cells in its assigned pivot group to find valid track segment that pass through its pivot cell and other cells in the pivot group. The engine can be programmed to require a hit in each of the four layer (4/4), or in at least three of the four layers (3/4), to accept a track segment as valid. Typically, valid segment patterns consist of hits, close together in time and in three of four layers, that could represent acceptable tracks which fall within a pre-defined range of azimuthal angles. Sets of valid segment patterns are stored in a pattern memory within each engine.

A two-bit counter is associated with each wire (cell). When a segment is hit its counters start being incremented at regular time intervals. At any given time the 16 bit pattern formed by the counters gives the segment address. A lookup table (LUT) is written to the read-out modules of each configure transition from the database. The LUT is calibrated to translate segment addresses to track ϕ position estimates and "weights". Five bits are available for ϕ. ϕ=0 corresponds to weight 0 and values 29-31

are not used. ϕ, therefore, ranges between 1 an 28 and the integer values correspond to:

- 01-07: half of the left neighboring segment

- 08-14: left half of the segment

- 15-21: right half of the segment

- 22-28: half of the right neighboring segment

In this numbering scheme the pivot wire is at 14.5, the segment boundaries are at 7.5 and 21.5 and the neighboring pivot wires are at 0.5 and 28.5.

The weight ranges between 0 and 3. For the LUT used at the time of this writing the meaning of the weight is the following:

- 0 - pattern is not in the LUT. ϕ is set to 0.

- 1 - no ϕ to estimate for the pattern (ϕ is set to 14), or ϕ lies outside the segment.

- 2 - ϕ inside the segment.

- 3 - ϕ inside the segment, better resolution that weight 2.

L3 tracking algorithms do not use weight 0 segments. For weight 1 the pivot wire position is used as the track ϕ coordinate. For weight 2 and 3 segments integer ϕ estimates are converted to absolute track ϕ position estimates.

Considering a pattern of hits in a superlayer, all the wires in the pattern can be attributed to one TSF segment (delineated with a solid line). However, this segment shares wires with a neighboring segment (delineated with a broken line), therefore, there will be hits in two TSF segments for this pattern. Once the principal segments (typically with higher weight) have been used to find a track pattern, remaining ghost segments can form another track pattern to produce an additional "ghost" track, as may be seen in Fig.2.23

The binary link tracker (BLT) receives this information and detemines whether segments lie in a road defined by "supercells," which are sectors of a superlayer covering to 1/32 of the DCH in ϕ. Patterns of segment-containing supercells that appear to correspond to tracks (according to the BLT look-up table) are output to the L1 global trigger. In parallel with the BLT, the p_t discriminator (PTD) checks TSF segments in
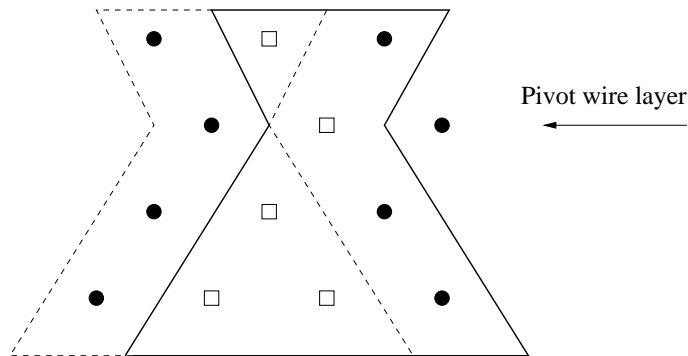
Figure 2.23: Ghost segment.

axial superlayers to see if they are consistent with a track having a greater p_t than a configurable minimum cutoff value. This information is also output to the GLT.

The level 1 calorimeter trigger (EMT) divides the EMC into 280 "towers" of 24 crystals each (22 for the endcap). All crystal energies within a tower which are above a 20 MeV threshold are summed and supplied to the EMT trigger processor boards (TPBs). The TPBs digitally filter the energy deposition (to smooth the output waveform of noise) and compare neigboring towers to look for clusters which span more than one tower. Trigger line "primitives" (bytes corresponding to trigger type and information) are output to the GLT corresponding to the energy and placement of found clusters.

The global level 1 trigger (GLT) receives the trigger line primitives from the EMT and DCT, along with information from an IFR trigger (IFT) which is used for cosmic ray and dimuon calibration purposes, and performs timing alignment to reduce jitter. The GLT does some rudimentary matching between DCT tracks and EMT clusters, and performs a logical AND of the input trigger primitives, which defines the output trigger line. The combined L1 trigger efficiency is $> 99.9\%$ for generic $B\overline{B}$ events, 99% for continuum, and 94.5% for $\tau^+\tau^-$ events.

Complete reconstruction of B decays (in addition to other major *BABAR* analysis techniques, such as tagging) requires precise and efficient charged particle tracking. As will be seen later, separation of decays in these modes from combinatoric background requires precise determination of mass and energy, which in turn requires precision measurement of track momentum. The majority of other modes are just as dependent on charged particle tracking. Data from the DCH and SVT is combined to satisfy the stringent charged particle tracking requirements of *BABAR*.

Charged tracks are parametrized by the 5 variables $d_0, \phi_0, \omega, z_0, \tan \lambda$ and their
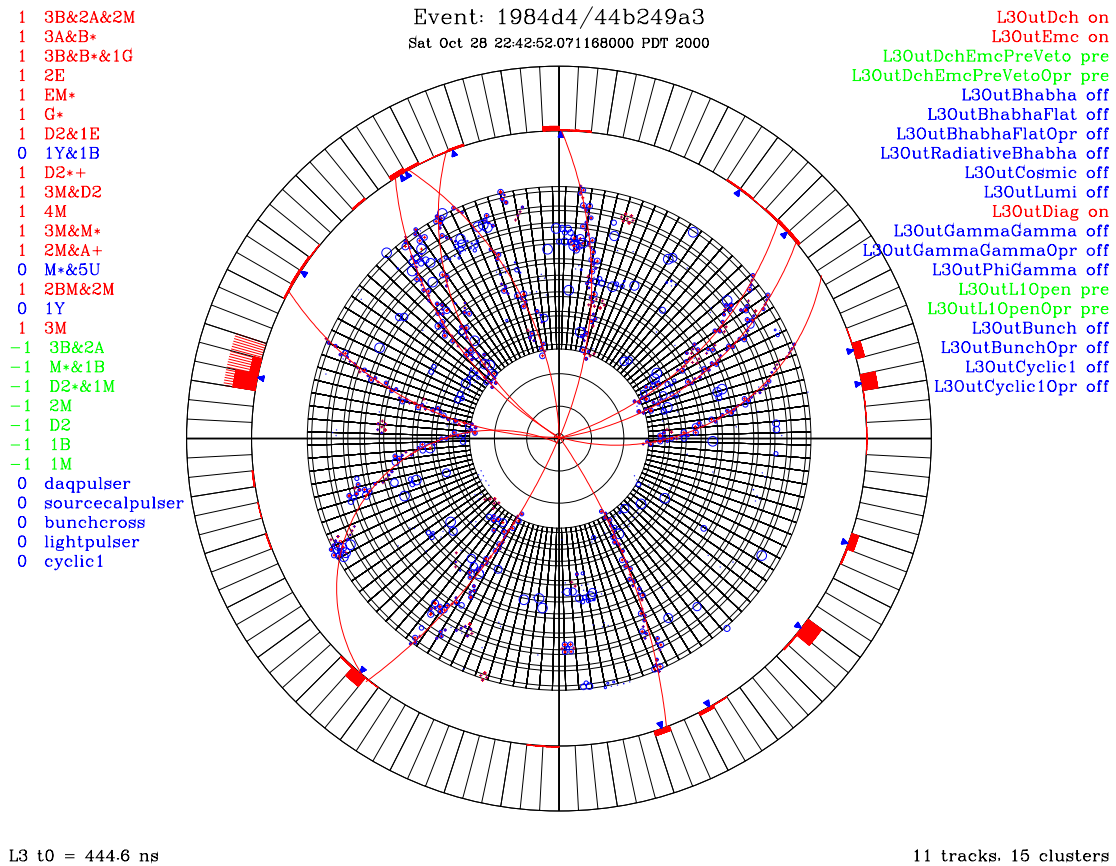
Event: 1984d4/44b249a3

Sat Oct 28 22:42:52.071168000 PDT 2000

1	3B&2A&2M
1	3A&B*
1	3B&B*&1G
1	2E
1	EM*
1	G*
1	D2&1E
0	1Y&1B
1	D2*+
1	3M&D2
1	4M
1	3M&M*
1	2M&A+
0	M*&5U
1	2BM&2M
0	1Y
1	3M
−1	3B&2A
−1	M*&1B
−1	D2*&1M
−1	2M
−1	D2
−1	1B
−1	1M
0	daqpulser
0	sourcecalpulser
0	bunchcross
0	lightpulser
0	cyclic1

L3OutDch on
L3OutEmc on
L3OutDchEmcPreVeto pre
L3OutDchEmcPreVetoOpr pre
L3OutBhabha off
L3OutBhabhaFlat off
L3OutBhabhaFlatOpr off
L3OutRadiativeBhabha off
L3OutCosmic off
L3OutLumi off
L3OutDiag on
L3OutGammaGamma off
L3OutGammaGammaOpr off
L3OutPhiGamma off
L3OutL1Open pre
L3OutL1OpenOpr pre
L3OutBunch off
L3OutBunchOpr off
L3OutCyclic1 off
L3OutCyclic1Opr off

L3 t0 = 444.6 ns

11 tracks, 15 clusters

Figure 2.24: A level 3 trigger event display for a multihadron event.

error matrix. The parameters are defined as: d_0 is the distance of the track to the z-axis at the track's point of closest approach to the z-axis, z_0 is the distance along the z-axis of that point to the origin, ϕ_0 is the azimuthal angle of the track at that point, λ is the dip angle with respect to the transverse plane, and ω is the curvature of the track and is proportional to $1/p_t$. After tracks are recognized by the pattern recognition alorithms, these 5 variables are fitted, and error matrices are extracted. Offline track reconstruction begins with tracking and event time information from the L3 Trigger.

2.6.1 t_0 **Reconstruction**

L3 provides both tracks and an estimate of the time at which the interaction occured (with a resolution of approximately 5 ns), referred to as the t_0.[3] Reconstruction of the event interaction time, or t_0, is necessary for both fitting DCH tracks (since the DCH time-to-distance relation is necessary for position information of a track within a given cell, a time must be provided as input) and for rejecting out-of-time hits within the SVT to reduce background. t_0 reconstruction takes place in several steps, iterated with track pattern recogition since the two are interdependent, during offline reconstruction. The value of t_0 is used for drift time to drift distance conversion. The drift distances are used in track fits, therefore, t_0 finding and tracking efficiency and resolution are directly related. For example, tracks coming from the interaction point will be missed if t_0 finding latches on background hits, or a cosmics track instead. Beam background typically produces clusters of adjacent TSF segment hits. These are looked for and removed from t_0 finding. Note, that for an ioninzing particle the time-of-flight in the DCH (of order of several ns) is much smaller than typical ionization drift time (of order of $500 \, \mathrm{ns}$). Only segments belonging to track patterns found in event are used for initial t_0 finding. The initial t_0 estimate is obtained by subtracting a constant value of $220 \, \mathrm{ns}$ from the drift time average for all the wires in those segments. Time-of-flight is not taken into account.

If no track patterns have been found $500 \, \mathrm{ns}$ is used as the initial guess, but t_0 finding will very likely fail. The initial t_0 estimate is iteratively improved. Iterations are stopped after 5 iterations or if the time estimate changes from iteration to iteration by less than $5 \, \mathrm{ns}$. If t_0 finding fails on first iteration on second the initial time estimate is incremented by $200 \, \mathrm{ns}$. If t_0 finding fails again on third iteration initial time estimate is decremented by $200 \, \mathrm{ns}$. t_0 estimates calculated are only calculated for TSF segments in which all 4 wires (2, 3, 4, 5) or (4, 5, 6, 7) (Fig. 2.22) are hit. t_0 finding efficiency could possible be improved if other patterns are also used. Time-of-flight is crudely taken into account by assuming that the particle's flight length is equal to the radius of the pivot layer. (A better estimate of the flight length could be obtained for TSF segment belonging to tracks, by using track parameters). TSF segment time estimates are accumulated in a histogram. (Two binnings are used to avoid splitting a peak into two bins.) If no bin contains 3 entries or more -20000 is returned, otherwise the average of entries in the highest bin is returned.

---

[3]The e^+e^- interaction time is referred to as the "bunch t_0," often shortened to "t_0."

Inefficiency in t_0 finding for these events directly translates into tracking inefficiency. t_0 finding algorithm should be modified to use more hit configurations for segments and use associated track information, if available. This should allow to recover t_0 for most of these events. t_0 finding efficiency then could be as high as 93%.

2.7 Track fitting

Before tracks are fitted a second pass of track pattern finding is done. However, this time a fit is attempted to every track pattern found. For a successful fit hits will be removed from the hit map for the cells used in the fit. Because the hit map is cleared of hits in a different manner track patterns found in pass two will in general be different from those found in pass one.

Fitting for track parameters is done by a least squares minimization of

$$\chi^2 = \sum \left(\phi_{\mathsf{ipt}}(k, d_0, \phi_0, t, z_0) - \phi_{\mathsf{est}} \right)^2$$

The sum runs over DCH superlayers, ϕ_{est} are the estimates for TSF segments and ϕ_{ipt} are track intercepts that have a non-linear dependence on the track parameters. The system is solved iteratively. Given a seed track the expression for ϕ_{ipt} is linearized around seed track parameters using track intercept derivatives to obtain an easily solvable linear system. The iterations are described below.

The seed track corresponding to a track pattern is used to perform prefitting. TSF ϕ estimates are used for the prefit. d_0 and z_0 are fixed to zero and the other 3 track parameters are allowed to vary. The fitted track is used as the seed track in the next fit. Fits 1 - 4 are 5 parameter fits, each iteratively improving on the previous one. For each intercepted cell two cells to the left and two to the right are considered. The one with the ϕ estimate for TSF segment closest to the intercept is selected. Fitting fails if fewer than 6 TSF segments are available, of if for seed track $P_t < 225\,\mathrm{MeV}$ or $|d_0| > 15\,\mathrm{cm}$. For each layer ϕ errors are estimated and outlier hits (beyond 3 ϕ errors) are counted. If there are no outliers and 10 segments were used for the fit it is declared successful. For fit number 4 it's only required that there be no outliers.

Finally if the fit does not succeed after 4 iterations a final fit is done where segments used in fit number 4 are refitted using with the fit number 4 output used as the seed track.
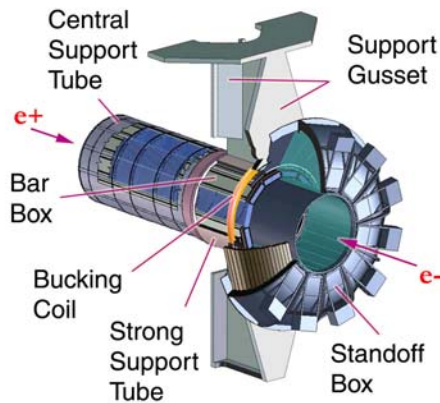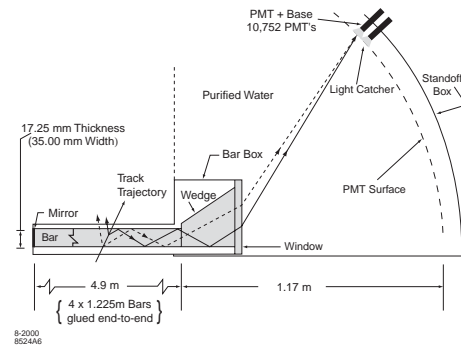
Figure 2.25: View of DIRC mechanical stucture.

Figure 2.26: DIRC schematic showing the principle behind PID measurements. The Cerenkov angle is preserved through specular internal reflection.

The L3 tracking efficiency is about 95% above 2 GeV/c in transverse momentum, sinks to about 80% for 1 GeV/c and further down for lower transverse momenta until it reaches 0 for a transverse momentum of 180 MeV. This is the transverse momentum of a track which curls in the drift chamber.

2.8   The DIRC

BABAR has stringent requirments for $\pi - K$ separation over a large momentum range. At the lower end of the range, primarily at momenta < 1 GeV, flavor tagging using kaons from cascade decays is an efficient way of determining B flavor. At the high end of the range, reconstructing $B^0 \to \pi^+\pi^-$ and $B^0 \to K^\pm\pi^\mp$ requires separation at momenta up to 4.2 GeV in the lab frame. At intermediate energies, reducing background in charm decays such as $D^0 \to K\pi$ is necessary for $B^0 \to D\overline{D}$ reconstruction. The particle identification device must exhibit sufficient $\pi - K$ separation throughout this wide range of momentum with a minimum of material in order to avoid adversely impacting calorimeter resolution.

The DIRC (Detector of Internally Reflected Cerenkov light) principle uses internal reflection within quartz bars to propagate Cerenkov light to readout phototubes while preserving the Cerenkov angle. This requires extremely flat surfaces in order to avoid
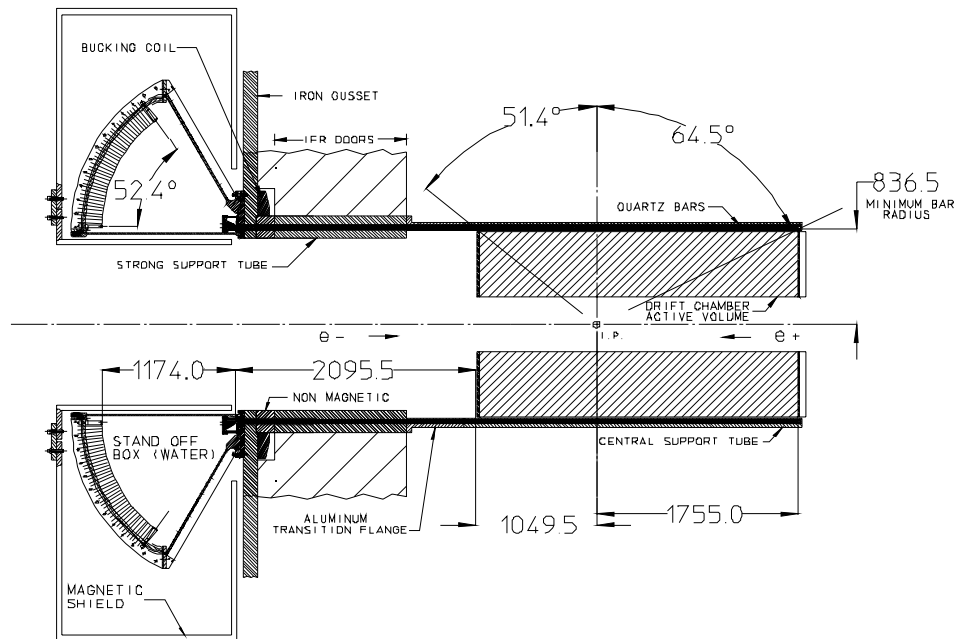
Figure 2.27: Longitudinal section of the DIRC. Length units are mm.

dispersing the reflected angles. Fused, synthetic silica quartz is used due to the excellent optical surface it allows through polishing, as well as other favorable properties such as long attenuation length, low chromatic dispersion, small radiation length, and radiation hardness. As shown in figure 2.26, the light is internally reflected down to a wedge to reflect photons into a water-filled "standoff box." The standoff box is enclosed by an array of 10752 photomultiplier tubes, which are each 29 mm. in diameter. The Cerenkov light from a particle passing through the DIRC forms a ring (essentially a conic section) imaged on the phototubes. The opening angle of this conic section contains information on particle type via the typical relation $\cos \theta_c = 1/n\beta$, with β being the particle velocity normalized to the speed of light, and n being the mean index of refraction (= 1.473 for fused silica).

Both efficiency and the timing of the electronics are critical for DIRC performance. Timing is critical for two reasons: one, for background hit rejection, resolving ambiguities, and separation of hits from differing tracks within an event; and two, timing gives information on the photon propagation angles, allowing an independent measurement of the Cerenkov angle. The intrinsic timing resolution of the PMTs is limited to 1.5 ns by transit time spread. Data from the phototubes is read out to front-end electronics, which performs the amplification, digitization, and buffering. Reduction of data from
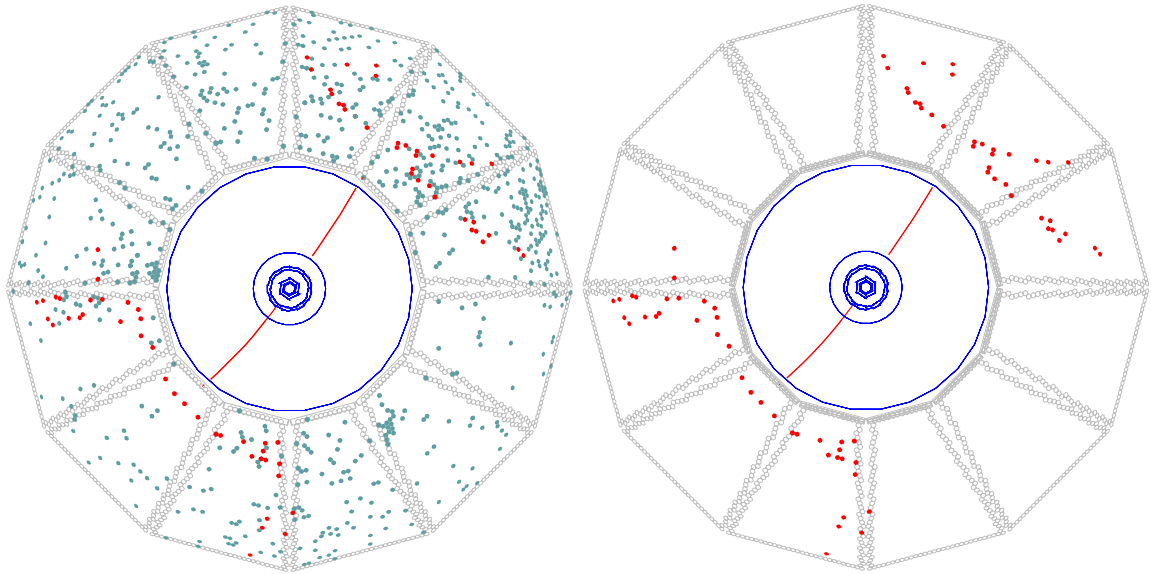
Figure 2.28: Display of an $e^+e^- \rightarrow \mu^+\mu^-$ event reconstructed in *BABAR* with two different time cuts. On the left, all DIRC PMTs with signals within the ± 300 ns trigger window are shown. On the right, only those PMTs with signals within 8 ns of the expected Cherenkov photon arrival time are displayed.

out-of-time or noisy PMTs is performed in in the external electronics and reduces the data volume by 50% using rough timing cuts. Online calibration of PMT efficiency, timing response, and electronics delays uses a light pulser system which generates precise 1 ns flashes from blue LEDs inside the SOB.

The DIRC has performed well throughout *BABAR*'s operational lifetime: 99.7% of PMTs are operating with design performance. The measured time resolution is 1.7 ns, very close to the intrinsic resolution of the PMTs. The Cerenkov angle resolution for dimuon events is 2.5 mrad, close to the design goal of 2.2 mrad. This results in $\pi - K$ separation at 3 GeV of 4.2σ. The mean kaon selection efficiency and pion misidentification for a "loose" selection are 96.2% and 2.1% respectively, as can be seen in figure 2.29. This results in dramatic background rejection with little signal loss for charm reconstruction, as may be seen in figure 2.30.

2.9   The Electromagnetic Calorimeter (EMC)

The design parameters for the *BABAR* EMC are driven by the requirements of precisely measuring energies over a spectrum from 20 MeV to 9 GeV in a 1.5 T magnetic field
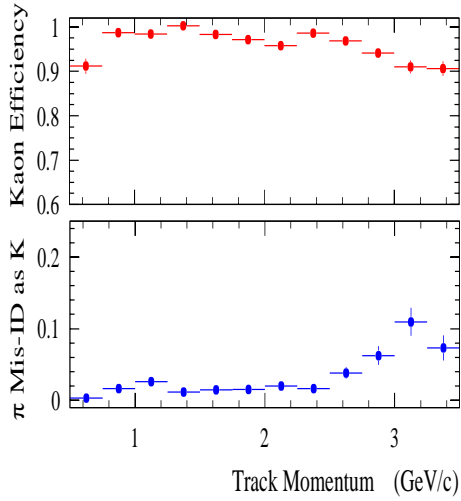
Figure 2.29: Kaon selection efficiency and misidentification probabilities as a function of momentum.
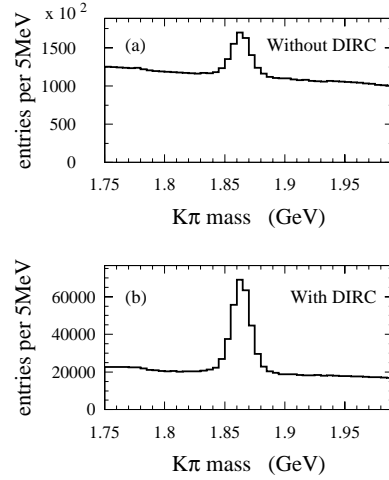
Figure 2.30: Inclusive $K\pi$ invarant mass spectrum (a) without and (b) with the use of the DIRC for kaon identification.

and a high radiation environment. At the high end of the spectrum, measurements of QED processes such as Bhabha and two-photon scattering, as well as (at slightly lower energies) photons from the critical physics processes $B^0 \rightarrow \pi^0\pi^0$ and $B^0 \rightarrow K^*\gamma$ decays, present the motivating incentive. The need for efficient detection of photons from high multiplicity B decays containing π^0's determines the requirement for the low end of the spectrum. *BABAR* uses a thallium-doped cesium iodide (CsI(Tl)) crystal calorimeter in order to achieve the necessary energy and angular resolution to meet these physics requirements.

The EMC contains a cylindrical barrel and a conical endcap containing a total of 6580 CsI(Tl) crystals. The crystals have nearly square front and rear faces with a trapezoidal longitudinal cross-section. They range in length from 29.6 to 32.4 cm with a typical front face dimension of 4.7 x 4.7 cm. A diagram can be seen in figure 2.31. The crystals are mounted in thin (300 μm) carbon-fiber composite housings which are mounted on an aluminium strong-back (see figure 2.32). Although light incident on the crystal boundary is internally reflected, the small part that is emitted is reflected back with a coating of white reflective TYVEK on the outer surface. Surrounding that are thin layers of aluminium and mylar to act as RF shielding and electrical insulation respectively. On the rear face of the crystal, two 1 cm^2 silicon PIN diodes with quantum efficiency of 85% for CsI(Tl) scintillation light are mounted via transparent
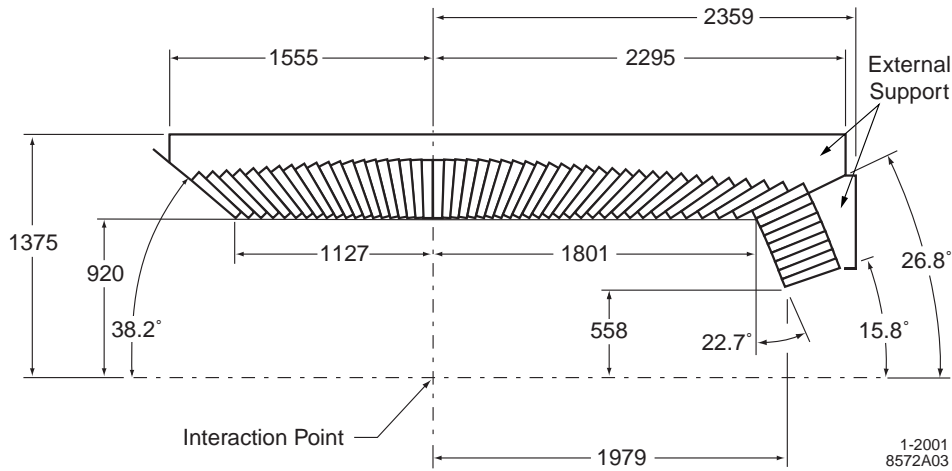
Figure 2.31: Longitudinal section of the EMC. Length units are mm.

polystyrene substrate.

Each diode is connected to a low-noise preamplifier which shapes and amplifies the signal by a factor between 1 and 32. The signal is then transmitted to mini-crates at the end of the barrel (see figure 2.32) where a digitization CARE ("custom auto-range encoding") chip provides an additional variable amplification factor. Unlike other subsystems (except for the IFR), the EMC does not buffer the data on front-end electronics; rather it outputs the full digital datastream to the read-out modules in external electronics, which perform, on receipt of a level 1 accept signal, a parabolic fit to the digitally filtered datastream to derive energy and time measurements.

A variety of online calibrations and checks is performed, including a neutron source which produces a monoenergetic 6.13 MeV calibration signal and a xenon flash light pulser system. Offline energy calibrations are necessary for higher energy corrections. The relation between polar angle and energy of Bhabha and radiative Bhabha scattering events is used to calibrate the 0.8-9 GeV range. The middle range is covered by π^0 calibration, which constrains the mass of a sample of π^0's to the known value, extracting correction coefficients.

The clustering pattern recognition uses a seed crystal algorithm to establish energy clusters. Local energy maxima within a cluster are used (if there are more than 1) to separate the cluster into bumps. Charged particle tracks are associated with bumps using a χ^2 consistency cut. In an average hadronic event, 15.8 clusters are detected, of which 10.2 are not associated to a track.
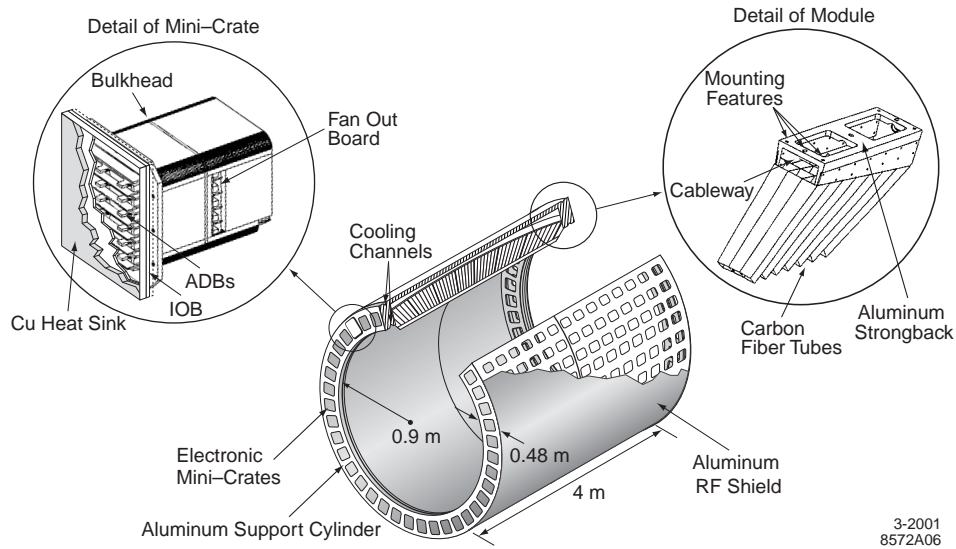
Figure 2.32: The EMC barrel support structure, modules, and mini-crates.

Energy resolution is determined using $ChitoJpsig$ and Bhabha scattering events to be

$$\frac{\sigma_E}{E} = \frac{(2.32 \pm 0.30)\%}{\sqrt[4]{E(\text{ GeV})}} \oplus (1.85 \pm 0.12)\% \tag{2.1}$$

and angular resolution is determined using π^0 and η decays to be

$$\left(\frac{3.87 \pm 0.07}{\sqrt{E(\text{ GeV})}} + 0.00 \pm 0.04\right) \text{mrad.} \tag{2.2}$$

As can be seen in figure 2.33, the reconstructed π^0 average width is 6.9 MeV. The separation of electrons from charged hadrons using the ratio of shower energy to track momentum (E/p) and other variables may be seen in figure 2.34:
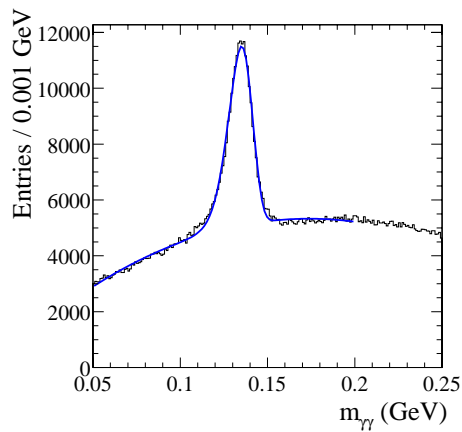
Figure 2.33: Two photon invariant mass, using photons between 30 and 300 MeV.
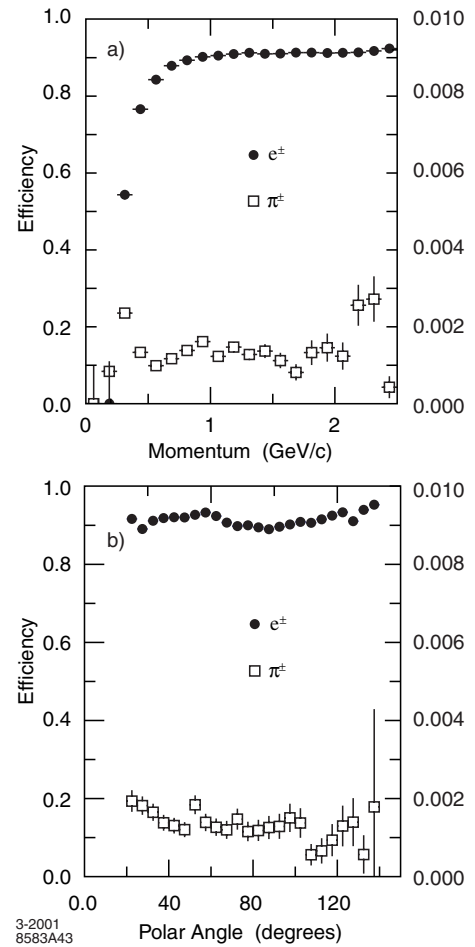
Figure 2.34: Electron efficiency and misidentification as a function of (a) momentum, and (b) polar angle.
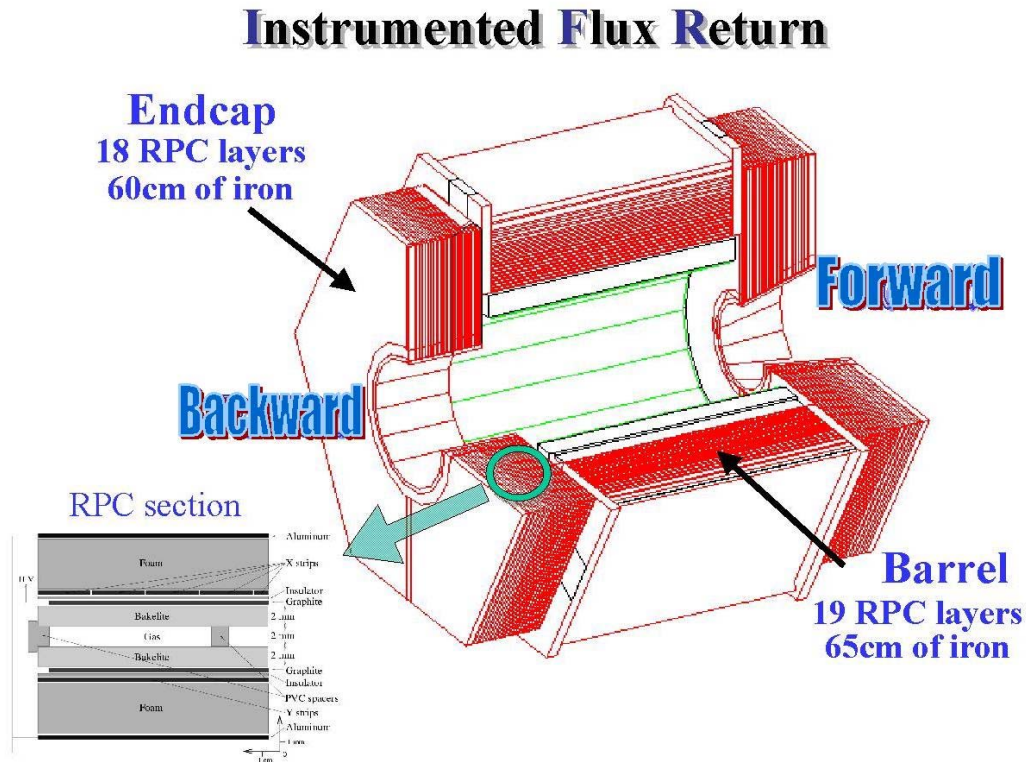
Figure 2.35: The instrumented flux return modules, structure, and RPCs.

2.10   The Instrumented Flux Return (IFR)

Detection of neutral hadrons (primarily K_L^0's) and muons is necessary for several *BABAR* analyses and analysis techniques. Muons provide a very clean B flavor tag, extremely useful for increased efficiency in tagging the opposite-side B for time-dependent CP violation measurements. Muons are also necessary for reconstructing $J/\psi \to \mu^+\mu^-$, as well as for measuring semileptonic branching fractions, required for extracting magnitudes of CKM elements. K_L^0 reconstruction is critical for the $B^0 \to J/\psi\, K_L^0$ channel. Initially, *BABAR* used an Instrumented Flux Return (IFR) composed of layers of resistive plate chambers (RPCs) and steel plates in order to provide enough material to separate pions and kaons from muons and to efficiently detect the presence and position of both μ and K_L^0 over a large solid angle. As shown in figure 2.35, the IFR consists of layers of planar RPCs in a barrel and endcap (red lines) as well as 2 layers of cylindrical RPCs (green lines) between the EMC and the magnet. Between the RPC layers are steel plates of thickness varying between 2 cm (inner plates) to 10 cm (outer plates). The total mass of the IFR is 870 metric tons. Planar

RPCs contain a 2 mm Bakelite gap with ~ 8 kV across it. Ionizing particles which cross the gap create streamers of ions and electrons in the gas mixture (which is typically 56.7% Argon, 38.8% Freon, and 4.5% isobutane) which in turn creates signals via capacitive coupling on the "x-strips" and "y-strips" on opposite sides of the RPC. Strip width varies between 16 mm and 38.5 mm. The 2 mm gap is kept constant using polycarbonate spacers spread at 10 cm intervals and glued to the Bakelite. The Bakelite surface is smoothed with an application of linseed oil. Cylindrical RPCs are composed of a special thin and flexible plastic, rather than Bakelite, and have no linseed oil or other surface treatment. They are laminated to cylindrical fiberglass boards. In 2003 they decided to replace the present RPCs in the gap of the *BABAR* IFR with plastic Limited Streamer Tubes (LST). After testing, they were persuaded that LST's are the most straightforward, practical and reliable detectors among the various options to instrument the barrel region, access to which has been and will be continue to be difficult and in some cases impossible. A "standard" LST configuration consists of a silver plated wire 100 μm in diameter, located at the centre of a cell $9x9mm^2$ section. A plastic (PVC) extruded structure, or "profile", contains 8 such cells, open on one side 2.36.

The profile is coated with a resistive layer of graphite, having a typical surface resistivity between 0.2 and 1 MΩ/square. The profiles, coated with graphite and strung with wires, are inserted in plastic tubes ("sleeves") of matching dimensions for gas containment. The signals for the measurement of one coordinate can be read directly from the wires, but it has become customary instead to read both coordinates with strip planes, thereby avoiding the complications of feedthroughs and DC-blocking capacitors. For such tubes the operating voltage is typically 4.7kV; the efficiency plateaus are at least 200V wide; the signals on the wire are of the order of 200/300mV (into 50Ω), typically 50ns at the base, sometimes with an afterpulse. The gas mixtures are strongly quenching: the original one (25% Ar, 75% n-pentane) being explosive has been replaced in accelerator use by a non-flammable one based on CO_2.

The LST geometrical efficiency is limited by the ratio of active versus total volume in the cell. The effect is mitigated by the fact that most tracks do not impinge perpendicularly. In the gap between iron slabs is wide enough, the inefficiency can be greatly reduced by using larger cells or, alternatively, a double-layer geometry.

The LST tubes are somewhat fragile mechanically so careful design, handling, and operation are of paramount importance in preventing failures. The "mortality" of the
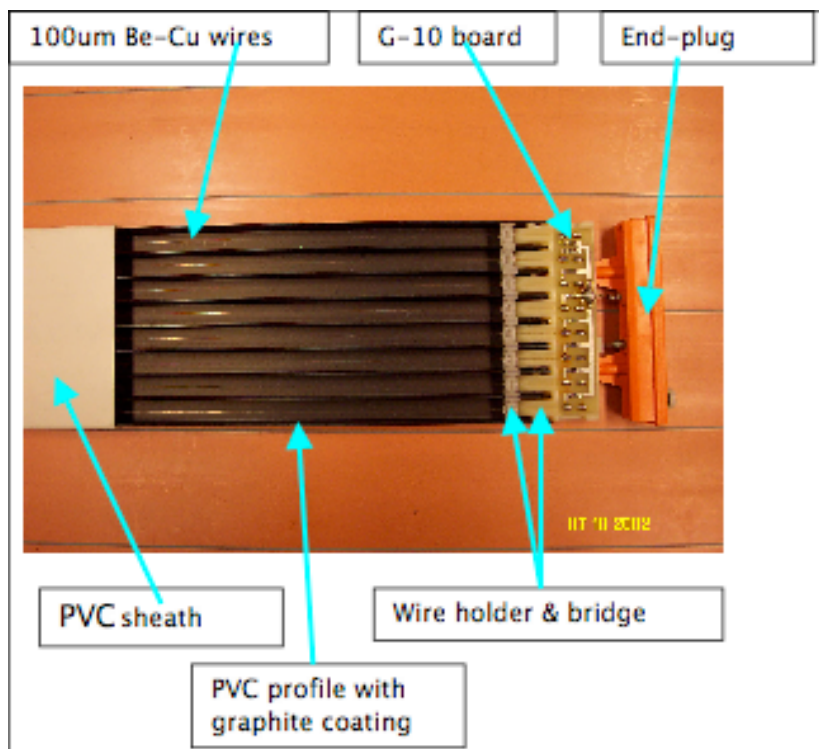
Figure 2.36: Photo of a standard LST, partially inserted in the sleeves

LST's depends on the cell size, on the care and attention given during construction and installation, and on the strictness of the acceptance tests. If we consider the performance isses, we have:

- minimize dead spaces. These include the profile walls, separation between tubes, dead areas at the tube ends, both inside the sleeves and outside, for electronics, gas and cabling

- reduce tube mortality and/or introduce redundancy to decrease its effect on detector efficiency

- arrange tubes into modules that can be extracted and replaced without removing corner pieces

- feed each tube with one or more independent HV channels

- locate HV distribution boxes and front end electronics on the outside of the detector to avoid having to doors to repair.

The cell efficiency was studied by a simple Monte Carlo simulation, reproducing tracks going through standard-cell LST and it's esistimated around 5-10%. Results from measurements made with cosmic rays on stardard tubes and on the first batch of double layer prototypes are consistent with these numbers. In addition the overall efficiency of the detector depends on the dead space at both ends of the LST and in between the LST.

Instead of recycling the existing IFR Front End Cards (FEC), it has been decided to build a new FEC. The new FEC's have a different input section but with the same interface to the existing IFR-FIFO boards, which is used for the readout of the LST's and are well integrated in the *BABAR* Data Acquisition (DAQ). The data format will be the same as it was in the RPC system. This choice allows us to use the present DAQ software and electronics also with the LST system. Compared to the old FEC's, two new functions are provided: front-end amplification and a settable threshold. The electronics is located just outside the detector in a set of 12 crates. The new system will be based on boards which serve 64 channels: 4 input connectors, 64 amplifiers and comparators, and a Field Programmable Gate Array (FPGA) which will contain all the digital logic (delay, gate with the trigger, latch) for the 64 channels. The baseline plan is to route the utilities (gas, HV) to the detector layers of a sextant, as well as

the signals from the z cathode strip planes thorughout 2 dedicated conduits located at the backward end of each sextant. The Φ-strip signals will be routed throughout 2 dedicated conduits located at the forward end of each sextant. The baseline plan includes suitable fixtures to the LST endplugs to help in an orderly routing of the utilities and the signal cables at the detector layer. These structures will occupy about 8cm at the backward end and 3cm at the forward end.

Reconstruction of clusters proceeds via two methods: a standalone method where groups of hits along 1 dimension within a module are joined to form one-dimensional clusters, which are then combined with opposite-side hits to form two-dimensional clusters, and then with other modules to form 3D clusters; and a "swimmer" method, where charged tracks are propagated to the IFR — 1D clusters within 12 cm. of the expected path are combined to form 2D or 3D clusters. Clusters which are not matched to a charged track are considered as neutral clusters. Muon identification uses variables such as number of expected vs. actual interaction lengths tranversed and the χ^2 match to the charged track.

Chapter 3

BaBar software

3.1 Introduction

In this and in the following chapters will be presented framework and software tools used during this thesis work. This section includes a presentation of the simulation and the reconstruction programs used in *BABAR* collaboration.

The system includes two parts: *online* system (data acquisition, checking and monitoring) and *offline* system (reconstruction, simulation and data analysis). It is implemented on PC with commercial Unix operative systems (SunOS e OSF/1) and Linux.

3.2 Programming choices

In the *BABAR* experiment it is used a software developped using *Object Oriented* programming implemented on Unix machines.

We have a big choice in using object oriented codes [44]; among all possibilities, in *BABAR* collaboration C++ has been choosen for its specific demands: for example, large disponibility for compilers, distributed with free open-source licenses, compatibility with different platforms, efficiency of the code and tools for development and debugging and large disponibility of libraries.

3.2.1 Object oriented programming

The main feature of object oriented coding can be simplified through a analogy with real world: utilization of an object is not linked to knowledge, for an user, of its internal

operation. For example, to drive a car we hadn't to know how engine is and how it functions, but this (substantial) difference doesn't influence our driving.

This is an example of separation between *what* an object offers in functionality terms and *how* it realizes this functionality; the way to interface with an user should be costant in the time, but system can be modified, expanded and optimized. This feature is fundamental in complex software system codes, as used in *BABAR*.

In C++, tool that allows us to use object oriented programming is *class*, data types defined by programmer; they are composed of a public interface that give us functions to operate on contained data, and a hidden, private, structure that tipically includes both internal data representation and utility functions to operate on themselves. This way to hide effective implementation is called *encapsulation* and it's tipical for object oriented programming.

So, classes can be thought as boxes that speak each other with messages: we can operate on data for a class (that is most the interesting thing for an user) only through some function in public interface; these functions are called *methods*.

Such a way to operate can give us some advantages cause we can shield data from illegal operations and verify finished operations (verification on variation interval of a quantity, as in data input stage). Much more, it allows a re-utilization of the code (for example, a classes set to operate on vectors and matrices with usual addition, product and convolution operations etc.) and it reduces the development and software debugging times.

Another object oriented feature is objects hierarchy, illustrable with a real world example: it's possible to define some abstract data types with certain very general properties; in fact we are able to think to abstract objects, like a particle, and derive from these ones other objects with more definite properties, "boson or fermion?". Continuing in this hierarchy, we can specify more detailed properties, "if fermion: lepton or quark?" and reach up for more internal levels maintaining general class properties, leaving them as before or modifying parts of them. This feature is called *heredity* and we can have single heredity (if it derived by only one more general class) or multiple heredity (if derived by more classes).

Polymorphism is a concept strictly linked to heredity: it is the language ability to use some specific objects (derived by more or less generic classes) as if they were like generic class objects: for example, I could want a list with all particles with a fixed momentum, independently if they are bosons or leptons, and I'd want to use them in a

uniform way (for a fixed particles class definition).

3.3 Object oriented database

Recently, *BABAR*'s data storage has changed to a completely new system. The new model is called *CM2* ("Computing Model 2").

The original *BABAR* Event Store used two data-storage formats. The *Objectivity* database was a large object-oriented database with several levels of detail stored for each event. It could be used for almost any analysis or detector study. *Kanga* ("Kind ANd Gentler Analysis") datasets stored only the micro (see below) level information in ROOT-type files (architecture for object oriented data analysis developped by CERN) [45]. This is the level of detail required for most physics analysis jobs, and avoided the complication of interacting the full Objectivity database and the complications that often arose with it. The idea was to have Objectivity as the main database, and use Kanga files at remote sites.

The Objectivity database had four levels of detail: *raw*, *reco*, *micro* and *nano* (or "tag"). *Raw* and *reco* were very big databases that kept virtually all of the details from every event. *Micro* was a smaller, more user-friendly database that kept only information likely to be useful for physics analyses, rather than detector studies, or more refined analysis tasks. *Nano* ("tag") contained even less detail, and was used only to skim data for a few given key characteristics to save loading in the whole event information for each event (a time-consuming process). The original idea was to keep *raw* and *reco* information for jobs like detector studies. *Raw* and *reco* were infrequently used, and only a small part of the information was ever accessed.

The new CM2 Event Store has just one database, the *Mini*. The *Mini* database is basically an extended version of the *micro*, however with the additional capability to store information written into "skims" by users ("user data", see below). The *Mini* contains all of the information from the old *Micro* database, plus the small part of *Raw* and *Reco*. The new data storage format is more like *Kanga* than anything else, so we may refer to the CM2 Mini database as "CM2 Kanga," "new Kanga" or (since old-kanga is obsolete) just "kanga". Another difference between the CM2 Mini and the old database system is that the CM2 Mini allows for the storage of "user data": user-defined composite candidate lists and user-calculated quantities.

Here's a summary table of the differences between the old Objectivity/Kanga sys-

tem and the new CM2/Mini system:

	Old Objectivity/Kanga	**New CM2/Mini/Kanga**
Level of detail	Objectivity: high detail	Mini: intermediate detail
	Old Kanga: low detail	
Portability	Objectivity: central	Mini: central, but easily skimmed to make portable collections
	Old Kanga: portable	
User data	Objectivity: None (central database)	Mini: some user data in central database
	Old Kanga: Lots (small, user-defined collections)	

Table 3.1: Differences between the old system and CM2.

3.4 Code organization

BABAR software is accessible to all registered users through NFS system file (*Networked File System*) or AFS (*Andrew File System*), mounted on every UNIX workstation at SLAC.

The scheme is replied in all calculus labs in the countries that collaborate in this experiment: USA, France, England, Italy and Germany.

Analysis presented in this thesis work has been developped only on SLAC PCs.

3.4.1 BaBar Framework

BABAR software is organized like a framework for the event reconstruction coming from detector. For example to figure out what programming inside a framework means, it's possible to compare it with reality: in every home we find water, electricity, telephones, etc. and these services are supplied without worrying about how they realized them.

In software engineering, a framework supplies base services as I/O, graphic management, data scheme management. The obvious advantage is: low-level function problems have already been solved and generally in a very efficient way with few faults. So, the user can only work in his specific domain; in this way, it is favoured a re-use of a work (a well written code can so be re-used to solve similar problems even if not identical). A drawback can be operating inside the framework, but this stiffness can be considered not significant if framework has been planned cunningly.

3.4.2 Package

BABAR software is completely modular, and his base element is the *package*, defined as a classes set planned to solve certain exact problems very closer among them (for example a selectors package, or planned classes that assign a specific identity to a candidate particle). In every package we can find classes with same tasks, that differ for chosen approach or chosen operative tecnique. Many dozen of packages are avalaible, to cover a large spectrum of possibilities and requests coming from reconstruction and event analysis.

3.4.3   Release

We define *release* the set of all packages, each defined in his specific version. Like packages are updated with new classes added, releases are updated with new packages. Particularly, we can divide release in two parts: ones with a testing function for code implementation and ones considered stable, used for official analyses.

For this work it has been used the official stable release tagged with 12.5.2 (so called `analysis-21`), using Linux 7.2 platforms.

3.4.4   Module

BABAR framework base unity is defined as *module* and it can be or a package class or a user defined class based on other packages classes. The modules hold code that draws data from every event, runs specific algorithms and it can eventually give back results in the event in a such way that they can be used in next phases.

An executable analysis program is formed by one or more compiled and linked modules; each of them can be enabled or disabled during execution if it is useful in data processing.

Framework functionality management is left to TCL (*Tool Command Language*) language that has two features: it can interpret and so it can be an interface among user and framework, and for that, it can be used as a scripting language to check exactly the operations for every module, in a similar way with a Unix shell. It can be used on many platforms and it is a big advantage.

Modules can be added in a *sequence* in which they are executed in apparition order. Modules and sequences can be combined in a *path*, completed sequences start with an input module and finish with an output module.

The presence of particular filter modules can allow that a path will be finished before exiting and so a processed event won't reach output module. Multiple paths can be specified and each of them can be enabled or disabled.

3.5   Online system

BABAR Online software comprehend detector check and monitoring systems, processes related to data flow from front-end electronics to storaging in database or run checking programs. These tasks are solved by main Online system components: *Data Flow*,

Run Control, *Online Event Processing* (OEP) and *Prompt Reconstruction*. Another component exists, *Detector Control*, and it's not joined to event: it checks software and hardware detector components (for example DCH high tension system).

3.5.1 Online Data Flow (ODF)

Data acquisition system has a software and a hardware component; first one is called *Data Flow* while the hardware one is called *Platform*. Often, we refer to both of them as *BABAR Data Flow* [46].

Data Flow has task of joining all the data coming from front-end electronics, processing them in a preliminar way (so called *feature-extraction*) and delivering them to OEP.

Main platform elements are: checking masters that form trigger interface and distribute clock and command system, read-out modules (ROM), particular modules that catch data from front-end electronics and execute feature-extraction, and *bulk data fabric* that transport data inside-outside the platform.

Every platform needs a clock and an external trigger system; it has 32 input lines for the trigger that produce level 1 trigger acceptance signal (L1 accept) and then it propagates overall the platform. A platform can manage electronics for more than one sub-detector and they are able to operate independently, can't be independent because they are on a same platform. To maximize resources, such platforms are *partitioned*: in this way operations related to different detectors are done in parallel.

Data Flow platform has been drawn considering rigorous conditions due to experiment for dimensions and events frequency.

Components are organized in a hierarchy that permits to execute operations with a high-grade of parallelism.

3.5.2 Online Event Processing (OEP)

OEP receives completed events from Data Flow's Event Builder, executes level 3 trigger algorithms, checks data quality through so called *Fast Monitoring processes* and develops other tasks as supporting functions to calibration activities. Furthermore, OEP allows avalaible events for the reconstruction to *Prompt Reconstruction*.

Work done by OEP is distributed among knots of a farm composed by Unix machines. On every machine are solved identical processes parallelly.

3.5.3   Prompt Reconstruction

Prompt Reconstruction task is to reconstruct, in short times, all events that passed level 3 trigger filter, to furnish calibration constraints and informations on data quality. This allows us to diagnose immediately detector problems in such a way that they can be solved without losing integrated luminosity. This function has been specially important in the preliminar phases of the experiment. Many calibration constraints, like pedestals and electronics component gain, are evaluated through special runs, others, like DCH time-distance relationship and relative corrections of alignment between chamber and vertex detector, need a large number of reconstructed events. Prompt Reconstruction receives these quantities from a previous (but recent) dataset and applies to current data. Generated constraints by every reconstructed events block are storaged in Condition Database to be read again during following reconstruction block.

The Prompt Reconstruction results are monitored by *Prompt Monitoring* that checks for example chamber performances, data quality and reconstruction and calibration algorithms of reconstruction. Unlike Fast Monitoring, Prompt Monitoring analyzes reconstucted events and has a large numbers of informations on tracks.

3.6   Simulation

Completed simulation of the detector is formed by three parts: events generation, particles tracing through the detector and detector reply simulation.

3.6.1   Generators

Simulation process starts with event generation, using one of available different generators, of $B\overline{B}$ events with the corresponding decay channels, $q\overline{q}$ with $q = u$, d, s, c background events, e^+e^- diffusion events, and other backgrounds linked with accelerator operation. Furthermore, energies beams and interaction point position smearing are simulated; for each beam is used a single gaussian with width 5.5 MeV for the high energy beam, and 3.1 MeV for the low energy beam. Smearing for interaction point is in the x and y coordinates, respectively 160 μm and 6 μm, and it's simulated, for each coordinate, with a single gaussian. The z beam position is modelled on a flat distribution 1 cm long.

Most important events generator for $B\overline{B}$ is EvtGen. This generator furnishes a

scheme in which specific decay channels can be implemented as modules. Such modules, called EvtGen *patterns*, can solve different functions; for example, they can evaluate decay amplitudes. EvtGen introduces mixing, generating $\Upsilon(4S)$ decays in a user defined proportion of $B^0\overline{B}^0$, $\overline{B}^0\overline{B}^0$ and $B^0 B^0$ final states with correct Δt distributions; CP asymmetries are generated in modules which modify produced B mesons mean life distributions. They are available generic patterns to simulate two body decays in a scalar mesons pair, a scalar and a vectorial mesons, a tensorial and a scalar mesons or a vectorial mesons pair. Decay features (branching ratio, numbers of sons and patterns) are planned in a ASCII file called `DECAY.DEC`.

Generator manages only exclusive final states; for quarks to hadrons fragmentation we use Jetset7.4, and for this reason it is used for $q\overline{q}$ background generation, $c\overline{c}$ states and weak baryons decays. Jetset7.4 decay table has been updated to latest measurements.

3.6.2 BOGUS

BOGUS simulator (*Babar Object-oriented Geant4-based Unified Simulation*), using Geant4 package developed by CERN, allows us an unified simulation, in the sense that permits a completed and a faster simulation.

Geant includes tools to simulate detector geometry, charged and neutral tracks revelation through the detector, interactions and decays of every kind of particle, magnetic field and detector reply.

BOGUS is structuralized in some packages, one for every underdetector, in each of them are contained standard routines recalled in different simulation phases. Geometries of all under detectors are re-created starting from parameters hold in a format ASCII data bank, in which they are specified materials, dimensions, positions and orientations for every enabled and disabled under detectors and also the quantities for materials concerned an enabled detector.

Monte Carlo tracks hits are called in the *BABAR* terminology *GHits*. These contain all needed informations to obtain in a second phase detector reply simulation. *GHits* are written, with Monte Carlo truth, on an output file.

3.6.3   Detector reply

Tracks hits digitalization happens in another process called *SimApp*. This process is added as *GHit* input information and produces digitalized data as output in the same format of those producted by real detector. At the end of such a process, Monte Carlo data are processed by same code of real data. This code is organized like a subsystems packages set. These packages contain routines to give simulated data sample as most similar as data coming from detector.

Another function of SimApp packages code is to add background hits: rather than simulate background in the detector, it is preferred to catch a random trigger sample and mix (using correct luminosity factors) them with Monte Carlo simulated events.

3.7   Reconstruction software

We already gave prominence to packages as base element of *BABAR* software; in the following sections will be described main *packages* used for analysis done.

3.7.1   `Beta` package

`Beta` is a data analysis program developed for *BABAR*, and it is the base interface for data reconstruction. `Beta` main task is to furnish a solid and simple basement to write detailed physical analysis programs; to do that it gives needed tools to particles identification, tagging, vertexes reconstruction, etc.

All the `Beta` structure, and so the reconstruction mechanism, is based on four fundamental concepts:

- *Candidate*. A candidate is the representation that `Beta` gives to the particle that could be existed in the considered event. There are many kinds of candidates: for example a charged track, reconstructed thanks to vertex detector and DCH, can be a π candidate, while calorimeter neutral cluster can be a photon candidate. The important thing is that all candidates have same interface (they are `BtaCandidate` objects) and they can be used in a general way.

- *Operator*. An operator acts on one or more candidates, combining them in new candidates (for example defining a mother particle by two charged tracks) or extracting informations as mass, charge etc. by them.

- *Selector*. A selector is a particular structure that creates candidates with certain features starting by avalaible candidates. For example a selector for π^0 selection can seek among photons candidates pairs the ones with invariant mass close to nominal π^0 mass and combine them with a right operator in π^0 candidates. Selectors can be generic or destined to a specific physical analysis, and they can be used in different analyses (for different decay channels) without modifying anything.

- *Combiner*. It creates an agreement between two candidates. For example, reconstructed candidates can be combined to respective Monte Carlo generated candidates and so on.

For every *BABAR* event, reconstructed `BtaCandidate` objects are gathered in lists. Each list has a different identity hypothesis and different selection criteria. In table 3.2 are listed some default lists avalaible in the Micro database level.

3.7.2 `CompositionTools` package

This package [47] contains functions for the creation of `BtaCandidate` lists that describe a fixed decay reaction, for example $\pi^0 \to \gamma\gamma$, starting by `BtaCandidate` existing lists (for a little example, lists described in table 3.2). Candidates obtained are tree-like decay. For these trees we can impose kinetical and geometrical constraints. So, composite candidates are decay trees that combine tracks, neutral clusters, PID and fitting. In this way, using all the informations given by detector, `CompositionTools` is the package for reconstruction of every kind of composite particle.

In the package there are base modules for particles composition through a specific decay channel like `CompositeSelector` that offers a common interface, while for other decays and for every particles it creates a module called `CompositeSelector`, derived by the selector (cfr. 3.7.1).

- we can give at maximum six input lists (parameters are modifiable through file.tcl, but default lists are `ChargedTrack`);

- it has a `BtaCandidate` list as output;

- we can impose masses, energies, momenta, composite candidate reconstruction probability and reconstruction daughters chain cuts.

Name of the list	Description
ChargedTracks	Candidates with charge not equal to zero. Pion mass hypotesis is assigned.
CalorNeutral	Candidates are single bumps not associated to any tracks. Photon mass hypotesis is assigned.
CalorClusterNeutral	Candidates that correspond to multi-bump neutral or single bumps not associated to any cluster related to a track.
NeutralHad	Candidates that correspond neutral clusters in hadronic calorimeter not associated to any tracks.
GoodTrackLoose	ChargedTracks list candidate with: • Min momentum: 0.1 GeV • Max momentum: 10 GeV • DCH min # hit: 12 • Max DOCA in XY plane: 1.5 cm • Min Z DOCA: -10 cm • Max Z DOCA: 10 cm
GoodPhotonLoose	CalorNeutral list candidate with: • Min energy: 0.030 GeV • Min # of crystals: 0 • Max "lateral momentum": 0.8 Gev

Table 3.2: Main avalaible lists in Micro database.

- we can impose kinematical and geometrical constraints on reconstruction chains and fit and evaluate vertexes;

- the name of `CompositeSelector` we want to create is given as constructor argument.

Chapter 4

Statistical tecnique and software for physical analysis

4.1 Introduction

In this chapter it will be described the developed software to do analysis presented in this thesis work. In the first part it will be shown the analysis tecnique based on unbinned maximum likelihood fit, that *BABAR* collaboration chosen as the official one. This kind of analysis shows a better efficiency, the possibility of consider errors with a better precisions and correlations between variables. Then it will be presented the procedures that allow us to pass through reconstructed events to the ones which we fit, starting from identification of the problems and showing identified solutions; in the end, it will be described fitting software, illustrating features and functionalities. To develop analysis software has been choosen an object oriented coding technique (C++ language); we also use ROOT framework classes and a particular classes package developed by *BABAR*, called RooFit. We'll briefly present features of both.

4.2 Maximum Likelihood analysis

Analysis has been done using EML, *Extended Maximum Likelihood*, through a program that does an unbinned fit.

Now we consider a x casual variable distributed with a distribution function $f(x; \theta)$. We suppose the expression $f(x; \theta)$ well-known, but at least a parameter value θ (or parameters $\theta = (\theta_1, \ldots, \theta_n)$) should be unknown. So, $f(x; \theta)$ expression represents,

after normalizing it, hypotized probability density function (PDF) for x variable. Maximum likelihood method is a technique to estimate parameters value given a finite data sample. Furthermore, we suppose to perform an experiment where a measurement has been repeated N times, supplying $x_1, \ldots, x_N$ values, where x can represent a multidimensional casual vector, the probability of x_i included between the interval $[x_i, x_i + dx_i]$ for every i is

$$P = \prod_{i=1}^{N} f(x_i; \theta) dx_i \tag{4.1}$$

If the hypotized expression $f(x; \theta)$ for PDF and the parameters θ are correct, this probability will have an large value for measured data. While, a parameter value very different by real one gives us a small probability for realized measurements. Cause dx_i doesn't depend with parameters, same considerations can be effected for the function $\mathcal{L}$, defined as:

$$\mathcal{L}(\theta) = \prod_{i=1}^{N} f(x_i; \theta) \tag{4.2}$$

called likelihood function. It is clear that to estimate parameter value we had to maximize this function. We should underline that x_i values are well-known and so $\mathcal{L}$ only depends by parameters we want to fit.

Often it happens that number of measurements N is a random variable following a Poisson distribution with a mean value n. So, experiment result can be understand as N number and N values $x_1, \ldots, x_N$. In this case likelihood function is given by Poisson probability product to evaluate N for the function (4.2)

$$\mathcal{L}(n, \theta) = \frac{e^{-n}}{N!} \prod_{i=1}^{N} n f(x_i; \theta) \tag{4.3}$$

This function is called extended maximum likelihood. In this case to evaluate parameters values and n value it needs to determinate corresponding parameters that maximize the function.

Now we see how extended maximum likelihood technique allows us to measure the number of signal events and the number of background events in a data sample where every measurement has constituted by observable quantities.
We suppose that parameters we have to evalutate are the number of events $n_1, \ldots, n_s$, each one corresponding to a particular species of events (signal, continuum background, non-continuum background...), where s is index of such a species. To dis-

tinguish the events of each species between them, we determine the variables distributions that present an high discriminant power between those species. We fit these distributions with corresponding PDFs, indexed with $f_1^j, \ldots, f_h^j$ ($j = 1, \ldots, s$) where h is the number of PDFs for each species. When observations are independent (if no, we should consider correlation terms), extended maximum likelihood function becomes:

$$\mathcal{L} = \frac{e^{-\sum_{j=1}^{s} n_j}}{N!} \prod_{i=1}^{N} \sum_{j=1}^{s} n_j \mathcal{P}_j(x_i) \tag{4.4}$$

where

$$\mathcal{P}_j(x_i) = \prod_{l=1}^{h} f_l^j(x_i) \tag{4.5}$$

The evaluation of maximum for the extended maximum likelihood $\mathcal{L}$, or equivalently the minimum of $\chi^2 = -2\ln(\mathcal{L})$, can be done in a numeric way.

4.3   ROOT

BABAR software uses ROOT, an object oriented framework dedicated to scientific data analysis [45]. The project was born in CERN in the middle of '90s to furnish tools for data analyses that would offer a better stability with respect to FORTRAN traditional tools. At the same time, many people needs the necessity of a programming that allow them to manage quickly big projects, realized by huge and mixed groups, using advanced software programming tecniques: it has been chosen the object oriented programming, that in the 90s stood out as optimal choice to realize complex projects.

Several of the most used ROOT components are fitting and hystogramming for statistical analysis and for 2D and 3D graphics.

ROOT framework has been developed using a liberal and informal style where it is necessary an interaction between developers and users, roles very similar and often superimposed: this allows to maintain a continuous evolving project.

ROOT architecture is really portable: released version for more common commercial Unix versions (SunOS/Solaris, IBM AIX, HP-UX, SGI IRIX, Compaq/DEC OSF1), for Linux, for Windows NT and for MacOs are avalaible. Furthermore avalaibility of the source code give adaption to specific necessities of operative system possible.

The ROOT basic structure is formed by a hierarchy of over 300 classes, divided in 14 categories and organized as a tree with one common root, or a large part of classes

inherits from common class *TObject*. Among categories we find:

- *container classes* that implement a series of complex data structures as vectors, lists, sets and maps used very often in ROOT

- *histogram classes* and *minimization* procedure that offer advanced functionalities for statistical data analysis as histograms in one, two or three dimensions, profiles, fitting, minimization and evaluation of mathematical formulas

- *tree classes* and *ntuple* that estend potentialities of PAW[1] n-tuples, 2D and 3D graphical classes and classes for both graphical and textual interface for the user

- *operative system interface* that represents the only link with Operative System (OS) and favours framework portability, classes for the documentation that allows a careful and complete documentation generation during project developments.

ROOT is based on C/C++ interpreter called CINT [48]; his goal is to process programs (*script*) which not need high performance but they are important for a quick development. CINT supports about 95% of ANSI C code and about 85% of C++.

ROOT version used for the analysis described in this thesis is 3.10/02 con CINT 5.15.115.

4.4   RooFit

RooFit package is formed by a set of classes constructed on ROOT framework dedicated to unbinned maximum likelihood fit, and uses a natural and intuitive notation, that not needs a direct knowledge of ROOT programming[49, 50].

RooFit is composed by two packages: RooFitModels e RooFitCore. Former contains all the classes for the PDFs definition and complex models (as sum or product of PDFs). Latter puts at everybody disposal a set of classes to define a fitting model and fitting methods; it extends ROOT graphical functions allowing to project fitting models in function of several parameters; it allows data and both discrete and continuous variables management.

RooFit scripts are executed inside ROOT, loading external library in the initialization phase.

---

[1] Framework for statistical analysis developed in FORTRAN[**?**]

4.4.1 Main classes

Variables: *RooRealVar* and *RooCategory*

The first operation we have to do when we create a fit model is to define variables and parameters: it is not done a type distinction between them because they are all objects of *RooRealVar* class. A *RooRealVar* object is featured with a value, a minimum and maximum limit, an error, a name, an unit of measurement, a description and other attributes (for example, to establish if the object defines a constant or a variable).

The *RooRealVar* objects can be used to construct more complex structures as vectors, matrices or lists in the traditional way but RooFit already offers a container class adapted to multidimensional structures called *RooArgList* and *RooArgSet*. It allows to create a list of different variables to use them with other classes (for example as PDFs parameters).

If *RooRealVar* are used to describe continuous variables, *RooCategory* permits to manage discrete variables. Examples of discrete variables can be the B tagging, numbers of run of the events or a naive identification between different sub-channels in a combined fit. The *RooCategory* is important in the fits for the time dependent CP-violating parameters cause it allows to do simultaneous fits (in this case for B^0 and $\overline{B}^{\,0}$ and for the different tagging categories) splitting fitting data in subsets.

Data sets: *RooDataSet*

A class useful to manage a complex data structure to fit is called *RooDataSet*. It permits to organize the data as a matrix, in which single variables are represented in columns while in the other the single events. For rows the constructor allows to initializate an object in a direct way through a number of *RooRealVar* (from one to five) or with a arbitrary number of variables using a *RooArgList*. This way is more flexible but much more complicate to manage due to the presence of a middle structure.

Data are read through `read()` method. This method allows to access to both text-like files (ASCII) and binary-like ones with ROOT *tree* format.

Distributions: *RooAbsPdf*

The distributions used are the most common for the physics analyses, so we can use a gaussian (*RooGaussian*), an asymetric gaussian (*RooBifurGauss*), polinomials (*RooPolynomial*), an Argus [51] function (*RooArgusBG*), a Breit-Wigner function

(*RooBreitWigner*), an exponential (*RooExponential* and *RooLifetime*) and some others. The single classes inherits from the abstract class *RooAbsPdf* and we can define new functions in a quick and simple way.

The *RooAbsPdf* class puts at the people's disposal a series of generic methods to the events random generation based on a *try–reject* technique that can be redefined in a more efficient way for the subclasses. This class offers a fundamental method defined `fitTo(RooDataSet *data,...)` that effects a fit creating a specific object *TMinuit*; it is possible to set up some options to perform a binned fit or to minimize the likelihood function with a certain algorithm (`MIGRAD, MINOS, HESSE`). It offers some other options for plotting and drawing [52].

It's useful to note that *RooAbsPdf* distributions are automatically normalized (with unitary area).

Furthermore we can compose single PDFs through sum (*RooAddPdf*), product (*RooProdPdf*) and convolution (*RooConvPdf*). Single classes inherit from the same abstract class *RooAbsPdf*.

The *RooAddPdf* class permits to declare a model obtained with the sum of an arbitrary number of PDFs, each weighted with a parameters. This model furnishes the basis for the declaration of the extended maximum likelihood function.

4.5   Software for the cut optimization: Selector

The variables determined during the event reconstruction are saved in ROOT files (`.root`) contained in particular structures called *tree*. These files represent the output of the event reconstruction process; during this stage loose cuts are applied on several variables that caracterized our event. To discriminate signal from background. This permits to reduce files dimension because we save only the events that pass cuts (*preliminary* cuts). After the reconstruction we can optimize the values of such cuts (obviously, using tighter cuts). To do that it's necessary a program that allows us to read values of the variables held in the *tree* to establish the number of these ones passing the applied cuts. ROOT realizes that with a solid and flexible method: *selector*. This procedure is based on the realization of a user's personalized class (depending on the analyses to realize) that is derived from the *TSelector* class. These following methods are implemented in it:

- `TSelector::Begin`: This function is called every time we start to read val-

ues of the variables of the tree. It's possible to furnish a configuration parameter that permits to effect several kind of operations for a fixed selector. For example, the selector used for the analysis in this thesis work allows to prepare input to the fitting program, to perform cut and count analysis, to draw variables distributions, to select a number of events and much more. Configuration parameter is only a alfanumeric string: reading of this parameter and the identification of the operation requested is performed in this function `Begin`.

- `TSelector::Process`: This function is called for every single event. Inside, they are defined the cuts to apply on the variables values. After every cut, we have a counter that allows us to determine the number of the events that pass them. If an event is analyzed and its variables pass all the cuts, this event passes to the following procedures. In this case the event is counted in all the counters. If, viceversa, a determined cut is not respected, the event is rejected and the counting operation is interrupted in the last passed cut. All the operations requested are done with the configuration program, as saving on a file or filling a histogram.

- `TSelector::Terminate`: This function is called at the end of variables reading of all the events. It performs the conclusive operations as closing a file, drawing histograms, showing at screen the number of the events after all the cuts and so on.

Cause different analyses differ essentially for the variables and for the cut values on them, from the description given for the methods, we can guess that the method that should be much more personalized is `Process`. For all the other functions is possible to realize a model for the selector which we can refer to.

4.6 Fitting program: MIFIT

As we said in the previous sections, we use an unbinned extended maximum likelihood (ML) fit in our analysis. After the events selection, we prepare an input file (in .root format) to the ML program with the events we want to fit. This program, developed in Milan group by Alfio Lazzaro in C++, is called MIFIT. It uses the ROOT and RooFit classes, but it is a standalone executable code. Essentially, the main goal of the program is to provide a very simple interface to perform several operations used in

the different analyses. It is not requested any skills about ROOT and RooFit, but any configuration of the program is given using an intuitive configuration text files.

Bibliography

[1] T. D. Lee and C. N. Yang, *Phys. Rev.* **104** (1956) 254.

[2] C. S. Wu *et al.*, *Phys. Rev.* **105** (1957) 1413.

[3] J.H. Christensen, J.W. Cronin, V.L. Fitch, and R. Turlay, *Phys. Rev. Lett.* **13** (1964) 138.

[4] M. Kobayashi and T. Maskawa, *Prog. Th. Phys.* **49** (1973) 652.

[5] V. Fitch, in Nobel Lectures (Physics) World Scientific, Singapore (1991), lecture for 1980 prize.

[6] CLEO Collaboration, D. Bortoletto *et al.*, Phys. Rev. Lett.B **62**, 2436 (1989).

[7] M. Bauer, B.Stech and M. Wirbel, *Z. Phys. C* **34**, 103 (1987).

[8] J. Pernegr *et al.*, *Nucl. Phys.* **B134**, 436 (1978); C. Daum *et al.*, *Phys. Lett. B* **89**, 281 (1980); D. V. Amelin *et al.*, *Phys. Lett. B* **356**, 595 (1995).

[9] CLEO Collaboration, D. M. Asner *et al.*, Phys. Rev. D **61**, 012002 (2000); DELPHI Collaboration, P. Abreu *et al.*, *Phys. Lett. B* **426**, 411 (1998).

[10] R. Aleksan *et al.*, *Nucl. Phys.* **B361**, 141 (1991);

[11] M. Gronau and J. Zupan Phys. Rev. D **73**, 057502 (2006).

[12] S. Weinberg, Phys. Rev. Lett. **19**, pag. 1264 (1967).

[13] A. Salam, *Elementary Particle Physics*, ed. by N. Svartholm (Almquist and Wiksells, Stockhol 1968), p. 367

[14] S. Weinberg, Phys. Rev. Lett. **37**, pag. 657 (1976).

[15] M. Gell-Mann and A. Pais, Phys. Rev. **97** (1955) 1387.

[16] S. L. Glashow, J. Iliopoulis, and L. Maiani, *Phys. Rev. D* **2** (1970) 1285.

[17] K. Hagiwara *et al.*, Phys. Rev. **D66**, 010001-1 (2004).

[18] M. Peskin and D. Schroeder, An Introduction to Quantum Field Theory Addison-Wesley, New York (1995).

[19] P. F. Harrison, H. R. Quinn, *The* BABAR *Physics Book*, SLAC-REP-504 (2004).

[20] *BABAR* Collaboration, B. Aubert *et al.*, hep-ex/0408127, submitted to *Phys. Rev. Lett.* .

[21] F. Blanc *et al.*, *Measurements of CP-violating Asymmetries and Branching Fractions in B Meson Decays to* $\eta' K$, BABAR Note 1093 (2005).

[22] B. Aubert *et al.*, *Measurements of Branching Fractions and Time-Dependent CP-Violating Asymmetries in* $B \to \eta' K$ *Decays*, Phys. Rev. Lett. **94**, 191802 (2005).

[23] N. Cabibbo, Phys. Rev. Lett.B **10**, 531 (1963); M. Kobayashi, T. Maskawa, *Prog. Th. Phys.* **49**, 652 (1973).

[24] *BABAR* Collaboration, B. Aubert *et al.*,Phys. Rev. Lett. **94**, 161803 (2005)
Belle Collaboration, K. Abe *et al.*, Phys. Rev. D **71**, 072003 (2005)

[25] UTfit Collaboration, M. Bona *et al.*, JHEP **0507** 028 (2005)
updated results available at: http://utfit.roma1.infn.it

[26] CKMfitter Group, J. Charles *et al.*, Eur. Phys. J. C **41**, 1-131 (2005)
updated results available at: http://ckmfitter.in2p3.fr

[27] M. Gronau, arXiv:hep-ph/0510153.

[28] V. Lombardo and F. Palombo, BAD 1202 and BAD-1311, submitted to PRL.

[29] F. Palombo, R. Pellegrini and Simone Stracka, BAD-1484, v.1, april 2006

[30] M. Gronau and J. Zupan, Phys. Rev. D73, 057502 (2006)

[31] *BABAR* Collaboration, *"The BABAR Book"*, pag.404; A. Forti, F. Lanni, F. Palombo, Babar note #423; C. Dallapiccola and A. Jawahery, BaBar note #434

[32] R. Aleksan et al., BAD#350 v.11; M. Gronau and J. Zupan, hep-ph/0407002 v.3

[33] M. Gronau and J. Zupan Phys. Rev. D **70**, 074031 (2004).

[34] D. Lange et al.", BAD. 729v2

[35] www.slac.stanford.edu/BFROOT/www/Physics/Tools/Tagging/Main/Summer2006/tagging_validation

[36] J. Charles, Phys. Rev. D **59**, 054007 (1999).

[37] J. Charles *et al.*, *Eur. Phys. Jour. C* **41**, 1 (2005).

[38] A. Höcker^{a} *et al.*, BAD #628 v.5

[39] *BABAR* Collaboration, A. Aubert *et al.*, Phys. Rev. Lett.B **91**, 201802 (2003).

[40] S. Eidelman *et al. Phys. Lett. B* **592**, 1 (2004).

[41] See documentation on EvtGen package.

[42] J. Charles *et al.*, hep-ph/0406184

[43] M. Suzuki, Phys. Rev. D **47**, 1252 (1993); L. Burakovsky and T. Goldman, Phys. Rev. D **56**, 1368 (1997); H. Y. Cheng, Phys. Rev. D **67**, 094007 (2003).

[44] S. Patton, *Object Oriented Programming (For a novice, by a novice)*, CSN 95-341 C3S 95-003 (1995).

[45] Please see ROOT home page at CERN:
`http://root.cern.ch.`

[46] R. T. Hamilton *et al.*, *DataFlow Reference Manual* BABAR Note 387 (1999).

[47] F. Martinez-Vidal, R. Faccini, Composition Tools User's Guide:
`http://www.slac.stanford.edu/BFROOT/www/Physics/Tools/Vertex/CompGuide/index.html.`

[48] Please see the home page of the project:
`http://root.cern.ch/root/Cint.html.`

[49] D. Kirkby *et al.*, *A User's Guide to the RooFitTools Package for Unbinned Maximum Likelihood Fitting*, BAD 18 (2001).

[50] Si veda la home page del progetto:
http://www.slac.stanford.edu/BFROOT/www/Computing/
Offline/ROOT/RooFit.

[51] ARGUS Collaboration (H. Albrecht *et al.*) Phys. Lett. **B241**, 278 (1990); **254**, 288 (1991).

[52] F.James, MINUIT, CERN Program Library Long Writeup D506.

[53] M. Pivk *et al.*, *Background fighting in charmless two-body analysis* , BABAR Note 346 (2002).

[54] F. Blanc *et al.*, *Measurements of branching fractions and charge and time-dependent asymmetries for $B \to \eta' K$* , BABAR Note 490 (2003).

[55] F. Blanc *et al.*, *Time-Dependent CP-violating Asymmetries in B meson Decays to $etapr K$*, BABAR Note 906 (2004).

[56] G. Cerizza *et al.*, *Study of B meson Decays to $\eta' K$ in new sub-decay modes of η' and K_S^0*, BABAR Note 907 (2004).

[57] For a description of MiFit program see:

http://pcbabar4.mi.infn.it/lazzaro/MiFit

[58] Carlo Dallapiccola , "New DIRC thetaC parameterization", Charmless Hadronic B Decays AWG, Msg # 359

[59] F. Martinez-Vidal *et al.*, *The BABAR vertexing*, BABAR Note 102 (2001). (2002)

[60] A. Lazzaro and F. Palombo ,*Time-Dependent and Direct CP-Violating Asymmetries and Branching Fractions Measurements in B Meson Decays to $\eta' K$*, BABAR Note 444 (2003).

[61] A. Lazzaro and F. Palombo , *B meson decay to $\eta' K^0$ with η' to $\eta\pi\pi$ and eta to 3 π*, BABAR Note 488 (2003).

[62] http://www.slac.stanford.edu/xorg/hfag/rare/pre_winter04/charmless
OUTPUT/TABLES/charmless.pdf

[63] D. Brown *et al.*, *Local Alignment of the SVT*, BABAR Note 486 (2003).

[64] Owen Long, Max Baak, Robert N. Cahn, and David Kirkby, *Phys. Rev. D* **68**, 034010 (2003). See also new work on this subject in Ref. [**?**].

[65] *BABAR* Collaboration, B. Aubert *et al.*, *Phys. Rev. Lett.* **91**, 161801 (2003).

[66] Belle Collaboration, K. Abe *et al.*, *Phys. Rev. Lett.* **91**, 261602 (2003).

[67] N. Cabibbo, Phys. Rev. Lett. **10**, pag. 531 (1963).

[68] Fermilab E288 Collaboration, S. W. Herb *et al.*, Phys. Rev. Lett. **39**, 252 (1977); W. R. Innes *et al.*, Phys. Rev. Lett. **39**, 1240,1640(E) (1977).

[69] CDF Collaboration, F. Abe *et al.*, Phys. Rev. D **50**, 2966 (1994); **51**, 4623 (1994); **52**, 2605 (1995); Phys. Rev. Lett. **73**, 225 (1994); **74**, 2626 (1995); D0 Collaboration, S. Abachi *et al.*, Phys. Rev. Lett. **72**, 2138 (1994); **74**, 2422 (1995); **74**, 2632 (1995); Phys. Rev. D **52**, 4877 (1995).

[70] B. Aubert *et al.*, *Observation of Direct CP Violation in $B^0 \to K^+\pi^-$ Decays* , BABAR Note 1020 (2004).

[71] *BABAR* Collaboration (B. Aubert *et al.*) *Observation of CP violation in the B^0 meson system*, Phys. Rev. Lett. **87**, 091801 (2001).

[72] *BABAR* Collaboration (B. Aubert *et al.*) *Measurement of CP-violating asymmetries in B^0 decays to CP eigenstates*, Phys. Rev. Lett. **86**, 2515–2522 (2001).

[73] *BABAR* Collaboration (B. Aubert *et al.*) BABAR-CONF-02/01, SLAC-PUB-9153, hep-ex/0203007, 2002.

[74] BELLE Collaboration (K. Abe *et al.*) Phys. Rev. Lett. **87**, 091802 (2001).

[75] G. Buchala, A. J. Buras, Phys. Lett. B **333**, 221 (1994)

[76] G. Buchala, A. J. Buras, Phys. Rev. D **54**, 6782 (1996)

[77] S. Bergmann, G. Perez, JHEP **0008**, 034 (2000)